Low-Temperature Spark Plasma Sintering of Zirconium Oxide through In-situ Conversion from Zirconium Hydroxide

Nikhil Bhootpur
5095883

Low-Temperature Spark Plasma Sintering of Zirconium Oxide through In-situ Conversion from Zirconium Hydroxide

By

Nikhil Bhootpur
(5095883)

in partial fulfillment of the requirements for the degree of

Master of Science

in Aerospace Structures and Materials

at the Delft University of Technology,
to be defended publicly on Wednesday August 25, 2021 at 02:00 PM.

Thesis Supervisor:	Dr. Y. Tang	TU Delft
Thesis committee:	Prof. Dr. Sybrand van der Zwaag,	TU Delft
	Ir. J. Sinke,	TU Delft

TU Delft

Acknowledgment

The thesis was a great opportunity for my professional and personal development as an engineer. I consider myself very lucky to have worked on a novel topic in the field of ceramics. I am grateful for having met so many wonderful people at NOVAM and have them as my colleagues. Their advice and encouragement led me through the whole period of thesis.

I express my deepest thanks and gratitude to Prof. dr. Yinglu Tang, my daily supervisor for providing me with timely feedback and assistance whenever it seemed necessary. I admire her enthusiasm towards novel work and achieving good results for the betterment of science, and I'm sure to have learned from it and will adopt these values in my life as well. I choose this moment to acknowledge her contribution to the thesis greatly.

I also deeply thank Mr. Hans Brouwer from the faculty of material science engineering, TU Delft for assisting me with every step while conducting the experiments, encouraging new ideas, and providing expert advice on ceramic sintering technology. I hereby acknowledge his greatest contribution to this project

I am using this opportunity to express my deepest gratitude and special thanks to Prof. dr. ir. Sybrand van der Zwaag, chair of the thesis committee who despite being busy with his duties took out time to hear about my work and encouraged me to carry out the assignment at the faculty of aerospace engineering.

I also express my gratitude to Prof. dr. Tadhg Mahon, Durga Mainali and my colleague Siddharth Joshi for assisting me during the operation of several characterization methods. I promise to take their advice and feedback to improve my skills.

I also thank Shanta Visser for assisting me with all the practical concerns of the project, and for always clearing out my queries.

Finally, I also would like to thank all my friends who were with me during the thesis journey for morally supporting me during the tough times and for being connected throughout the lockdown period of the pandemic. I would cherish these connections for the rest of my life.

Thank you.

Sincerely,
Nikhil Bhootpur (5095883)
Student,
Aerospace Engineering: Aerospace Structures and Materials,
Delft University of Technology

List of abbreviations

- **SPS:** Spark Plasma Sintering
- **UHTC:** Ultra High Temperature Ceramic
- **TBC:** Thermal Barrier Coating
- **FAST:** Field Assisted Sintering Technology
- **DSC:** Differential Scanning Calorimetry
- **TGA:** Thermogravimetric Analysis
- **SEM:** Scanning Electron Microscopy
- **EDS:** Energy Dispersive Spectroscopy
- **XRD:** X-Ray Diffraction
- **3YSZ:** 3mol% Yttria stabilized Zirconia
- **8YSZ:** 8mol% Yttria stabilized Zirconia

Table of contents

List of figures

List of tables

1. ABSTRACT

Zirconia (ZrO_2) has emerged as a promising technical ceramic, electrolyte for solid fuel cells, and as a topcoat for thermal barrier coatings at high temperatures, *etc.* in the past decades. The traditional synthesis of ZrO_2 usually necessitates a sintering temperature as high as 1200°C. General interest in lowering the sintering temperature to reduce energy consumption and thermal stresses has led to many research works.

In this thesis, a novel route of sintering ceramics at lower sinter temperatures named 'Cold sintering' was adopted to sinter Zirconia bulks. Sintering is performed with the Spark Plasma Sintering (SPS) technique through in-situ chemical conversion of Zirconium hydroxide [$Zr(OH)_4$] precursors into Zirconium oxide. The sintering process is accelerated by the water vapor emission from the conversion reaction. For the commercial applications of Zirconia, its density, hardness, and the stabilization of favourable tetragonal phases Is necessary.

Many methods were adopted to increase the densification of the powders. The applied mechanical pressure is increased, and sintering aids are used to densify the sintered bulks. Mechanical properties like hardness and thermal conductivity values are measured. The dependence of relative densities, hardness, and thermal conductivity on the sinter conditions such as sintering dwell pressure (range: 50 MPa – 300 MPa) and sintering dwell temperature (range 400 °C – 1200 °C) is mapped out as guidance for further material property design.

In addition to the improved sintered density, the phase stabilization of tetragonal ZrO_2 phases is also enhanced at sintering dwell temperature of 900°C and dwell pressure of 50 MPa using the aliovalent phase stabilizing compounds Yttrium oxide (Y_2O_3) and Bismuth oxide (Bi_2O_3).

2. THEORETICAL STUDY

2.1 Thermal barrier coatings

Thermal barrier coatings (TBC) were used for the very first time in the 1950s [1] introduced by the NASA Lewis research center. Since then, these coatings have performed well and have replaced the gas film cooling technology in many of the aero engines. The main motive of their application was to increase the service temperature of the aero engines way higher than their melting points. They were designed to reduce the failure of the aero-engines without compensating the thrust-to-weight ratio. Thermal barrier coatings deal with increasing the service life of the aircraft engine components by insulating [2][3] them against very high temperatures, thus allowing them to work beyond their melting point and to avoid thermal failure (hot corrosion, thermal stresses). They are usually 200–500µm thick [4] and constitute a protective, non-thermally conductive ceramic topcoat, and a metallic bond coat for adhesion to the substrate.

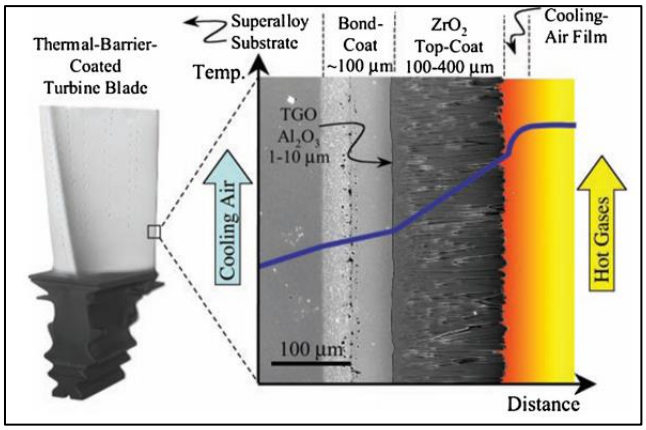

Figure 1: Thermal Barrier Coating on a turbine blade of the engine with all the three components [4]

The coating should have a coefficient of thermal expansion (CTE) such that there is no large difference with that of the substrate as it causes thermal stresses resulting in delamination of the coating. The properties and microstructures of these coatings are well dependent on the sintering/spraying technique used for deposition and on the feedstock composition.

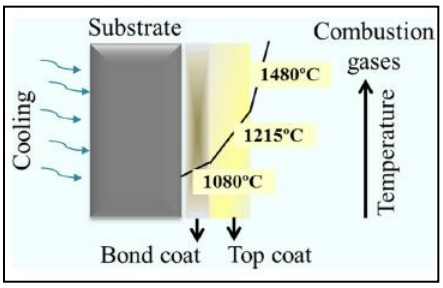

Figure 2: Variation of temperature among the different functional layers of Thermal Barrier Coating [2]

2.1.1 Topcoat

The topcoat is the topmost component of the TBC system and is usually about 100-400µm in thickness [1][2]. It provides thermal insulation [2][3] against the exterior high temperature and protects the underlying bond coat and substrate against thermal stresses. A novel set of materials called the Ultra-high temperature ceramics (UHTC) [5] have very good insulating properties and are recently being used in rocketry for space reentry vehicles. One such UHTC - Zirconia is being used as a topcoat in the TBC of aircraft engine components. These Ceramic coatings are thus used as they are resistant to higher temperatures and are porous to an extent to let the convectional cooling to proceed as it is.

The general requirements of the insulating topcoat material can be listed as having low thermal conductivity, high melting point, and good adhesive properties [1][2]. It should be thermally stable to have these properties even at very high temperatures. The coefficient of thermal expansion should be compatible with that of the substrate. Besides, it should be chemically inert towards the thermally grown oxide layer at the bond coat interface and should be resistive to corrosion from airborne fuel residues. Additionally, there should be no phase transformation between the room temperature and the operating temperature [2] to avoid residual stresses and delamination due to the transformation-induced strains.

The topcoats are usually made up of Yttrium stabilized Zirconia (YSZ) which facilitates a temperature drop of about 150°C to 300°C depending on the thickness [2][6]. It has a thermal conductivity of about 0.8-1.2 W/mK [2] and is reported to provide properties such as low density, low thermal conductivity (high concentration of point defects), the ability of stress relaxation (compatible CTE), and strain tolerance [1]. TSZ (Tetragonal stabilized Zirconia) also known as 'ceramic steel' is another pioneer material that is used as a thermal barrier coating. It exhibits the highest toughness for ceramics [7].

2.1.2 Bond coat

MCrAlY (where M = Ni/Co/both) [1][2][3][6][8] alloy is applied as the bond coat which is usually around 40-200µm[1][4]. The coefficient of thermal expansion should not have a large difference with respect to both the substrate and the ceramic coating; preferably it should be between that of the substrate and the ceramic coating [3]. The components of the alloy each have a function of their own. Aluminum oxidizes to form a passive Al_2O_3 layer which avoids further oxidation of the underlying substrate [2][6]. Indeed, it acts as a sacrificial layer which oxidizes outwards towards topcoat at the interface between the two layers and covers the substrate beneath. Chromium provides resistance against corrosion. Yttrium improves the adhesion of the TGO and also the thermal shock resistance [1].

2.1.3 Thermally grown oxide layer

Due to the presence of Al in the bond coat, a thin and dense Al_2O_3 is formed between the bond coat and the top ceramic coat during the preparation and service life due to heating. This layer is termed as "Thermally Grown Oxide" (TGO) layer. The Al_2O_3 layer acts as a protective layer in the long run and avoids further oxidation of the bond coat and the substrate below as it avoids the impregnation of contaminants into the substrate from the porous top coat.

2.2 Zirconia (ZrO_2)

Zirconium-di-oxide (Zirconia) is a functional ceramic which finds its application in various fields like aerospace, automotive, dental, medical, and other industries. Specific to the aerospace industry, it finds its application as the topcoat material for thermal barrier coatings. As required by the application as a TBC topcoat, this material qualifies for all the pre-requisite properties like high hardness, high flexural strength, compatible thermal co-efficient with the bond coat, low thermal conduction (0.8-1.2 W/mK) [2], high melting point (2700 °C)[9], etc. In most cases, the Yttrium oxide (Y_2O_3) stabilized Zirconia [YSZ] is used as the topcoat [1].

2.2.1 Allotropy

Zirconia like many ceramic counterparts exhibits allotropy. Three phases of the material exist at different ranges of temperature. Pure Zirconia exists in the monoclinic phase at lower temperatures up to 1170°C. The tetragonal phase exists between 1170°C and 2370°C. Beyond 2370°C, cubic phases are dominant [9]. The lattice structures of the phases are shown below in figure 3.

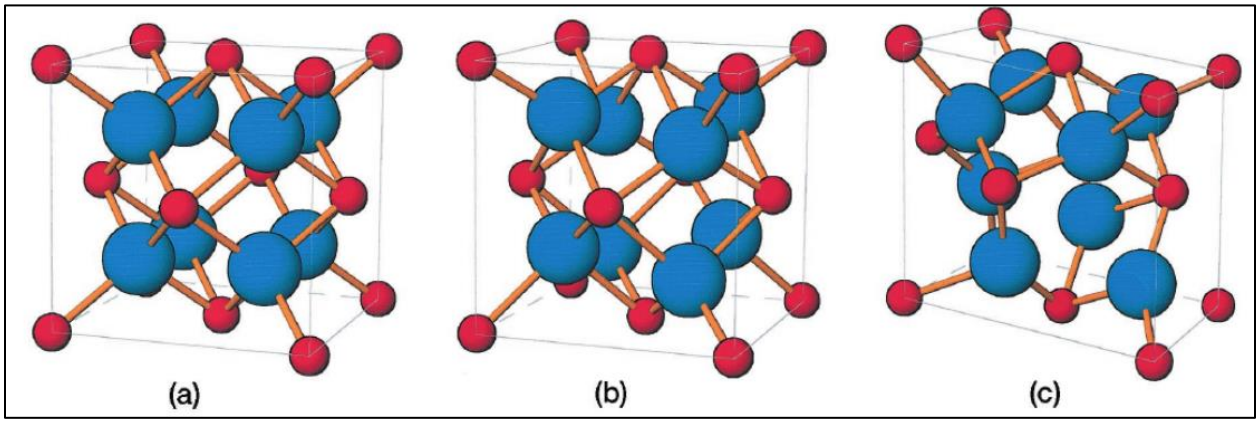

Figure 3: (a) Cubic, (b) Tetragonal, and (c) Monoclinic phases of Zirconia [10]

The densification of the tetragonal phase of Zirconia is very essential during application as the other two phases; monoclinic and cubic are not as effective to be used as a topcoat material as the tetragonal phase. The monoclinic phase at lower temperatures transforms into tetragonal or cubic phases when the high operating temperatures are reached, and stresses are induced in the system due to this transformation which results in failure of the coatings. 6-8mol% Yttria stabilized Zirconia is considered the most successful topcoat material [1] as it shows low density, low thermal conductivity with a more compatible thermal expansion coefficient with the bond coat.

Tetragonal to monoclinic phase transformation is studied as the direct consequence of the reduction of strain energy that favours Gibb's free energy of conversion to the monoclinic phase. Equation 1 shown below [9] explains these dependencies:

$$\Delta G_{t-m} = \Delta G_C + \Delta U_{SE} + \Delta U_S \ldots (1)$$

Where,

- $\Delta G_{(t-m)}$: Change of total free energy associated with tetragonal to monoclinic phase transformation.
- ΔG_c : Change in chemical free energy between Monoclinic and Tetragonal phases (< 0 below equilibrium temperature).
- ΔU_{SE} : Change in strain energy due to transformation.
- ΔU_S : Change in energy associated with the formation of new interfaces during transformation (cracks).

The phase transformation from tetragonal to monoclinic phase can be avoided when $\Delta G_{(t-m)} > 0$. This is achievable only when $|\Delta G_c| < \Delta U_{SE} + \Delta U_S$. This is possible by increasing ΔU_{SE} by doping Zr4+ ion with aliovalent cations which induces strain energy in the lattice system.

2.2.2 Phase stabilization

The phase transformation of Zirconia from monoclinic to tetragonal phases and the disadvantages associated with it can be controlled by stabilizing the tetragonal phases of Zirconia at lower temperatures.

The oxygen vacancies associated with the Zr^{4+} ions are responsible for the phase stabilization. The Zr^{4+} ions from tetragonal Zirconia phases have a 7-fold coordination with the oxygen atoms because of the presence of Oxygen vacancies. The oxygen vacancies can be created by doping Zirconia with aliovalent cations.

Doping with undersized trivalent dopants like Cr^{3+} and Fe^{3+} having lower ionic radii than that of Zr^{4+} ion create oxygen vacancies in the system. Each oxygen vacancy is associated with two dopant ions which relaxes the nearest oxygen atoms and causes two outward oxygens to move away from their position. Thus, 6-fold coordination is associated with the dopants through the M-Vo-M (M: Dopant; Vo: Oxygen vacancy) model as shown in figure 4. This associates the Zr^{4+} ions with 7-fold coordination and stabilizes the tetragonal phase as shown in figure 5.

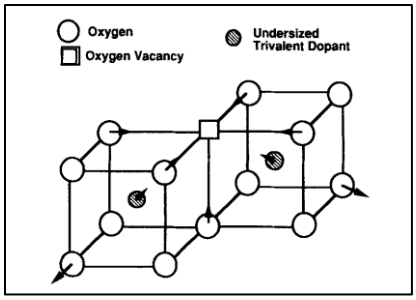

Figure 4: Oxygen relaxation by undersized trivalent dopants [11]

Doping Zirconia with oversized trivalent dopants like Y^{3+}, Sc^{3+} having higher ionic radii than that of Zr^{4+} ion replaces the Zr^{4+} ions at certain sites with the dopant ions and hence creates oxygen vacancies associated with the Zr ions through the Zr-Vo-Zr (Vo: Oxygen vacancy) model which relaxes the crystal structure thus stabilizing the tetragonal phases as shown in figure 5.

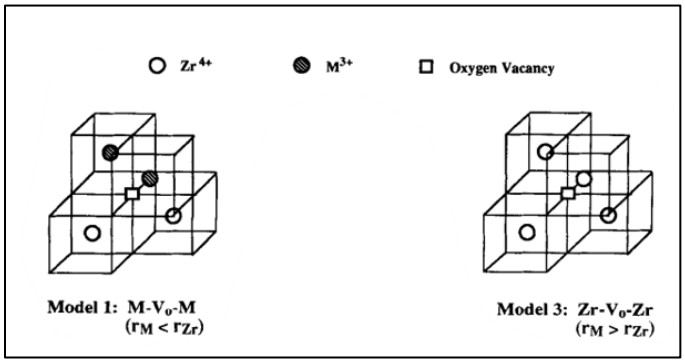

Figure 5: Doping with (left) undersized trivalent cations and (right) oversized trivalent dopants [11]

2.3 Sintering

Sintering is a process in the field of powder metallurgy and ceramics where the fusion of powder particles occurs at their points of contact at high temperatures with or without the application of external pressure and usage of sintering aids. The thermodynamically favourable state of lower surface energy and mass transport due to particle movement towards the pores are the driving forces that accelerate the sintering process. The depiction of sintering is shown in figure 6.

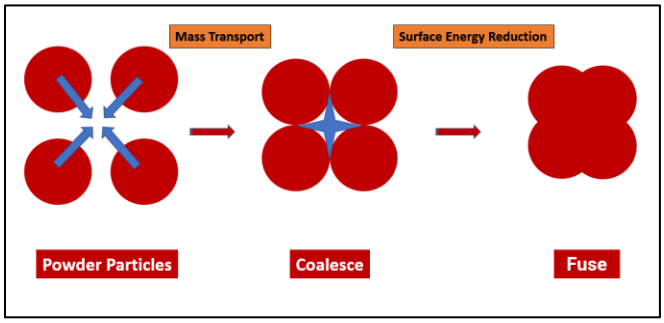

Figure 6: Graphical representation of the sintering process

2.4 Spark plasma sintering

Sinterability of ultra-high-temperature-ceramics (UHTC) is hindered by their low diffusion coefficients, and higher sizes of the available commercial powders [12]. This disadvantage can be solved by sintering the UHTCs using Spark plasma sintering (SPS) technology. SPS is a field-assisted sintering technique (FAST) that sinters by the simultaneous application of both, a pulsed electric field, and a mechanical pressurizing system.

Spark Plasma Sintering has been found advantageous compared to the other former methods of sintering. The combination of electric current, high temperatures, and pressure assist in the sintering of materials at relatively lower temperatures compared to other methods and at shorter dwell times. The densification time is generally some seconds to a few minutes [13]. The lower dwell times and lower sintering temperatures due to SPS help in controlling the microstructure of the sintered elements which possess better mechanical properties. The porosity of the spark plasma sintered samples decreases with an increase in the applied mechanical pressure. The reduction in porosity increases the hardness and strength of the sintered pellets [7]. Hence, it is necessary to have abundant mechanical pressure in the pursuit of reducing the sintering temperature. It compensates for the shortcomings of the limited thermodynamic effect in such experiments.

2.4.1 Setup

SPS consists of an electric pulse system connected to a two-electrode system which are embedded in pistons associated with a hydraulic pressurizing system. These electrode/piston systems are fixed to a detachable punch-mould system. The punch and mould materials are dependent on the maximum force that can be applied during the sintering process. They have an opening for thermocouple/pyrometer systems to measure the temperature at their interior. The powder systems to be sintered are filled in the moulds enclosed by spacers for uniform electric contact and to avoid the adhesion of powders to the interior of the mould and punches [13]. Graphite foils are used as spacers in most cases as they are electrically conductive. The powders are initially pressurized in an external pressing system before installation into the system. The typical SPS setup is shown in figure 7.

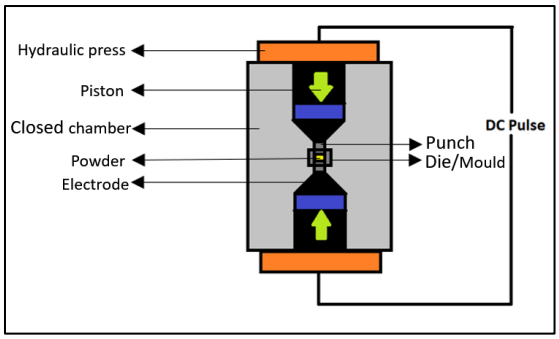

Figure 7: SPS system assembly with associated parts

Sintering is performed in a controlled environment under a vacuum or a protective gas. The system is cooled by a water/coolant chamber. The whole apparatus is under vacuum to avoid surface contamination and undesirable reactions with Nitrogen/Hydrogen/Oxygen.

2.4.2 Working

Spark plasma sintering involves the simultaneous application of electric field and mechanical pressure which provide the necessary conditions required for the sintering to occur. The thermodynamic and kinetic requirement is fulfilled by the electric field and the applied mechanical pressure.

effects of electric current:

The heat energy required for the sintering is achieved by the conversion of electric energy into heat energy in the system by resistance to the electric current flow. In SPS, the resistance of the powders (mostly ceramics) to electric current flow is generally very high, and thus when the electric contact is made via the mould-punch system, the electric current is resisted resulting in high temperatures which assist in the sintering of the materials.

The pre-sintered powder particles have a lot of defects and pores in their system. When the electric current flows through them during deformation, the local "hot spots" caused by the greater electron scattering at defects such as dislocations, voids, and grain boundaries largely enhance the lattice vibration energy in the defect vicinity. As a result, the dislocations can move more easily along the slip planes, thus enhancing the mobility of defects and in turn the mass transfer. Therefore, the stress required to move dislocations is reduced and sintering is favoured. This is termed 'Joule heating' [12][14][15].

The direct transfer of momentum from the electrons flowing through the substrate also makes the dislocations move in the lattice hence, increasing the mass transfer. This phenomenon is known as the 'Electron wind effect' [15] and is also one of the responsible factors for the highly-dense SPS products.

The ceramics which usually have brittle nature at lower temperatures have ductile properties at higher temperatures due to the flow of electric current and the associated effect of increasing the dislocation motion. This phenomenon is known as the 'Electro-Plastic effect' [15] and this induces 'Electro-plasticity' in the substrate. Hence combined, they all enhance the densification of the product under sintering.

effects of mechanical Pressure:

The mechanical loading that is applied along with the pulsating DC has two purposes [16]; breaking down of agglomerates and the re-arrangement of the grain. When the mechanical pressure in the apparatus reaches several hundred MPa, the powder agglomerates will break away and the packing of these will be increased [17] with a reduction in pore sizes. Applying quasi-static compressive pressure over the substrate in the SPS makes the pores disappear and ensure better coalescence of the grains enhancing the densification in the resulting product. The grain coalescence takes place either by the rotation or sliding of grains over one another [12].

2.5 Cold sintering process

Sintering is a process that involves high-temperature operations and subsequently requires high energy input. To reduce this, a novel sintering route named “Cold sintering” was introduced. The process is currently being applied to various ceramic systems including Zirconia systems. Consolidation of the ceramic particles via minimization of surface Gibb’s free energy is the working principle of the process [18]. The synergy between system kinetics and thermodynamics is very essential for the process to be successful.

2.5.1 Method

The method utilizes water vapour or other aqueous solution media as a sintering assist and consolidates the ceramic particles. A typical cold sintering route begins with an introduction of liquid media into the ceramic system. The liquid media dissolves the sharp edges of the ceramic powders forming a liquid phase, and renders a smooth curvature to the individual particles thus providing abundant space for particle sliding and rearrangement [18][19], lubricating the powder particles, and providing good fluidity. The next step involves pressurizing the system with an external pressure system which distributes the dissolved liquid phase all around the system into the pores and interstitials and initiates particle rearrangement. Increasing the temperature of the system concludes the process where the liquid phase evaporates leaving behind a consolidated dense ceramic system.

2.5.2 Working principle

Kinetics: Mass transport of the particles in the system is one of the two major driving forces for the consolidation of the particles in the cold sintering route. Mass transport occurs by three routes. Primarily, at the solid-solid interface, due to the applied external pressure, there is a difference in stresses between the grain particles which induces an enhanced dissolution at the particle-particle interface assisting the initial closure of pores by the dissolved particles. This is termed “liquid phase creep” [18][19]. In addition to this, there exist gradients related to concentration, surface tension, and temperature at the liquid-liquid interfaces which induce another set of mass transport via diffusion. This is termed “Marangoni flow” [19]. Finally, during the evaporation of the liquid system at higher temperatures, the concentration gradient in the liquid-solid interfaces at the evaporation sites induce mass transport. This is termed “Diffusiophoresis” [19]. All these diffusion processes reduce the surface area of the system, thus reducing Gibb’s free surface energy.

Thermodynamics: The rise of temperature above the boiling temperature of the liquid medium results in a supersaturated state of the liquid phase formed by the dissolution of ceramic particles. This supersaturated system is responsible for the sintering of the ceramic system at lower temperatures. This occurs in one of the two following ways [18][20]:

1. The particles (ionic species) in the liquid phase precipitate at the lower chemical potential sites like defects and pores reducing the surface area of the system which in turn reduces the surface Gibb’s energy at the surface which is thermodynamically favourable.
2. The liquid from the supersaturated solution evaporates leaving behind a glassy state of the remaining solution which crystallizes upon the further increase in temperature which is thermodynamically favourable.

2.6 Sintering aids

2.6.1 Ceramic systems

Sintering aids are the compounds/elements that assist the sintering of powder particles either via strengthening of bonds or crosslinking or through liquid melt fusing. One such sintering aid is Bismuth oxide (Bi_2O_3) which was claimed to have melted and dissolved in the Zirconia bulk [21] at temperatures above its melting point of 817°C. The melting of Bi_2O_3 can be utilized to fuse the powder particles to form a well-sintered bulk with less porosity and higher densification. Also, Zirconium hydride (ZrH_2) (density: 5.54g/cc) is used as one of the starting powders for the consolidation of ZrN-ZrB_2 ceramic composites [22] through reactive spark plasma sintering. The process had a 4-step sintering process with the first step attributed to the decomposition of ZrH_2. The atomic hydrogen is lost within a wide temperature range up to 1900°C with an onset at 575°C. This sintering step from this literature is adopted in the ZrH_2-$Zr(OH)_4$ system sintering in the thesis to obtain better sintering at much lower temperatures. In the case of spark plasma sintering of metal oxides like Zirconia and alumina, mainly silica (SiO_2) [23] is used as a binding agent.

2.6.2 Polymeric systems

There is an interesting set of experiments where dental ceramic brackets are made from zirconia toughened alumina through Powder injection moulding where a common set of binders are used. Here, the binder system is composed of polypropylene, linear low-density polyethylene, and paraffin wax (10:10:80 by mass). The surfactant added is stearic acid [24][25] to avoid agglomeration. The binders and powders are mixed in a wet ball machine for 24hr using water and ammonia as solvents. They are then dried in an oven and the resulting powders are sieved through a mesh. After sintering, the pores are connected making the ceramic almost monolithic after the binder is removed during heating [25]. In another set of experiments, the binder system to densify Yttria stabilized ZrO_2 is composed of water-soluble polyethylene glycol (PEG) and Polyvinyl butyral (PVB) in the weight ratio of 80:20 [26]. Organic solvents were used in another experiment where PVB was used as a binder dissolved in a mixture of ethanol and toluene to consolidate NiO-Y-ZrO2 [27].

3. EXPERIMENTS

3.1 Motive:

The results from the cold sintering experiments of various ceramics by researchers [28][18][29][30][31][20][19] paved the way to design the following experiments. The research on the cold sintering of ZrO_2 could be realized through the usage of bimodal powders or by using ZrO_2 precursors. Since the bimodal powder experiments involved the usage of nano powders which are challenging to handle without confined facilities, the other route of sintering via conversion from precursors is chosen. The hydroxides of Zirconium are chosen as the precursors that will be converted in-situ into Zirconium oxide during spark plasma sintering.

The research on such a method has already been done by Estournes *et. al.* [28] where the Zirconium hydroxides were sintered at temperatures below 400°C with the application of a mechanical pressure of 600 MPa. The phase composition data, hardness achieved were all reported. Some missing links in the research like effects of dwell temperature and dwell pressure on densification, and additional approaches in obtaining high-density sintered Zirconia along with the phase stabilization of tetragonal phases at room temperature are carried out in the present study. This is done by adopting various modifications in starting powders (agglomerate size), doping with phase-stabilizing dopants, and the addition of sintering aids as will be discussed in the following chapters. Additionally, some thermal and mechanical properties of the sintered samples *viz;* thermal conductivity and hardness will be reported and related to the sintering parameters (temperature and mechanical pressure).

3.2 Spark Plasma Sintering

The spark plasma sintering (SPS) is performed using the FCT Systeme Gmbh SPS machine at the Materials science department of the 3ME faculty, TU Delft. The sintering assembly consists of two tapered adapters for the uniform application of load on the punches which are in turn surrounded by the die that controls the diameter. Temperature, current, and pressure sensors assist in measuring the required values and control the system to perform sintering according to process parameters which can be programmed through an in-built system connected to a computer. The dies and punches have circular holes for pyrometer viewing and the insertion of thermocouple wire.

Figure 8: Spark Plasma Sintering machine

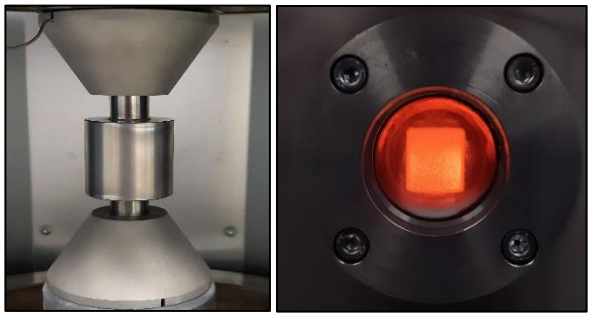

Figure 9: SPS sintering assembly

3.2.1 Sample preparation

All the sintering experiments are performed following the same protocol as follows. First, the inner surface of the hollow cylindrical die is covered with thin Graphite foils to ensure uniform conduction of the electric current throughout the die. The $Zr(OH)_4$ powders (from Sigma Aldrich) are then weighed and filled in the dies enclosed by thin Graphite discs at both the end surfaces of the powder filling (inner end surface of the dies) for uniform electrical conduction. The powder filling process is entirely done in a glove box with limited oxygen and water content to avoid contamination of the powders. The die assembly is then pressed under a hydraulic press up to 1ton force (10kN) to prepare the cylindrical green body. The die is placed in the SPS machine and is locked in between the top and the bottom adapters which are in turn fixed to the plunger and the base respectively. The thermocouples are attached to the die/punch surfaces and the pyrometer is set up. The vessel enclosing the die is closed to create a sintering atmosphere, either vacuum or a noble gas. The heating and pressure ramps are then loaded into the SPS machine, and the process is started.

3.2.2 SPS cycles

An SPS cycle with a uniform heating rate (50°C/min) and the free cooling stage is applied to all the samples. The system is flushed and pressurized several times before heating/load application to ensure that the sintering atmosphere is not contaminated. The varied parameters are the mechanical pressure at dwell stage, temperature during the dwelling stage, and the dwell time. All the different dies used for the sintering have a diameter of 20mm are made of either Graphite/Stainless steel/Tungsten Carbide–Cobalt. The thermocouples were calibrated for each die before the first use.

3.3 Density measurements

The pellets prepared by the SPS have high porosity. Hence, the geometrical densities are considered for the calculation of their relative densities. The as-prepared samples were measured for their 2 dimensions; diameter and thickness to calculate their volume. The mass of the pellets was measured in air. The density was calculated by dividing the obtained mass by their geometric volume. The relative density was calculated by dividing the obtained density with that of the tetragonal Zirconia from literature *i.e.*, 6.10g/cc [32] [33].

3.4 Hardness testing

Hardness is a mechanical property of a material that denotes how much a material resists the indentation loads without plastically deforming. It is a very important property for a coating as the coatings are prone to small impact loads and abrasion.

Sample preparation:

The surface of the pellets is polished with meshed grinding papers of various grit sizes to prepare a smooth and flat surface for the hardness test. This is necessary for the indentation to be visible while measuring its dimensions.

Testing:

Leitz Durimet micro Vickers hardness testing machine was used to measure the hardness of the samples. A counterweight of 500P (0.5Kg=4.905N) was applied over the indenter and this load was applied for around 15 seconds on the sample surface. The magnified image of the indentation is available for viewing through a microscope attached to the intender which aids the measurement of the diagonals of the intender. The Vickers hardness number is calculated using the formula:

$$HV = \frac{0.1891 * F}{d^2}$$

Where;

HV – Vickers hardness (N/mm^2)

F – Applied force (N) = 4.905N

d – Avg. length of the diagonals (mm)

Figure 10: Vickers hardness tester

3.5 Ball milling

The doped powders and the powders mixed with sintering aids are mixed in the required ratio in a planetary ball mill with 2-propanol as a disperser. The 'ball mass: powder mass' ratio is always taken to be 4:1. They are mixed for 3 hours at 300rpm rotation speed. The slurry is dried overnight in the fume hood. The powders are then ground using mortar and pestle before sintering.

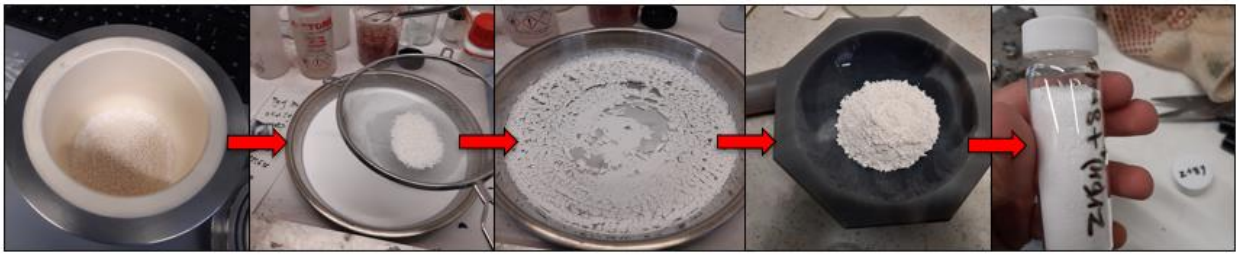

Figure 11: Ball milling procedure

3.5 Characterization

3.5.1 Scanning electron microscopy

The extent of sintering in the sample can be examined by observing the microstructure. The conjoining of the grains at the edges signifies a well sintered sample.

The microstructure of the sintered samples is examined qualitatively using the JEOL JSM7000F scanning electron microscope (SEM). The samples were prepared by slicing them with a diamond edge cutter to expose their cross-section. These are embedded in the Methyl methacrylate resin with the cross-section exposed for observation. The samples are then polished with grinding papers of different grit sizes to ensure flatness before observing them under the SEM. The embedded and polished samples are then sputtered with a 15nm Gold coating.

The sputtered samples are clamped to the sample holder and are transported inside the vacuum chamber. Since the samples are ceramics, accelerating voltage as high as 15kV with an emission current of 10µA along with a probe current up to 12µA can be applied to obtain high magnification and high-resolution images.

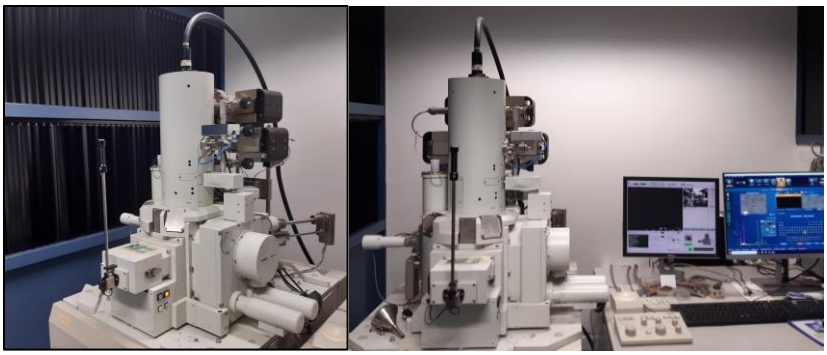

Figure 12: JEOL JSM-7000F Scanning electron microscope with Oxford instruments EDS system

3.5.2 Energy dispersive spectroscopy

The chemical composition of the sintered samples is investigated by the Oxford instruments energy dispersive spectroscopy system integrated with the SEM system.

Several sites were randomly chosen among the sample/powder surface for the investigation of the composition. The elemental ratio of Zr:O was used as the quantitative data to determine the conversion of hydroxides to oxides. The chemical composition at several randomly distributed sites is mapped onto an enlarged SEM image of the same site to observe the uniform mixture in doped powders, additive-rich powders, and mainly the conversion of hydroxides into oxides of Zirconium.

3.5.3 XRD

X-ray diffraction spectroscopy was used to identify the different phases present in the powders. Rigaku MiniFlex 600 XRD machine shown in figure 13 was used to measure the XRD peak data from the powder compositions.

The sintered bodies are analyzed with XRD spectroscopy to identify the ZrO_2 phases present in them. The as-formed pellets are ground using a mortar and pestle to break them into aggregates and then the aggregates are ground into fine powders. These free powders are filled in the sample holder and the powder surface is flattened before installation into the XRD system for the clear characterization of lattice structures. Cu-alpha X-rays are emitted and scanned after reflection from the surface with diffraction angle range 2Θ = 10°-80°. From the literature, it is found that the tetragonal reflections are observed around 30.19°, and the monoclinic reflections are observed around 28.20° and 31.47° [34].

Figure 13:Rigaku MiniFlex600 X-ray diffraction machine

3.5.4 Thermogravimetric Analysis (TGA)

The thermogravimetric analysis is performed on the pure Zr(OH)4 powders using the TGA machine at the faculty of aerospace engineering, TU Delft to check the mass loss associated with them at different temperatures. The powders were heated from ambient temperature up to 900°C with a heating rate of 50°C/min to mimic the sintering cycle that will be used in the experiments.

3.5.5 Differential Scanning Calorimetry (DSC)

The Differential scanning calorimeter from the Material science department, TU Delft is used to measure the thermal behaviour of the pure $Zr(OH)_4$ powders. The powders are heated from ambient temperature up to 600°C and back to ambient temperature with a heating and cooling rate of 5°C/min to closely measure their behaviour at each temperature step. A TGA machine associated with this DSC machine also measured the associated mass loss at each small temperature step (5°C/min).

Figure 14: Differential scanning calorimeter/Thermogravimetric analyzer

3.6 Thermal conduction testing

The thermal conductivity measurements are performed using the Hot Disk TPS 2200 machine at the faculty of civil engineering and geosciences, TU Delft. Two sintered pellets are placed, one on each side of the measuring disc which is enclosed in a closed chamber. The disc is heated slowly and the temperature change at each end of the two samples is measured with the increase in time and thus the thermal conduction is calculated.

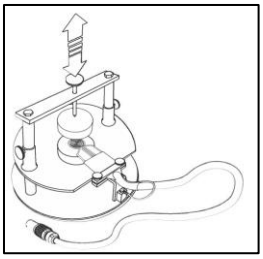

Figure 15: HotDisk TPS 2200 thermal conduction measurement machine

4. PRELIMINARY RESEARCH

To initialize the study, the $Zr(OH)_4$ powders are sintered under SPS at different dwell temperatures from 200°C up to 1200°C. These experiments are designed to study the influence of the temperature on mass loss, chemical conversion to ZrO_2, sintering, and densification.

4.1 Pre-sintering analysis:

4.1.1 Mass loss calculation:

The decomposition of $Zr(OH)_4$ to ZrO_2 is accompanied by dehydration from the system as shown in equation 2 below.

$$Zr(OH)_4 \rightarrow ZrO_2 + 2H_2O \ldots(2)$$

Since water is the byproduct that will be eliminated during the reaction, the ideal mass loss on the complete conversion of $Zr(OH)_4$ to ZrO_2 is calculated as follows.

- The molecular mass of Zr(OH)4 = 159.22g/mol
- The molecular mass of ZrO2 = 123.22g/mol
- The molecular mass of H2O = 18g/mol

$$Zr(OH)4 \rightarrow ZrO2 + 2H2O$$
$$(1mol) \rightarrow (1mol):(2mol)$$
$$(159.22g) \rightarrow (123.22g):(36g)$$

∴ The ideal mass loss % for the complete reaction: $\frac{36.00}{159.22} * 100 = 22.61\%$

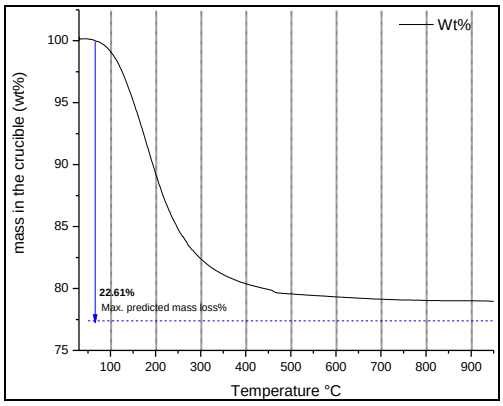

Figure 16: Thermogravimetric analysis of the pure $Zr(OH)_4$ powders

The TGA analysis with 50°C/min heating ramp up to 950°C shown in figure 16 conformed with this result as the maximum mass loss was well below the predicted value signifying that the conversion to oxides is indeed by the dehydration of the precursor hydroxide powders.

4.1.2 Thermo-Gravimetric Analysis and Differential Scanning Calorimetry analysis:

The DSC curve from figure 17 shows an endothermic peak at 176°C preceded and followed by a trough in the range 100°C-200°C. This can be attributed to the initial dehydration of the hydroxide powders after the boiling point of water is reached. The curve undergoes a major shift at 403°C where it reaches an exothermic peak corresponding to the crystallization of amorphous Zirconium hydroxide into crystalline zirconium oxide which is in line with the information from the literature [34]. Also, the slow heating rate rendered a new set of interesting data points from the TGA curve from figure 17 which depicts a large mass loss between 100°C and 200°C and a substantial mass loss between 200°C and 400°C after which it remains constant confirming the dehydration to be complete at around 400°C.

The mass spectrometry embedded with the DSC/TGA machine measured the composition of the outlet gas from the system. The plot from figure 18 shows water liberation from the system being detected beginning from around 100°C which reached 2 peaks at 185.40°C and 405°C after which it decreased to remain almost constant. This signifies that the dehydration of the precursor powders is evident and the conversion into oxides is occurring up to around 400°C.

These results suggest that further sintering experiments are to be conducted starting from 400°C onwards to ensure that the obtained sintered product is Zirconia and not Zirconium hydroxide.

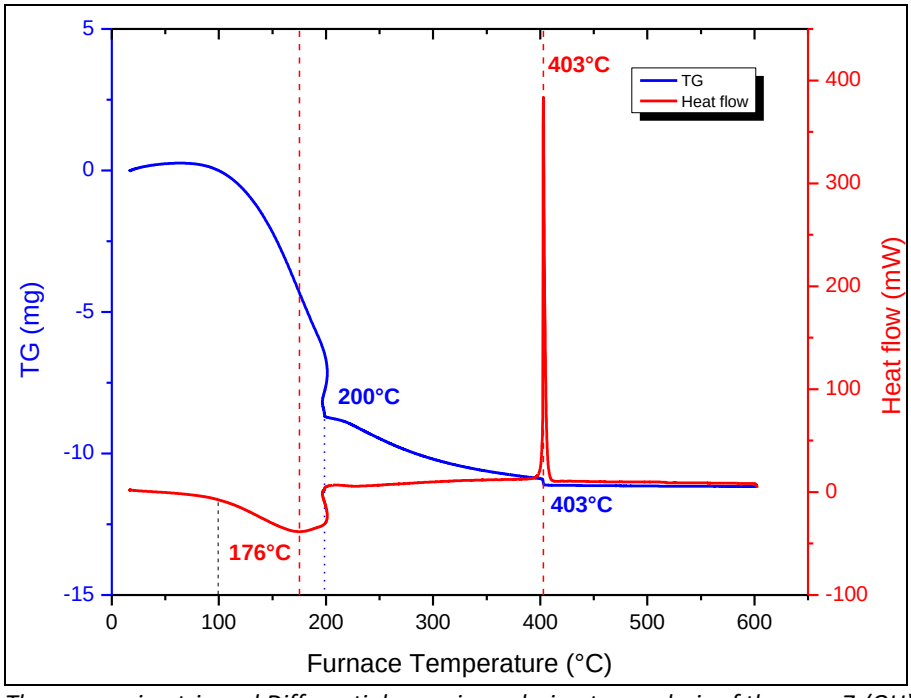

Figure 17: Thermogravimetric and Differential scanning calorimetry analysis of the pure $Zr(OH)_4$ powders

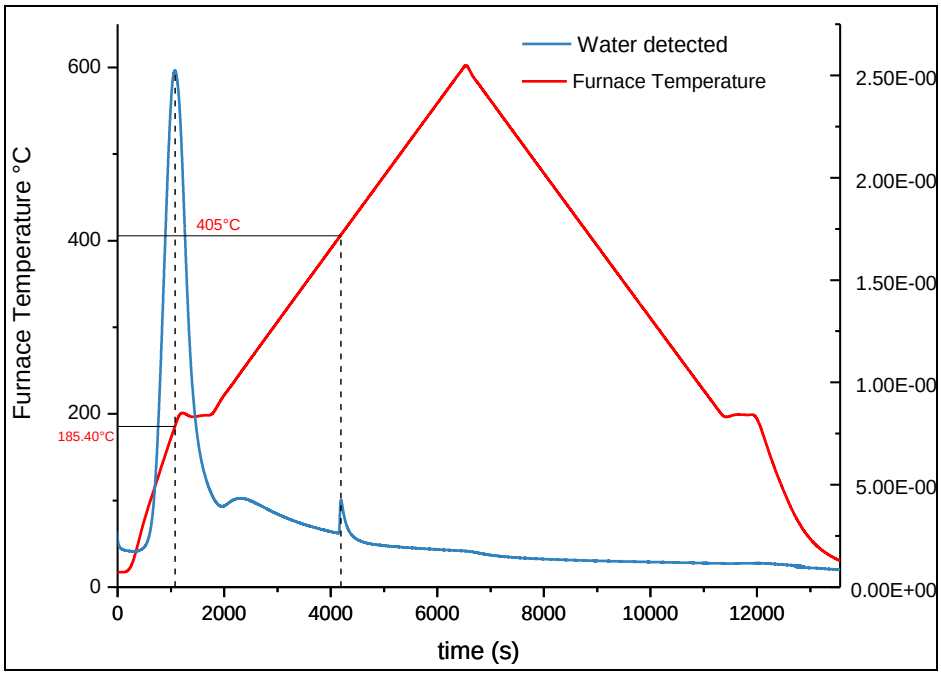

Figure 18: Mass spectrometry analysis of the pure $Zr(OH)_4$ powders

4.1.3 Cold Pressing

All the samples, irrespective of their sinter parameters are pressed into a cylinder before loading into SPS through cold pressing. They are pressed while filled in the dies used for SPS under 1 ton-force (10kN) using a hydraulic press. These cylindrical green bodies have a density of 1.73g/cc which corresponds to a relative density of 28.39%.

Table 1: Green density measurement results

Mass (g)	Diameter (mm)	Thickness (mm)	Volume (cc)	Density (g/cc)	ZrO_2 density (g/cc)	Relative density (%)
5.0	20	12	3.77	1.73	6.10	28.39

Figure 19: $Zr(OH)_4$ green body

4.2 Experimental setup

The powders are loaded onto the SPS machine and heated to their dwell temperatures with a temperature ramp of 50°C/min. Simultaneously, the maximum mechanical loading of 50 MPa (16kN) is also reached through a simultaneous pressure ramp alongside the temperature ramp as shown in figure 20. The samples are dwelled for 10 minutes at the set dwell pressure and dwell temperature and are freely cooled after this step. To compare the results to a standard set, a paradigm sample with 3mol% Yttria stabilized ZrO_2 (3YSZ) starting powders is sintered at 1200°C dwell temperature with the same parameters. The experimental parameters are listed in table 2 and depicted graphically in figure 21.

Table 2: Sintering parameters for the preliminary sintering experiments

Sinter atmosphere	Vacuum
Mechanical Pressure at dwell stage	50 MPa (16kN)
Heating rate	50°C/min
Cooling rate	Free Cooling
Dwell time	10 minutes

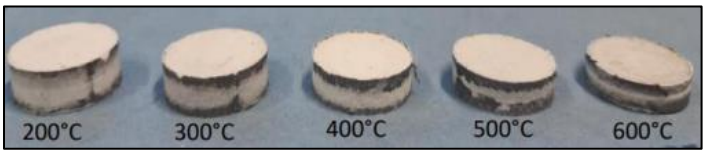

Figure 20: Pellets formed after SPS OF $Zr(OH)_4$ powders

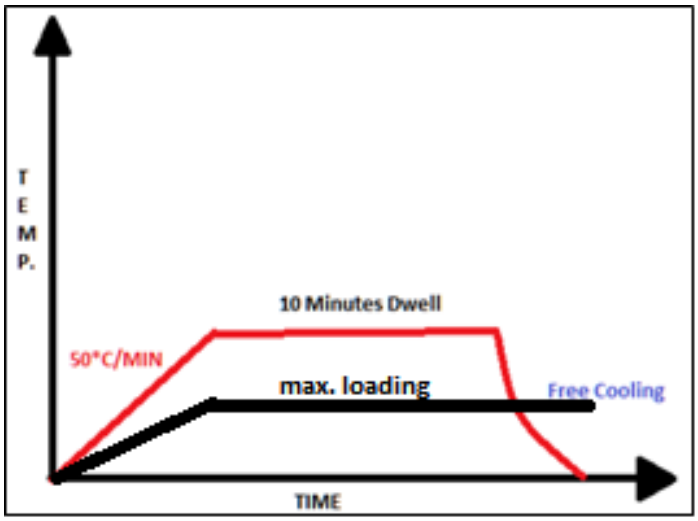

Figure 21: SPS Pressure-Temperature profile for the initial experiments

4.3 Sintering

After the sintering was performed by the SPS technique, the data regarding the piston travel and its speed corresponding to the temperatures and forces at every point is retrieved from the system and are plotted. The piston travel data provides an insight into the sintering profile of the hydroxide powders. The plots for the 1200°C dwell temperature, 50 MPa dwell pressure conditions for $Zr(OH)_4$ and 3mol% Yttria stabilized ZrO_2 samples are shown in figure 22 for comparison of piston displacement curves. It is seen clearly that the ZrO_2 sinters with a typical S-shaped sinter curve whereas the $Zr(OH)_4$ sample sinters steeply first and then with a different slope.

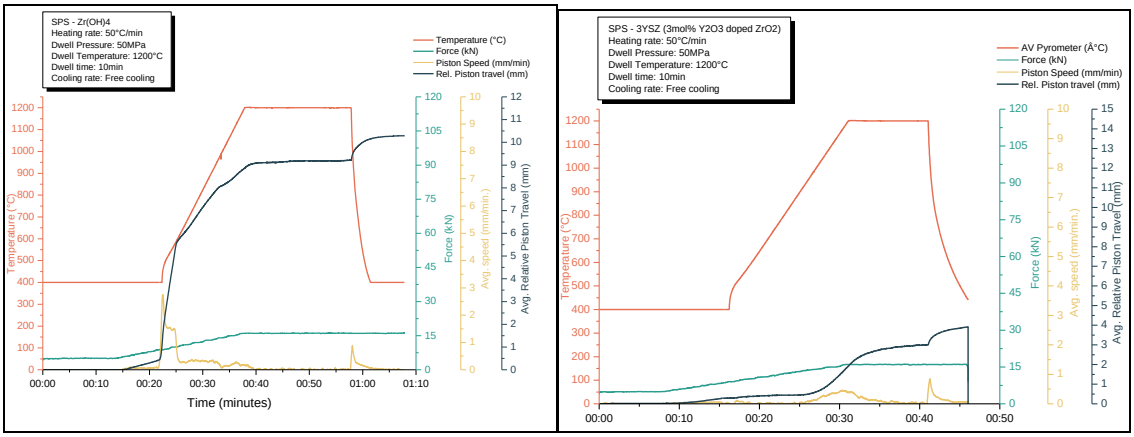

Figure 22: SPS piston-displacement curve with the corresponding temperature and pressure changes for pure $Zr(OH)_4$ [left] and 3mol% Yttria stabilized Zirconia (3YSZ) [right]

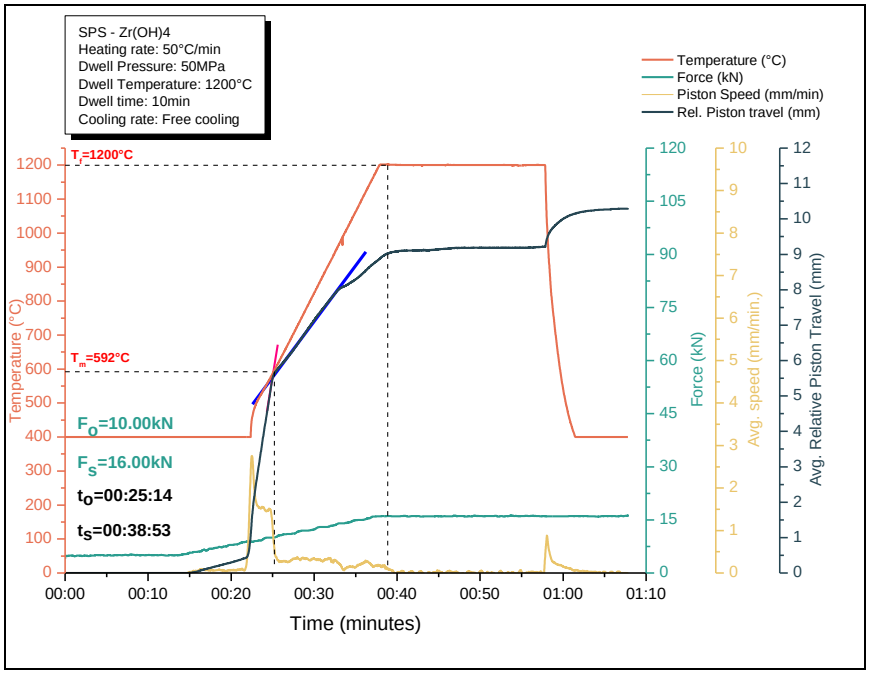

Figure 23: SPS piston displacement curve with projected sintering times, forces, and temperatures for 50 MPa dwell pressure sample of pure $Zr(OH)_4$ sintered at 1200°C

From the $Zr(OH)_4$ plot from figure 22, it is deduced that the piston movement occurs at two different rates: the first one from the initiation up to around 400°C-600°C (corresponding to complete mass loss and the advent of crystallization) followed by a less steep rate up to the dwell temperature. The slopes from both these curves are plotted and their conjoining point is regarded as the onset of the sintering process. The curve goes on to be a horizontal line after reaching the dwell conditions and the beginning of such a trend is regarded as the end of the sintering. This is shown graphically in figure 23. Similar plots for the rest of the sintering experiments can be found in Appendix A. The time, force, and temperature difference between these two points are calculated and tabulated in table 3.

Table 3: Total sintering time, temperature, and force for the 50 MPa dwell conditions

Dwell temperature	Sintering onset temperature	Sintering saturation temperature	Sintering time (mm:ss)	in s	Onset Force	Sintering saturation force	Sintering Force
400°C	393.00	400.00	02:33	153.00	15.75	16.00	0.25
500°C	385.00	500.00	04:16	256.00	13.00	16.00	3.00
600°C	394.00	600.00	05:45	345.00	12.20	16.00	3.80
800°C	573.00	800.00	10:20	620.00	12.50	16.00	3.50
900°C	447.00	900.00	08:20	500.00	11.20	16.00	4.80
1200°C	592.00	1200.00	13:39	799.00	10.00	16.00	6.00

4.4 Densification and conversion

The results of the preliminary experimental set are shown in table 4. The release of water as a byproduct during the conversion reaction influences the sintering of the powder grains. As depicted by the TGA curve earlier, it is seen that the water loss is complete and almost constant from 400°C onwards. The mass loss is shown in figure 24 also confirms this. In theory, the OH^- ions from the $Zr(OH)_4$ powders assist the mass transport by carrying the Zr^{4+} ions towards the vacancies hence accelerating the sintering process. The OH^- ions are then combined and liberated as H_2O. The liberated water can be considered as a default binder system that coagulates the powder grains together while it is evaporated from the system. This is evident from the microstructures of the sintered pellets. It can be observed visually from figure 26 that the sintering is evident once the dwell temperature is higher than 400°C and improves above this temperature. Thus, high densification of bulks via mass transport by water which is abundantly present in the system at and after 400°C is evident.

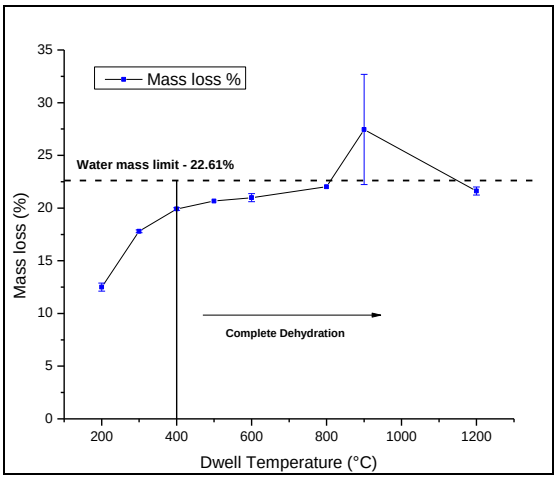

Figure 24: Mass loss of $Zr(OH)_4$ during sintering at different dwell temperatures

The density of a bulk signifies how good the packing of the constituents is done. In this case, the higher the density of the sintered bodies, the better is the sintering as the powder grains are being fused for better compaction in densely sintered bulks. Figure 25 shows the variation of relative density of the sintered pellets with their dwell temperatures. It is evident that the temperature indeed improves sintering as the densification increases with the increase in dwell temperature. Also, from table 3 it can be deduced that more sintering time available for higher dwell temperature samples is also responsible for higher densities.

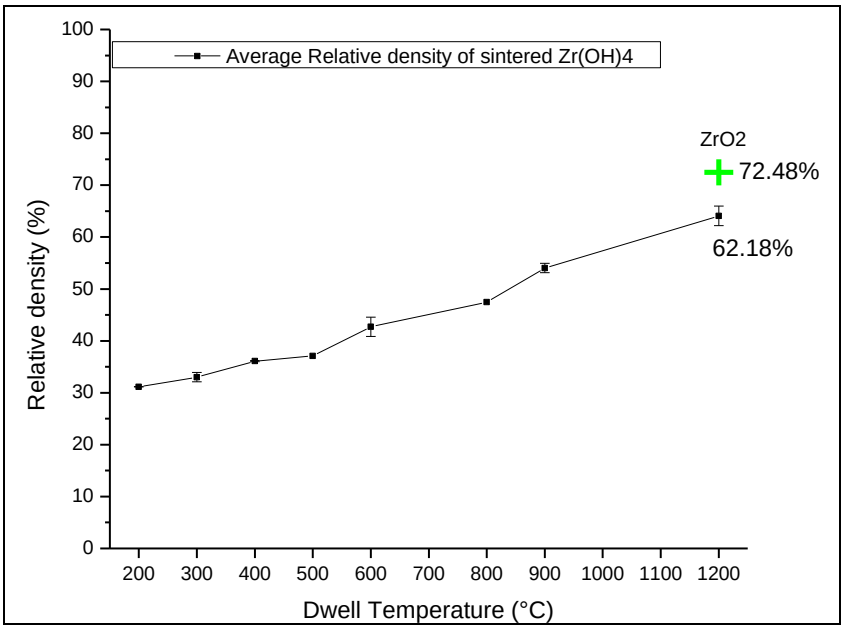

Figure 25: Relative densification of sintered $Zr(OH)_4$ at different dwell temperatures

Table 4: Mass loss and relative density of $Zr(OH)_4$ at different dwell temperatures sintered with a dwell pressure of 50 MPa and with 10 minutes dwell time.

Dwell Temperature (°C)	Initial mass (g)	Final mass (g)	Mass loss (%)	Diameter (mm)	Thickness (mm)	Volume (cc)	Density (g/cc)	Relative density (%)
200.00	5.10	4.48	12.12	20.30	7.30	2.36	1.90	31.11
200.00	5.10	4.44	12.88	20.38	7.16	2.33	1.90	31.20
300.00	5.10	4.19	17.92	20.27	6.63	2.14	1.96	32.09
300.00	5.10	4.20	17.67	20.33	6.26	2.03	2.07	33.89
400.00	5.10	4.08	20.04	20.39	5.69	1.86	2.20	36.00
400.00	5.10	4.09	19.78	20.29	5.73	1.85	2.21	36.22
500.00	5.10	4.05	20.67	20.23	5.57	1.79	2.26	37.07
600.00	6.53	5.14	21.36	20.22	6.42	2.06	2.49	40.85
600.00	6.53	5.18	20.61	20.46	5.80	1.91	2.72	44.59
800.00	5.10	3.98	22.02	20.32	4.24	1.37	2.89	47.44
900.00	6.53	4.40	32.68	20.26	4.21	1.36	3.24	53.12
900.00	6.53	5.08	22.24	20.35	4.66	1.51	3.35	54.95
1200.00	6.53	5.14	21.24	20.38	3.92	1.28	4.02	65.97
1200.00	6.53	5.09	22.01	20.50	4.07	1.34	3.79	62.18
1200 ZrO2	5.00	4.93	1.40	20.32	3.44	1.12	4.42	72.48

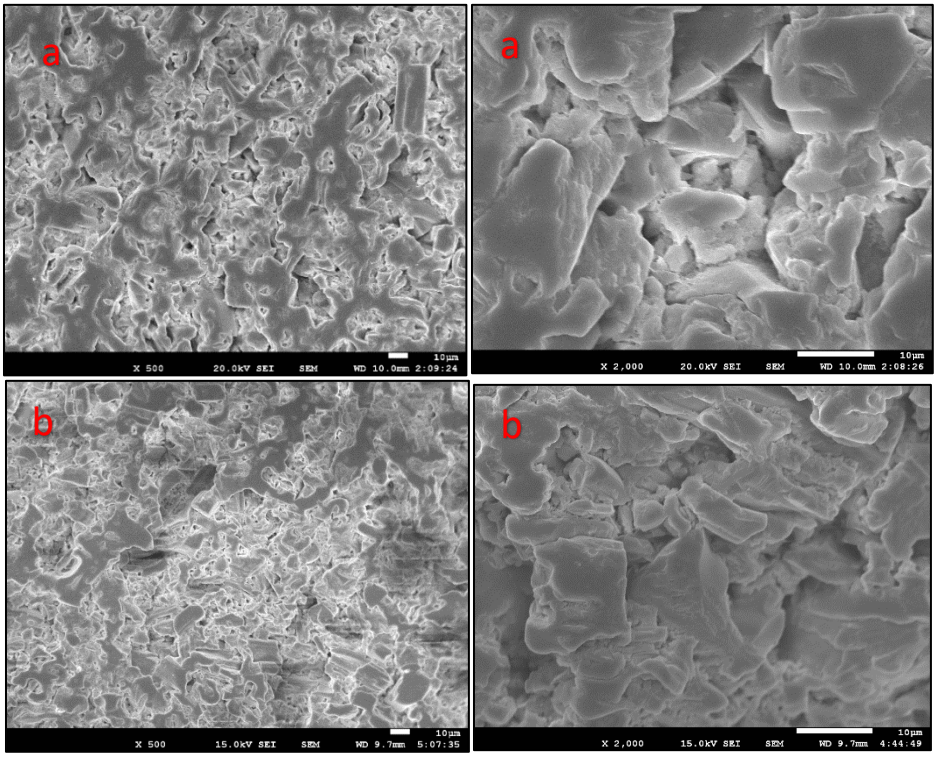

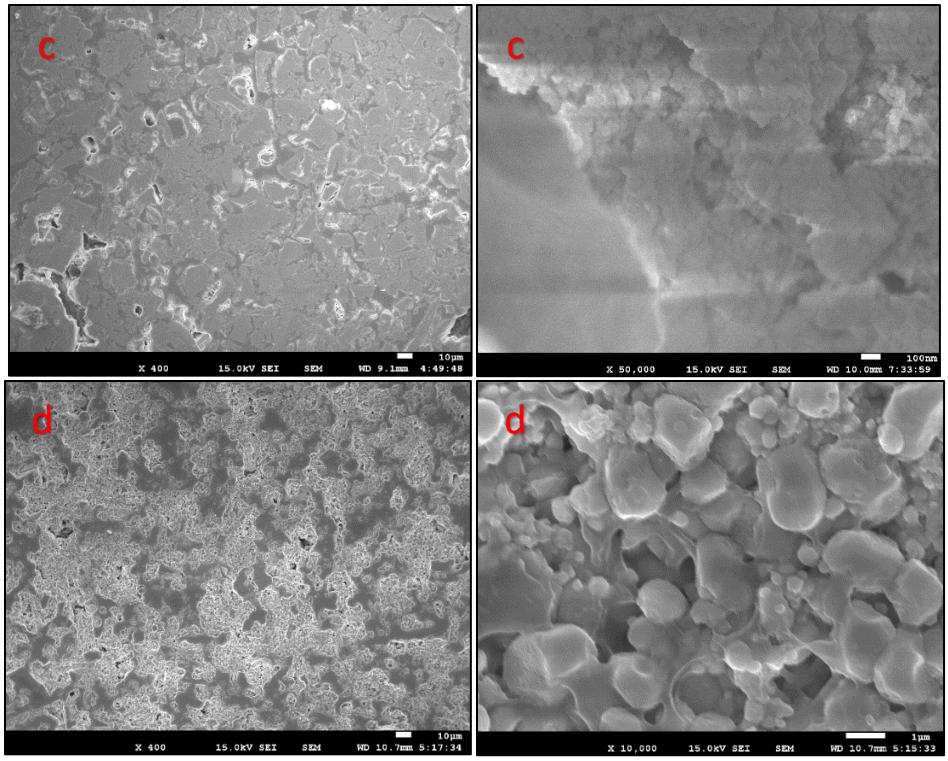

Figure 26: SEM micrographs of cross-sections of the sintered samples at different dwell temperatures (a) 200°C, (b) 600°C, (c) 900°C, (d) 1200°C [top to bottom respectively]

To confirm the uniform conversion of Zirconium hydroxide powders into Zirconia in the sintered body, Energy Dispersive Spectroscopy (EDS) is performed at random sites on the surface of the sample. To account for uniform accumulation of data across the surface, the cross-section was divided into 4 quadrants as shown in figure 26 and one site from each quadrant was selected for the analysis.

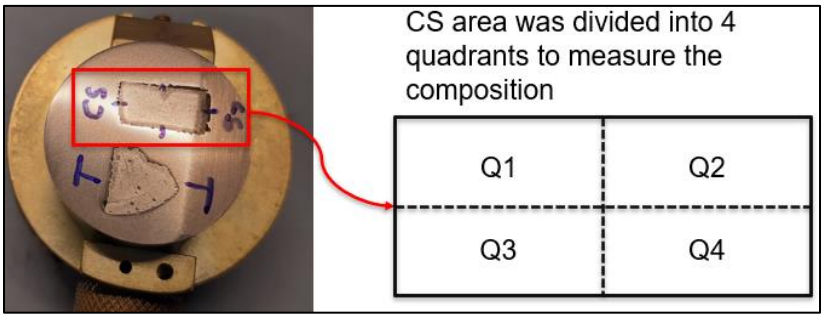

Figure 27: Division of the cross-section of samples for EDS analysis

The atomic percentage of Zirconium and Oxygen elements are quantified and the atomic % ratio of Zr:O atoms are used as comparison parameters. The ideal value of atomic % of Zr:O should be 1:2 or 0.5 if the expected product is ZrO_2. The obtained results are listed in table 2 below.

Table 5: Atomic percentage ratios of Zr:O at quadrants of samples sintered at different dwell temperatures.

Temperature °C	Quarter	Zr: O	Avg. Zr: O
200°C	1	0.36	0.37
	2	0.36	
	3	0.38	
	4	0.37	
600°C	1	0.6	0.56
	2	0.5	
	3	0.53	
	4	0.59	
900°C	1	0.58	0.53
	2	0.56	
	3	0.46	
	4	0.59	

The atomic ratios of Zr:O suggest that the conversion is not yet complete at 200°C but has been completed at around 600°C. The atomic ratios confirm the conversion of Zirconium hydroxide into Zirconia after 400°C dwell.

4.5 Phase Transformation: Influence of temperature on the Zirconia phases formed

The results from the analysis are plotted in figure 28. At 200°C, the powders are still amorphous implying the conversion to ZrO_2 to be incomplete. At 400°C both the monoclinic and the tetragonal phases co-exist with the advent of crystallinity. Onwards, up to 1200°C, the monoclinic phases are more reflected, and the tetragonal phases start to diminish indicating that the monoclinic phases are more stable at room temperature for the samples sintered at temperatures above 400°C. The peak shifts in the graph denote the changes in the lattice dimensions occurring due to stress induced by the phase change from tetragonal to monoclinic phases after 400°C.

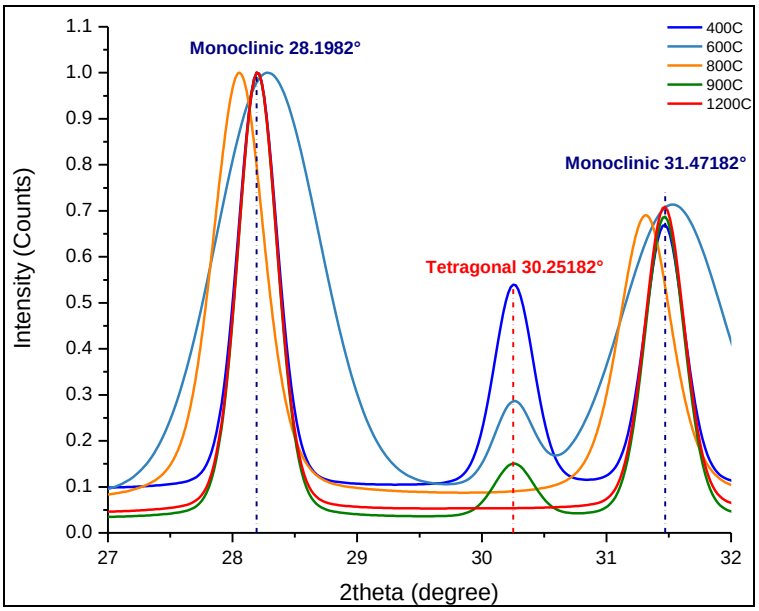

Figure 28: Phases of ZrO2 in samples cooled from different sintering temperatures

From the plots, it can be determined that there are shifts in the lattice parameters when the dwell temperature increases from 600°C to 1200°C. These shifts in lattice parameters are identified after performing full pattern matching using the 'Fullprof suite' software. The results are tabulated in table 6 with lattice shifts depicted in red text. The refinements can be found in Appendix B.

The lattice parameters remain the same for all the temperature dwell points except for 600°C and 800°C, where a shift in the XRD peaks is observed denoting changes in the lattice parameters. The XRD peak for the monoclinic phase shifts towards the left for the 600°C sample signifying a constraint in the crystal system, whereas the peak shifts towards the right for the 800°C sample signifying the relaxation in the crystal system. The changes in these values from table 6 show a decrease in lattice parameters for 600°C samples confirming the constraint in the crystal system and an increase in lattice parameters for 800°C samples confirming the relaxation in the crystal system.

Table 6: Lattice parameters of Zirconia phases for different dwell temperature samples sintered at 50 MPa

Sample	Monoclinic						Tetragonal					
	a	b	c	α	β	γ	a	b	c	α	β	γ
400°C	5.15101	5.20706	5.32099	90.00000	99.16990	90.00000	3.59480	3.59480	5.18240	90.00000	90.00000	90.00000
600°C	5.14085	5.19209	5.30692	90.00000	99.10742	90.00000	3.59480	3.59480	5.18240	90.00000	90.00000	90.00000
800°C	5.16623	5.21731	5.34224	90.00000	99.18029	90.00000	3.59672	3.59672	5.22128	90.00000	90.00000	90.00000
900°C	5.15101	5.20706	5.32099	90.00000	99.16990	90.00000	3.59480	3.59480	5.18240	90.00000	90.00000	90.00000
1200°C	5.15101	5.20706	5.32099	90.00000	99.16990	90.00000	3.59480	3.59480	5.18240	90.00000	90.00000	90.00000

The main findings of the preliminary research can be enlisted as follows:

- Sintering temperature should at least be 400°C since the conversion to oxide form is evident after this temperature.
- Water is indeed being liberated during the sintering which can be utilized as a sintering aid to achieve better results.
- The density of the samples should be increased to obtain sintered pellets with better mechanical properties.
- Monoclinic phases are largely present in the system and hence the required tetragonal phases need to be stabilized.

This initial study directs the further study towards achieving two major aspects: better densification and stabilization of tetragonal phases at room temperature.

5. IMPROVED DENSIFICATION

Densification is a measure of packing and fusing of the sintered powder particles. It is quantified by the density of the bulk. Here, the geometrical densities of the sintered bodies are measured and compared with the ideal density value of ZrO_2 corresponding to that of the tetragonal ZrO_2 from the literature [32]. Achieving better densification of the sintered pellets is one of the main concerns as the close packing and percolation of powders will improve many bulk properties. To achieve this, three parameters are modified: dwell time, powder size, and dwell pressure. Increased dwell time in an isothermal temperature condition is expected to enhance the sintering of powders as more time will be available for mass transport which will indeed assist the powders to fuse. Low grain size powders have high surface area and thus, high surface energy. As minimization of the surface energy is the main driving factor for sintering, the reduction in powder grain size is expected to trigger more powder contacts and thus shall improve sintering. Increasing the dwell pressure is expected to provide significant improvements in the densities of the samples as packing of powders and crushing of agglomerates will be possible.

5.1 Dwell time dependency

Sintering is performed with a dwell time of 10 minutes, 20 minutes, and 40 minutes at 1200°C dwell temperature. The sintering cycles were kept the same as the preliminary experiments with a 50°C/minute heating rate, simultaneous pressure ramp-up to 50M Pa, and free cooling.

Table 7: Sintering parameters for the dwell-time experiments

Sinter atmosphere	Vacuum
Mechanical Pressure at dwell stage	50 MPa (16kN)
Heating rate	50°C/min
Cooling rate	Free Cooling
Dwell time	10, 20, 40 minutes

The densification data obtained are shown in table 8. It is observed that the density is not affected by the dwell time. Also, it can be inferred from the microstructure comparisons from figures 29-31 that the sintering of powders is not affected by the increase in dwell time.

Table 8: Relative densities of the sintered samples at different dwell times of 1200°C dwell sintering

Dwell temperature (°C)	Dwell time (min.)	Relative density (%)
1200°C	10	68.80
	20	64.88
	40	61.02

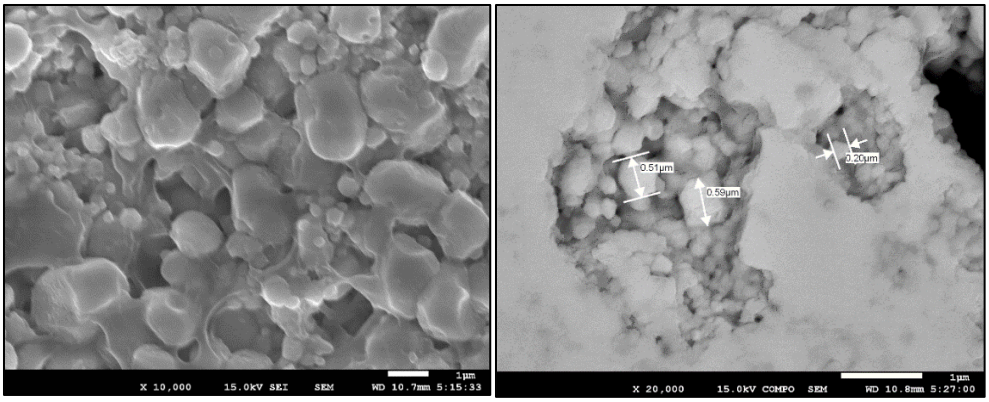

Figure 29: Microstructure of 1200°C 10-minute dwell samples

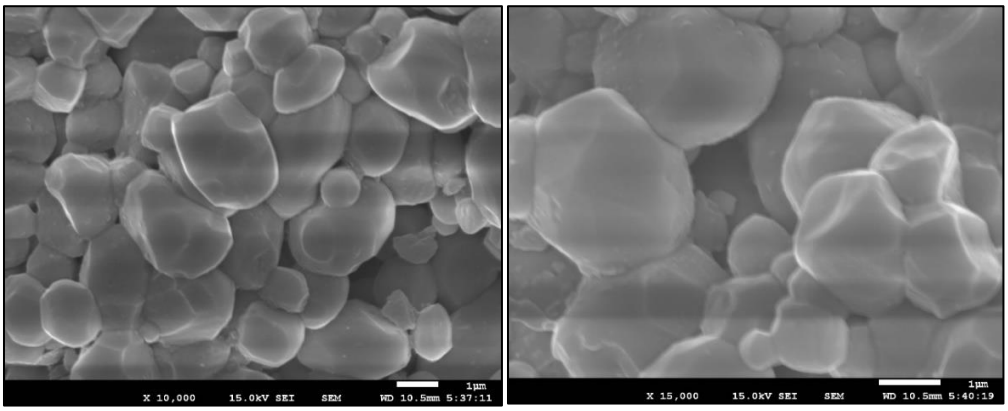

Figure 30: Microstructure of 1200°C 20-minute dwell samples

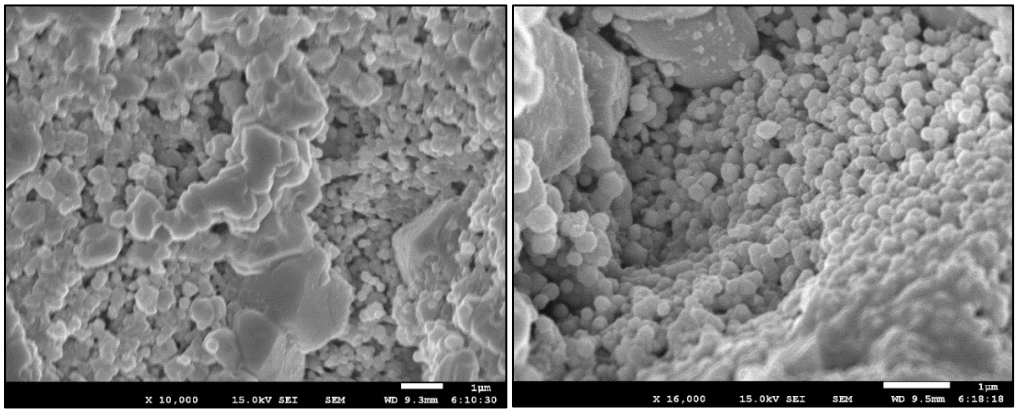

Figure 31: Microstructure of 1200°C 40-minute dwell samples

5.2 Powder size dependency

Reducing the powder sizes is expected to change the packing efficiency of sintered bodies and improve sintering. Also, minimization of the large surface energy of smaller grain size powders is expected to drive the sintering process. To investigate this, the powder grain size was reduced using sieves of different mesh sizes. The sieves with mesh sizes of 90µm, 50µm, and 25µm are used. The sintering cycles are kept the same with 50°C/minute heating rate, and free-cooling with a 40-minute dwelling at 900°C.

Table 9: Sintering parameters for the powder size experiments

Sinter atmosphere	Vacuum
Mechanical Pressure at dwell stage	50 MPa (16kN)
Heating rate	50°C/min
Cooling rate	Free Cooling
Dwell time	40 minutes

Table 10: Relative density measurements for the varied grain size samples

Sieve mesh size	Diameter (mm)	Thickness (mm)	Volume (cc)	Density (g/cc)	ZrO2 density (g/cc)	Relative density (%)
90µm	20.42	3.5	1.15	3.31	6.1	54.28
50µm	20.68	4.16	1.4	3.39	6.1	55.6
25µm	20.46	2.16	0.71	3.22	6.1	52.73
Unsieved	20.35	3.64	1.18	3.24	6.1	53.06

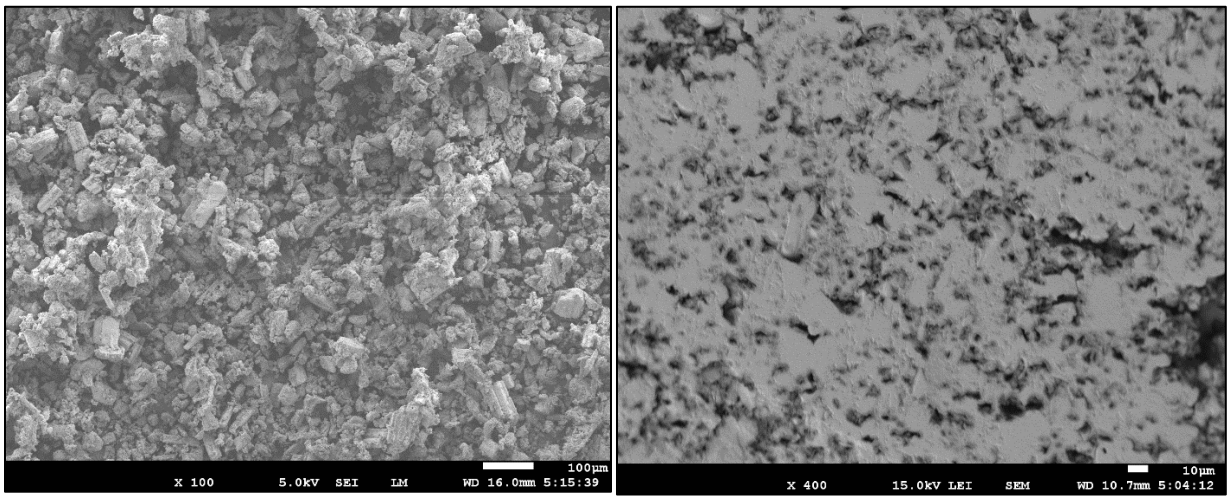

Figure 32: Free powders and sintered surface - 90µm sieved $Zr(OH)_4$ powders

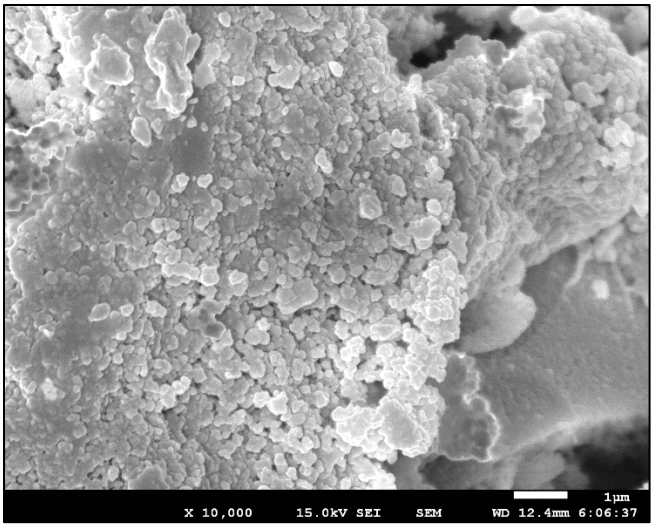

Figure 33: Sintered surface - 50µm sieved $Zr(OH)_4$ powders

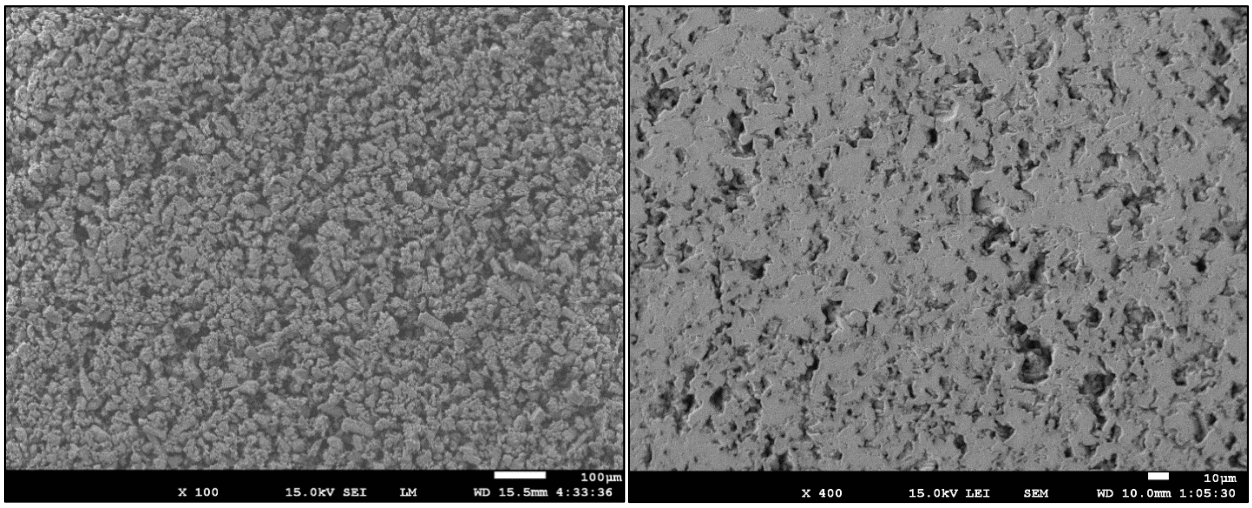

Figure 34: Free powders and the sintered surface - 25µm sieved $Zr(OH)_4$ powders

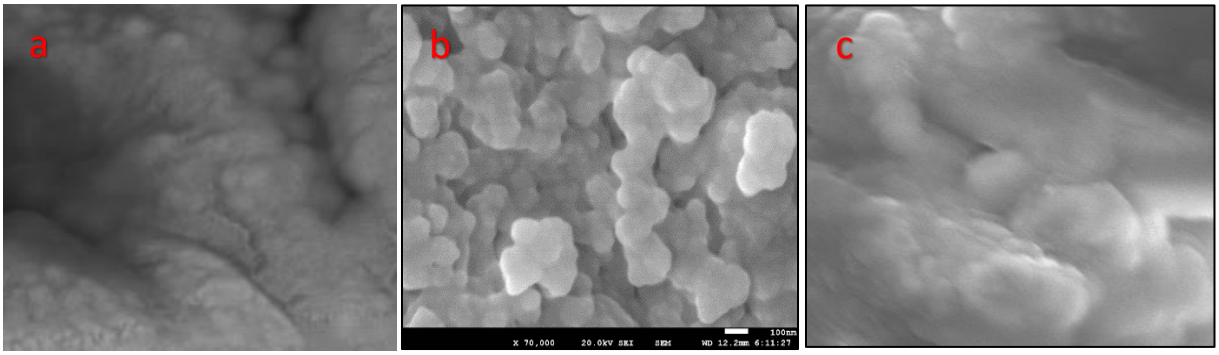

Figure 35: Magnified images showing the sintering of powder particles sieved using (a) 90µm, (b) 50µm, (c) and 25µm sieves before SPS

The relative density results are tabulated in table 10. Even though the results depict similar densities, the samples show improvements in the sintering can be seen in the microstructure images of their cross-sections from figures 32 to 35.

The Vickers hardness for the samples is measured and the values are tabulated in table 11 and the indentations are shown in figure 36. The calculations of hardness for all the samples can be found in Appendix C. The hardness values do not show any dependency to the sieve used to reduce the powder sizes and vary within the range of 0.6-0.9GPa. This may be due to the large agglomeration of powders during the pressing which negates the effect of powder sizes on sintering.

Table 11: Vickers hardness values for the samples from sieved pure $Zr(OH)_4$ systems

Sample	Average Hardness	Hardness (GPa)	Porosity (%)
25 micrometer mesh sieved	65.35	0.64	47.27
50 micrometer mesh sieved	53.91	0.53	44.40
90 micrometer mesh sieved	88.59	0.87	45.72

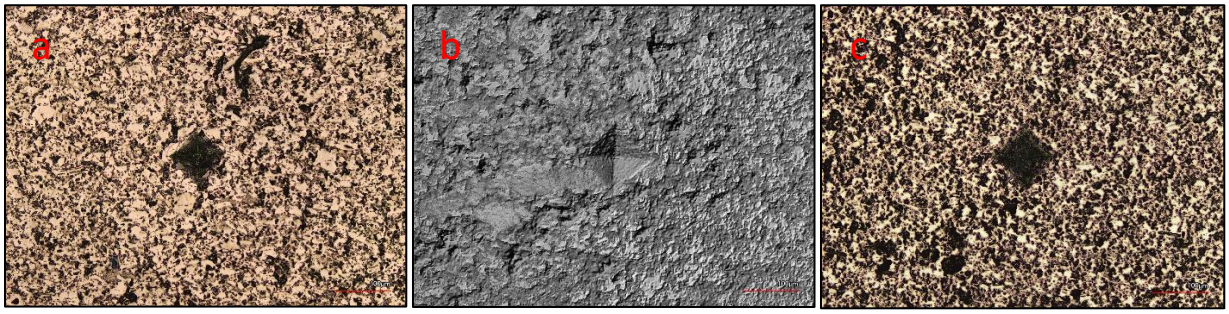

Figure 36: Vickers indentation images for (a) 90µm, (b) 50 µm, and (c) 25 µm mesh sieved (left to right samples)

5.3 Influence of Mechanical pressure on densification

The $Zr(OH)_4$ powders are sintered with the application of different mechanical loadings to study their effect on the relative density of the products. The sintering cycles are kept the same as the preliminary experiments *i.e.*, 50°C/minute heating rate, simultaneous loading ramp, 10-minute dwell time, and free-cooling. The samples are sintered at dwell temperatures 400°C, 600°C, and 900°C at two different mechanical loadings; 150 MPa and 300 MPa with dies made up of Stainless steel (20mm SS die, FCT Systeme Gmbh.) and Tungsten carbide – Cobalt (20mm WC-Co die, FCT Systeme Gmbh.), respectively. The results were compared to the preliminary experiment results with 50 MPa dwell pressure using the Graphite dies.

Table 12: Sintering parameters for the varied mechanical pressure experiments

Sinter atmosphere	Vacuum
Mechanical Pressure at dwell stage	50MPa (16kN)/150MPa(47kN)/300MPa (94kN)
Heating rate	50°C/min
Cooling rate	Free Cooling
Dwell time	10 minutes

Table 13: Relative density measurements of $Zr(OH)_4$ at different dwell temperatures sintered at different mechanical pressures under SPS

Dwell Temperature (°C)	Dwell time (minutes)	Dwell Pressure (MPa)	Diameter (mm)	Thickness (mm)	Volume (cc)	Density (g/cc)	Relative density (%)
400	10	50	20.29	5.73	1.85	2.21	36.22
	10	50	20.25	7.09	2.28	2.27	37.16
	10	50	20.45	7.04	2.31	2.27	37.21
600	10	50	20.16	5.10	1.63	2.47	40.46
	10	50	20.22	6.42	2.06	2.49	40.85
	10	50	20.46	5.80	1.91	2.72	44.59
900	10	50	20.26	4.21	1.36	3.24	53.12
	10	50	20.35	4.66	1.51	3.35	54.95
1200	10	50	20.50	2.90	0.96	4.20	68.80
	10	50	20.38	3.92	1.28	4.02	65.97
	10	50	20.50	4.07	1.34	3.79	62.18
400	10	150	20.51	5.79	1.91	2.69	44.08
	10	150	20.72	5.76	1.94	2.70	44.33
	10	150	20.57	5.62	1.87	2.72	44.59
600	10	150	20.52	5.02	1.66	3.11	50.95
	10	150	20.80	5.05	1.72	3.01	49.40
	10	150	20.78	4.80	1.63	3.18	52.15

900	10	150	20.92	3.56	1.22	4.19	68.73
	10	150	20.77	3.53	1.20	4.27	70.05
	10	150	20.91	3.53	1.21	4.21	69.09
400	10	300	20.61	5.01	1.67	3.10	50.89
	10	300	20.06	4.11	1.30	3.77	61.85
600	10	300	20.66	3.19	1.07	4.54	74.36
	10	300	21.06	3.41	1.19	3.99	65.43
900	10	300	20.00	3.00	0.94	5.31	86.97

The results are tabulated in table 13 and the relative densities are plotted against temperature in figure 37. The increase in densities can be attributed to the mechanical pressure changing the morphology of the powders and their contacts by breaking down the powder aggregates into individual grains. The microstructures of the cross-sections of the samples sintered at 150 MPa and 300 MPa dwell pressures shown in figures 39 and 40 show better sintered microstructures than the samples sintered at 50 MPa samples.

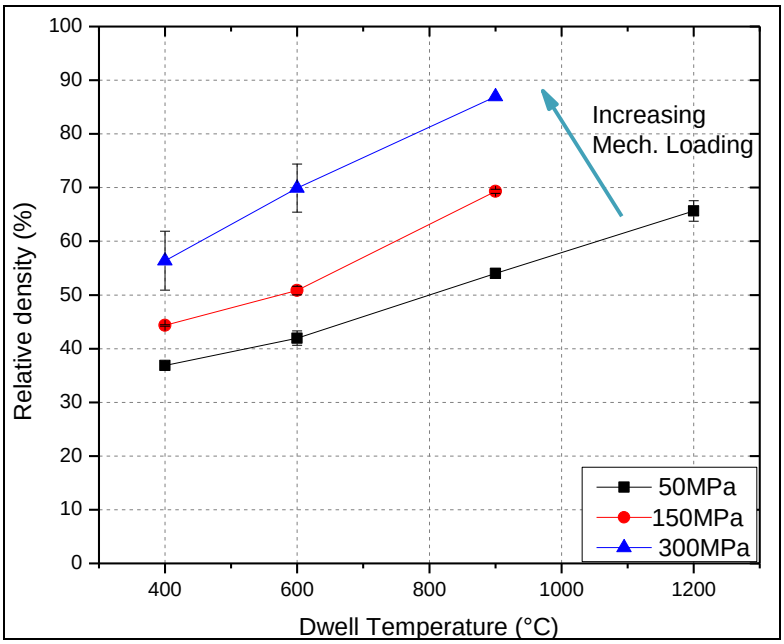

Figure 37: Relative density dependency upon mechanical pressure applied

An ideal graph of relative density is plotted against the dwell temperatures sintered at different dwell pressures considering the maximum densifications achieved with traditional SPS from literature. The plot is shown in figure 38.

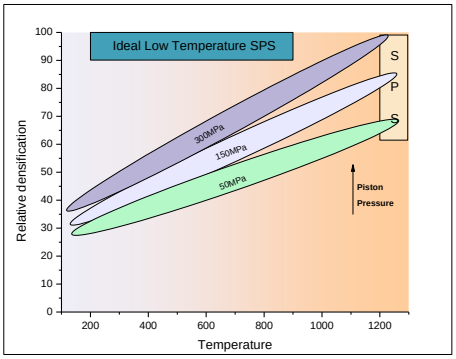

Figure 38: A depiction of the relative density trend for the low-temperature SPS at different mechanical loadings during the dwell

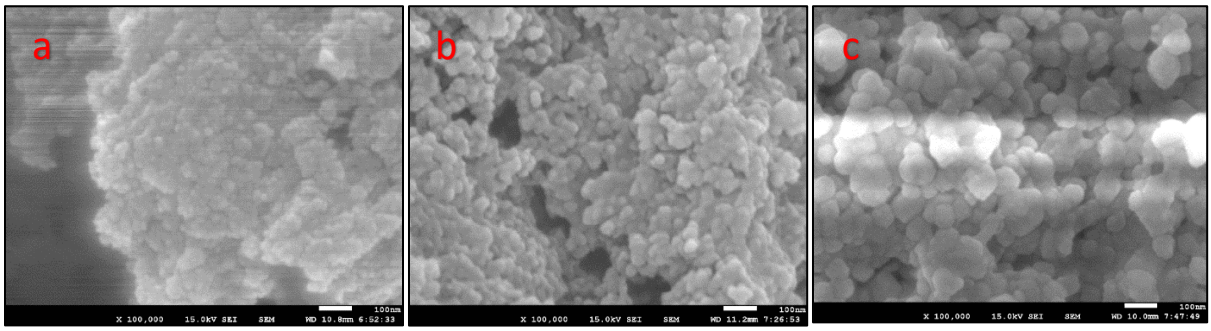

Figure 39: Microstructures of $Zr(OH)_4$ sintered at (a) 400°C, (b) 600°C, and (c) 900°C at 150 MPa dwell pressure

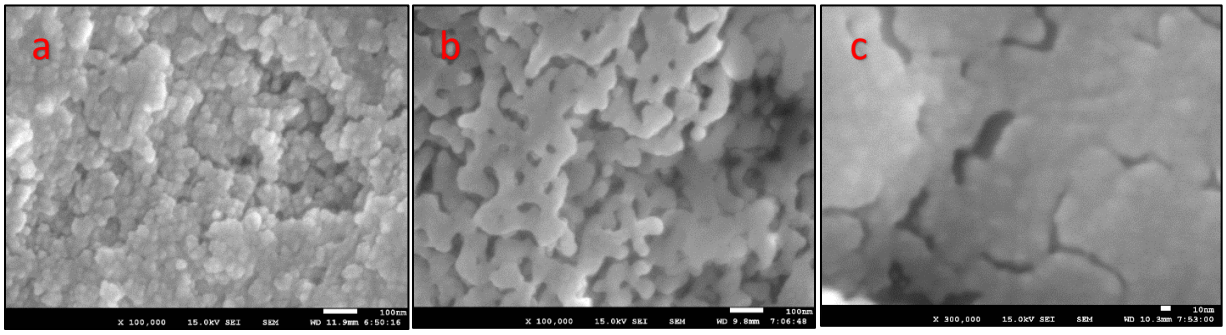

Figure 40:Microstructures of $Zr(OH)_4$ samples sintered at (a) 400°C, (b) 600°C, and (c) 900°C at 300 MPa dwell pressure

Table 14 depicts the hardness measured from samples sintered at different dwell pressures. Figures 41-43 depict the Vickers hardness indentations on the samples sintered at 50 MPa, 150 MPa, and 300 MPa. The calculations for the hardness are shown in Appendix C. The hardness of the samples increases with the increase in the applied mechanical pressure at the same dwell temperature condition. The trend varies for the sample sintered at 900°C dwell temperature and 300 MPa dwell pressure and this can be attributed to the large cracks formed in the sintered plane as can be observed from figure 40. The hardness values are also compared to the 3YSZ sample's hardness in figure 44.

Table 14: Vickers hardness values of samples sintered at various dwell temperatures and mechanical pressures

Sample	Avg. Vickers Hardness (HV)	Hardness (GPa)	Rel. density (%)	Porosity (%)
900°C-50 MPa	29.04	0.28	53.74	46.26
400°C-150 MPa	26.85	0.26	44.33	55.67
600°C-150 MPa	98.29	0.96	50.83	49.17
900°C-150 MPa	321.37	3.15	69.3	30.7
400°C-300 MPa	229.32	2.25	56.37	43.63
600°C-300 MPa	348.22	3.42	69.9	30.1
900°C-300 MPa	301.88	2.96	86.97	13.03
3mol% Yttria stabilized ZrO2 1200°C-50 MPa	961.98	9.43	72.48	27.52

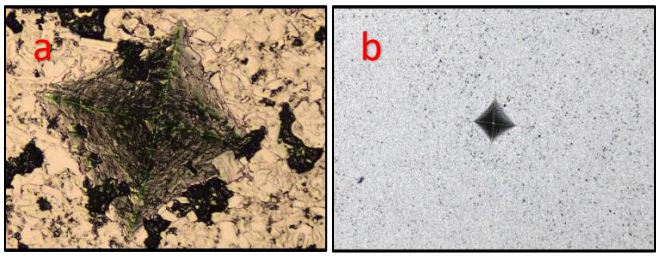

Figure 41: Vickers indentation images for (a) $Zr(OH)_4$ 900°C and (b) ZrO2 1200°C dwell temperature samples sintered with 50 MPa pressure at the same magnification

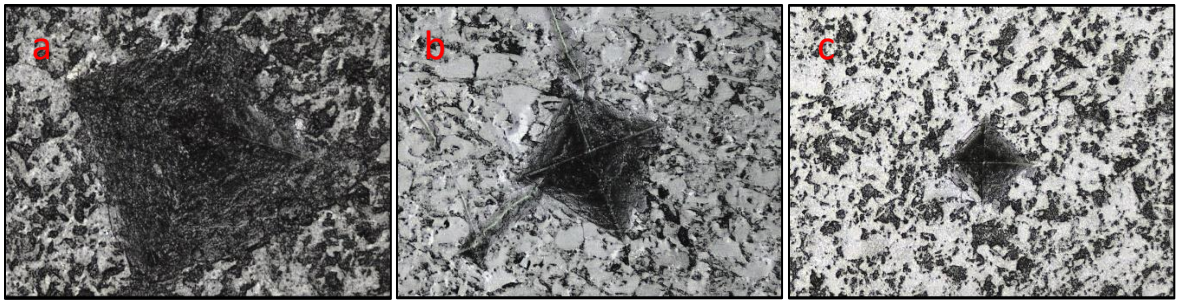

Figure 42: Vickers indentation images for (a) 400°C, (b) 600°C, and (c) 900°C dwell temperature samples sintered with 150 MPa pressure at the same magnification

Figure 43: Vickers indentation images for (a) 400°C, (b) 600°C, and (c) 900°C dwell temperature samples sintered with 300 MPa pressure at the same magnification

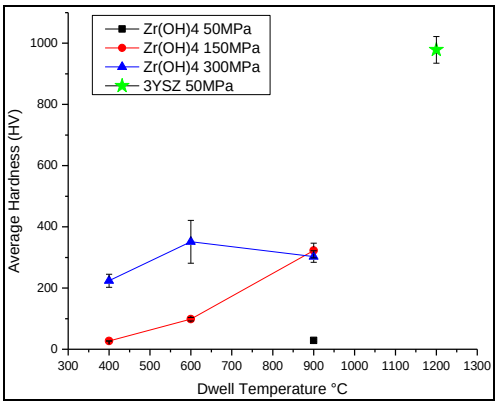

Figure 44: Comparison of Vickers hardness values for the samples with increased applied mechanical pressure

Table 15: Sintering time, sintering onset temperature, and force calculated from the SPS piston-displacement plots for the pure $Zr(OH)_4$ system sintered at 50 MPa dwell pressure

Dwell temperature	Sintering onset temperature	Sintering saturation temperature	Sintering onset time (mm:ss)	Sintering saturation time (mm:ss)	Sintering time (s)	Onset Force (kN)	Sintering saturation force (kN)	Sintering Force (kN)
400°C	393.00	400.00	18:22	20:55	153.00	15.75	16.00	0.25
500°C	385.00	500.00	18:14	22:30	256.00	13.00	16.00	3.00
600°C	394.00	600.00	18:20	24:05	345.00	12.20	16.00	3.80
800°C	573.00	800.00	24:25	34:45	620.00	12.50	16.00	3.50
900°C	447.00	900.00	18:15	26:35	500.00	11.20	16.00	4.80
1200°C	592.00	1200.00	25:14	38:53	799.00	10.00	16.00	6.00

Table 16: Sintering time, sintering onset temperature, and force calculated from the SPS piston-displacement plots for the pure $Zr(OH)_4$ system sintered at 150 MPa dwell pressure

Dwell temperature	Sintering onset temperature	Sintering saturation temperature	Sintering onset time (mm:ss)	Sintering saturation time (mm:ss)	Sintering time (in s)	Onset Force (kN)	Sintering saturation force (kN)	Sintering Force (kN)
400°C	346.00	400.00	14:30	16:00	90.00	42.00	47.00	5.00
600°C	395.00	600.00	14:50	19:52	302.00	31.00	47.00	16.00
900°C	443.00	900.00	15:35	26:25	650.00	22.00	47.00	25.00

Table 17: Sintering time, sintering onset temperature, and force calculated from the SPS piston-displacement plots for the pure $Zr(OH)_4$ system sintered at 300 MPa dwell pressure

Dwell temperature	Sintering onset temperature	Sintering saturation temperature	Sintering onset time (mm:ss)	Sintering saturation time (mm:ss)	Sintering time (s)	Onset Force (kN)	Sintering saturation force (kN)	Sintering Force (kN)
400°C	365.00	400.00	14:15	15:30	75.00	85.50	94.00	8.50
600°C	310.00	600.00	13:20	20:25	455.00	47.00	94.00	47.00
900°C	415.00	900.00	13:25	28:00	875.00	37.00	94.00	57.00

It is seen from the results from tables 15-17 and plots from figures 45 and 46 that for the pure $Zr(OH)_4$ composition irrespective of the applied mechanical pressure, the sintering onset temperature remains in the region 300°C to 500°C where the dehydration and conversion to oxides are in progress, but the sintering time is much higher for the 150 MPa and 300 MPa samples as the sintering begins earlier due to higher forces, and sintering occurs for a much larger period than the 50 MPa samples which also accounts for the better densification.

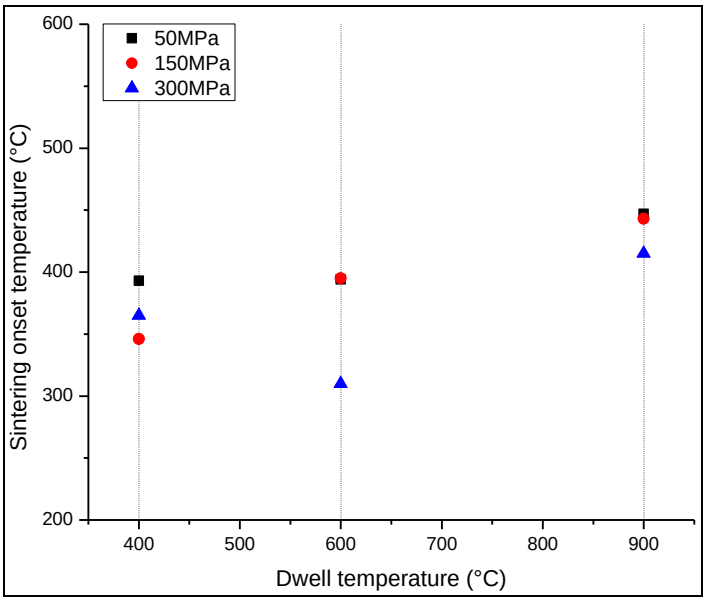

Figure 45: Comparison of sintering onset temperature for the samples sintered at different dwell pressures

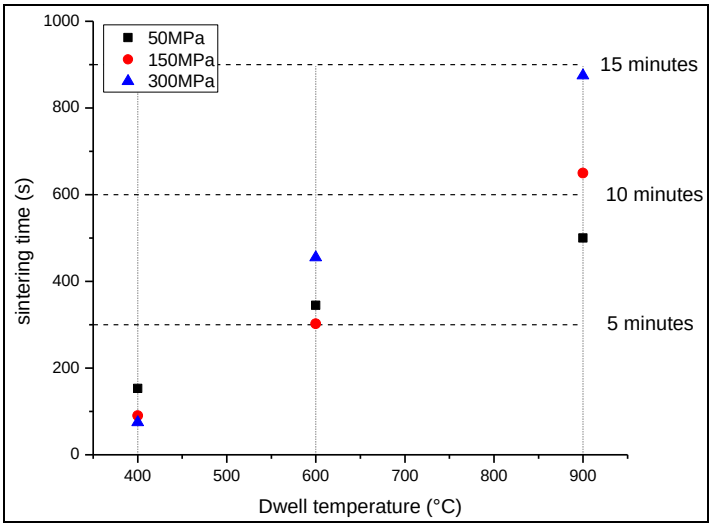

Figure 46: Comparison of sintering time for the samples sintered at different dwell pressures

5.4 Sintering aids

5.4.1 Bismuth Oxide

The sintering cycles were kept the same with 50°C/minute heating rate, 10-minute dwell time, and free-cooling. The highest densification with 50 MPa mechanical pressure at 900°C SPS is achieved by the 10wt% Bi_2O_3 system. The results are tabulated in table 19 plotted along with the preliminary (50 MPa) results in figure 47 for comparison.

Table 18: Sintering parameters for Bi_2O_3 sintering aid experiments

Sinter atmosphere	Vacuum
Mechanical Pressure at dwell stage	50 MPa (16kN)
Heating rate	50°C/min
Cooling rate	Free Cooling
Dwell time	10 minutes

Table 19: Relative density of 10wt% Bi2O3 doped $Zr(OH)_4$ sample

Sample	Initial mass (g)	Final mass (g)	Diameter (mm)	Thickness (mm)	Volume (cc)	Density (g/cc)	ZrO2+ X wt%Bi_2O_3 density (g/cc)	Relative density (%)
5wt% Bi_2O_3	5.00	4.07	20,36	4,62	1,50	2,71	6,16	43,99
	5.00	3.87	20,24	4,17	1,34	2,88	6,16	46,75
10wt% Bi_2O_3	5.00	3.82	20.79	2.46	0.83	4.57	6.30	72.63

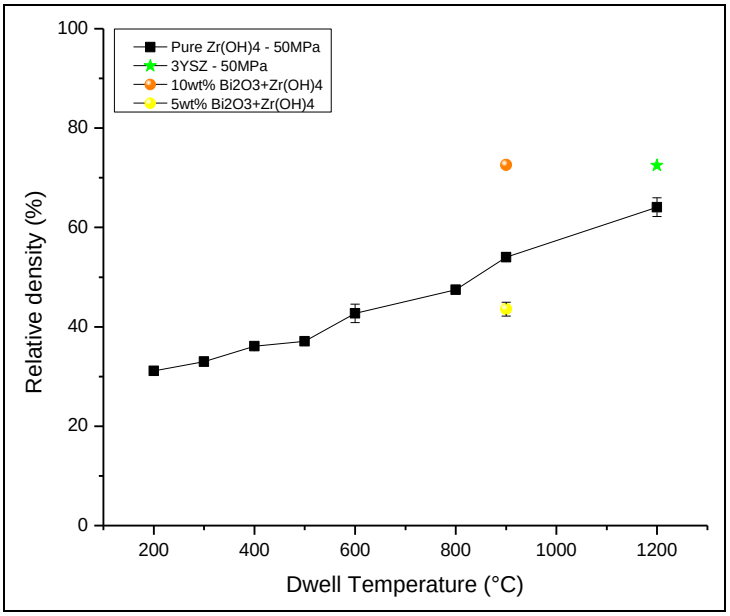

Figure 47: Improved densification at 50 MPa pressure sintering due to the addition of 10wt% Bi_2O_3

When Bismuth Oxide is mixed with $Zr(OH)_4$ and sintered at temperatures above its melting point of 817°C, the Bi_2O_3 melts and clogs the pores of the sintered sample and increases the density of the material as a whole by filling in the pores of the ZrO2 pellets. The melt also lubricates the grains and facilitates liquid phase sintering of the $Zr(OH)_4$ powders.

The microstructure of the 10wt% Bi_2O_3 sintered sample from figure 48 shows sintered grains. It can be inferred that indeed the sintering is better which is increasing the density. The sintering curve is shown in figure 49 and the sintering time, onset temperature is calculated in Appendix A. The values are tabulated in table 20 and plotted in figures 60 and 61 along with other results for comparison.

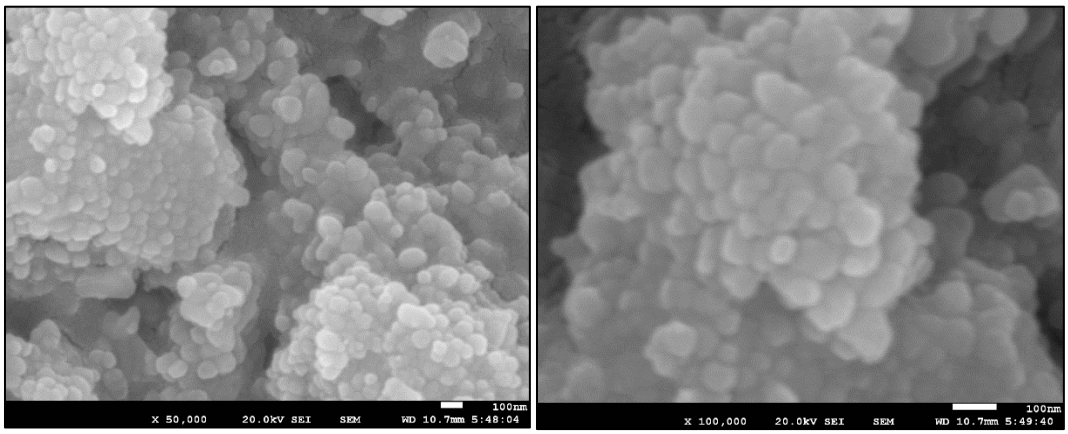

Figure 48: Microstructure of sintered Zr(OH)4 samples mixed with Bi_2O_3 sintering additive

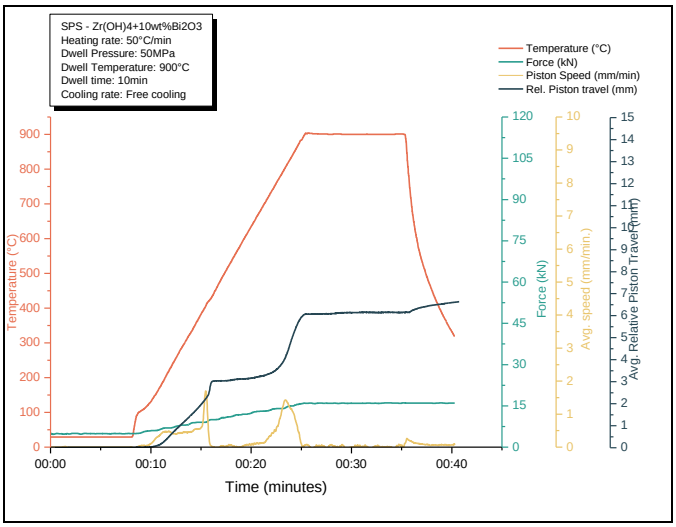

Figure 49: SPS piston-displacement curve with corresponding temperature and pressure changes for 10wt%Bi_2O_3-$Zr(OH)_4$ system

Table 20: Sintering time, sintering onset temperature and force calculated from the SPS piston-diplacement plots for the 10wt%Bi_2O_3-$Zr(OH)_4$ system

Sample	Sintering onset temperature	Sintering saturation temperature	Sintering onset time (mm:ss)	Sintering saturation time (mm:ss)	Sintering time (s)	Onset Force (kN)	Sintering saturation force (kN)	Sintering Force (kN)
10wt%Bi_2O_3-$Zr(OH)_4$	770.00	900.00	22:40	25:45	185.00	14.00	16.00	2.00

The hardness values are tabulated in table 21 and plotted in figure 50 along with other samples sintered until now. The hardness achieved by 10wt% Bi_2O_3 (6.59 GPa) is the highest in the sample set.

Table 21: Vickers hardness values for the samples from Bi_2O_3-$Zr(OH)_4$ systems

Sample	Average Hardness HV	Hardness (GPa)	Porosity (%)
5wt% Bi_2O_3-$Zr(OH)_4$	9.31	0.091331	54.63
10wt% Bi_2O_3-$Zr(OH)_4$	672.27	6.594969	27.37

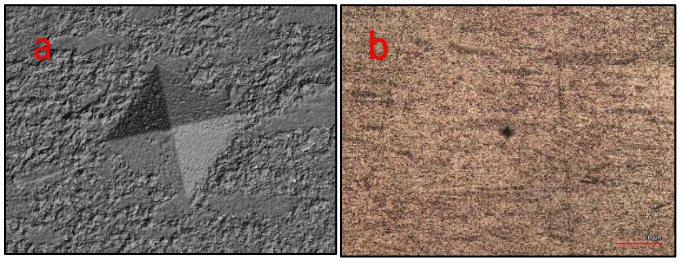

Figure 50: Vickers indentation images for (a) 5wt% Bi_2O_3-$Zr(OH)_4$ and (b) 10wt% Bi_2O_3-$Zr(OH)_4$ systems at the same magnification

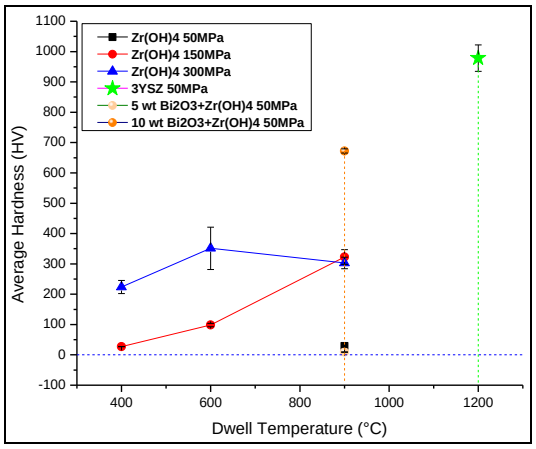

Figure 51: Comparison of Vickers hardness values for the Bi_2O_3-$Zr(OH)_4$ samples with those of increased applied mechanical pressure

5.4.2 Zirconium Hydride

The ZrH_2 powders are ball-mixed with the $Zr(OH)_4$ powders in the weight ratios 25wt% and 50wt% and are sintered by the SPS technique. The sintering cycles are kept the same with 50°C/minute heating rate, 10-minute dwell time at 900°C, and free-cooling. The pure ZrH_2 powders are also sintered with the same parameters for comparison.

Table 22: Sintering parameters for ZrH_2 sintering aid experiments

Sinter atmosphere	Vacuum
Mechanical Pressure at dwell stage	50 MPa (16kN)
Heating rate	50°C/min
Cooling rate	Free Cooling
Dwell time	10 minutes
Dwell temperature	900°C

The results from the SPS are tabulated in table 23. The sintering of pure ZrH_2 had no mass loss associated with it and had a better density. The microstructure of the sintered pure ZrH_2 sample shown in figure 54 shows sintered spherical aggregates with porosities. It can be seen from figures 52 and 53 that the mass loss associated with sintering decreases with the increase in ZrH_2 content in the system. Simultaneously, the density also increases with the increase in the ZrH_2 content in the system. The microstructures from figure 55 depict a similar level of sintering for both systems.

Table 23: Mass loss% and relative densities of $Zr(OH)_4$- ZrH_2 systems

ZrH_2 wt%	$Zr(OH)_4$ wt%	Initial mass(g)	Final mass (g)	Mass loss %	Diameter (mm)	Thickness(mm)	Volume (cc)	Density (g/cc)	Ideal density (g/cc)	Relative density %
0	100	6.53	4.40	32.68	20.26	4.21	1.36	3.24	6.10	53.12
0	100	6.53	5.08	22.24	20.35	4.66	1.51	3.35	6.10	54.95
25	75	5.00	4.24	15.12	20.47	3.73	1.23	3.46	5.94	58.29
25	75	5.00	4.25	15.06	20.55	3.43	1.14	3.74	5.94	62.94
50	50	5.00	4.61	7.86	20.41	3.59	1.17	3.93	5.81	67.59
50	50	5.00	4.48	10.50	20.37	3.39	1.11	4.05	5.81	69.68
100	0	5.00	5.00	0.00	20.58	3.36	1.12	4.48	5.54	80.90
100	0	5.00	5.00	0.00	20.69	3.61	1.21	4.12	5.54	74.40

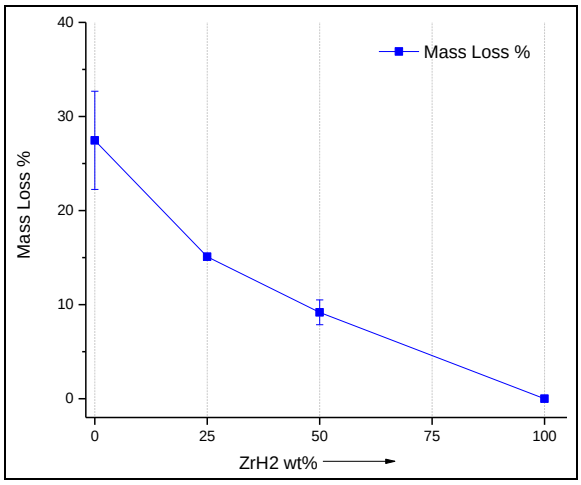

Figure 52: Mass loss% vs $Zr(OH)_4$-ZrH_2 system composition

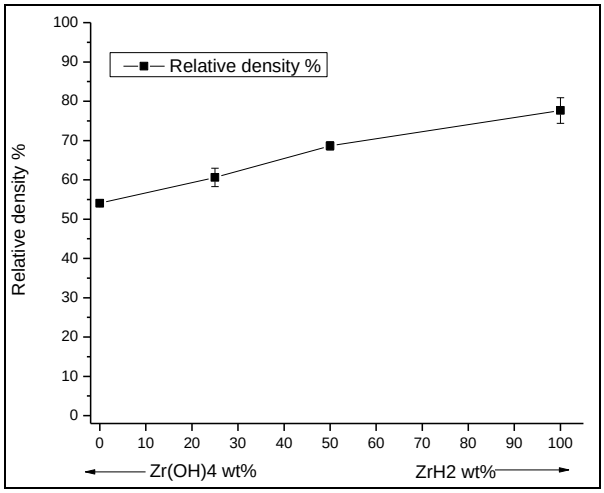

Figure 53: Relative densities of $Zr(OH)_4$-ZrH_2 system composition

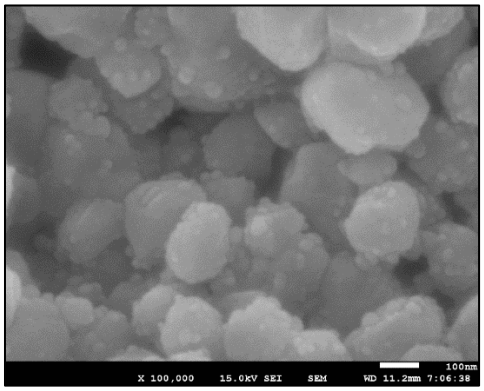

Figure 54: Microstructure of pure ZrH_2 sintered at 900°C under 50 MPa pressure

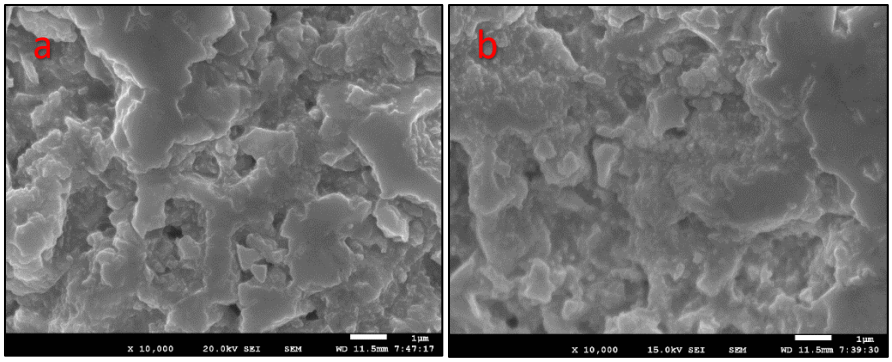

Figure 55: Microstructure of (a) 25wt% ZrH_2-$Zr(OH)_4$ system and (b) 50wt% ZrH_2-$Zr(OH)_4$ system sintered at 900°C under 50 MPa pressure

The piston displacement curve for the pure ZrH_2 system from figure 56 shows an S-shaped sintering curve with an onset at 558°C closer to the value from the literature (575°C) [22]. The curves for the 25wt% and 50wt% ZrH_2 systems shown in figure 57 show a two-fold sintering curve. The former is from the densification of $Zr(OH)_4$ and the latter is similar to the sintering curve from ZrH_2 sintering due to the dehydrogenation of ZrH_2. The two-fold sintering provides enhanced densification to the powder particles. The sintering time, onset temperature is calculated in Appendix A. The values are tabulated in table 24 and plotted in figures 60 and 61 along with other results for comparison.

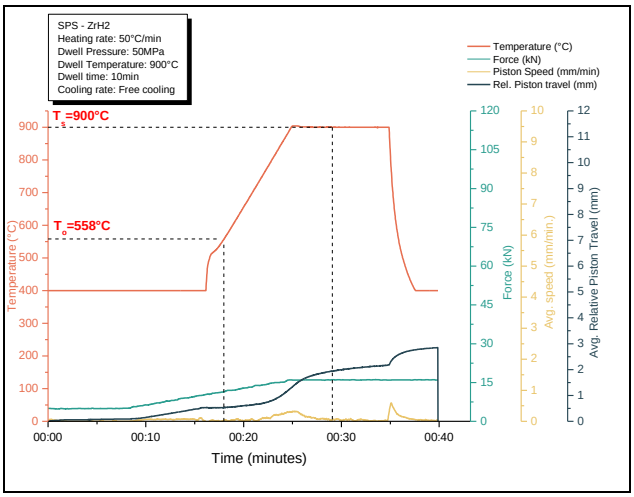

Figure 56: SPS piston-displacement curve with corresponding temperature and pressure changes for pure ZrH_2

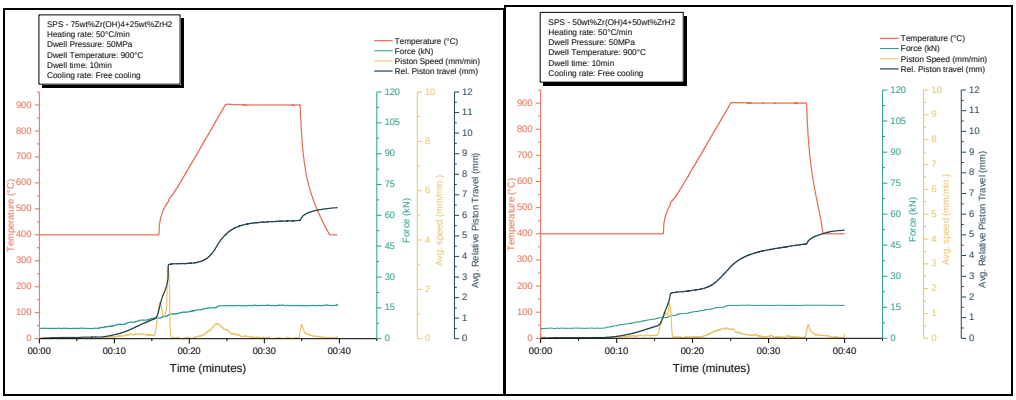

Figure 57: SPS piston-displacement curve with corresponding temperature and pressure changes for ZrH_2:$Zr(OH)_4$ system: [left] 25wt% ZrH_2-$Zr(OH)_4$ and [right] 50wt% ZrH_2-$Zr(OH)_4$

Table 24: Sintering time, sintering onset temperature, and force calculated from the SPS piston-displacement plots for the ZrH_2-$Zr(OH)_4$ system

Sample	Sintering onset temperature	Sintering saturation temperature	Sintering onset time (mm:ss)	Sintering saturation time (mm:ss)	Sintering time (s)	Onset Force (kN)	Sintering saturation force (kN)	Sintering Force (kN)
75wt%$Zr(OH)_4$+25wt%ZrH_2	762.00	900.00	22:05	30:10	485.00	14.60	16.00	1.40
50wt%$Zr(OH)_4$+50wt%ZrH_2	770.00	900.00	22:30	29:20	410.00	14.30	16.00	1.70

The Vickers hardness for the ZrH_2-$Zr(OH)_4$ systems is tabulated in table 25 and plotted in figure 59 with other results for comparison. It is seen from them that the hardness of the ZrH_2 sintering aid systems is better than the values for pure $Zr(OH)_4$ pellets but lower than the values from increased dwell pressure systems.

Table 25: Vickers hardness values for the samples from ZrH_2-$Zr(OH)_4$ system

Sample	Average Hardness	Hardness (GPa)	Porosity (%)
Pure $Zr(OH)_4$	29.04	0.284882	45.96
$Zr(OH)_4$-75wt% + ZrH_2-25wt%	46.53	0.456459	39.39
$Zr(OH)_4$-50wt% + ZrH_2-50wt%	76.94	0.754781	31.36
Pure ZrH_2	228.39	2.240506	22.35

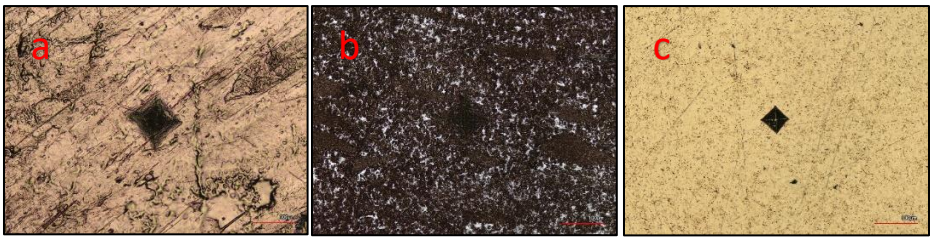

Figure 58: Vickers indentation images for (a) 25wt% ZrH_2 -$Zr(OH)_4$ and (b) 50wt% ZrH_2-$Zr(OH)_4$ systems and (c) pure ZrH_2 sintered at 900°C and 50 MPa (at the same magnification)

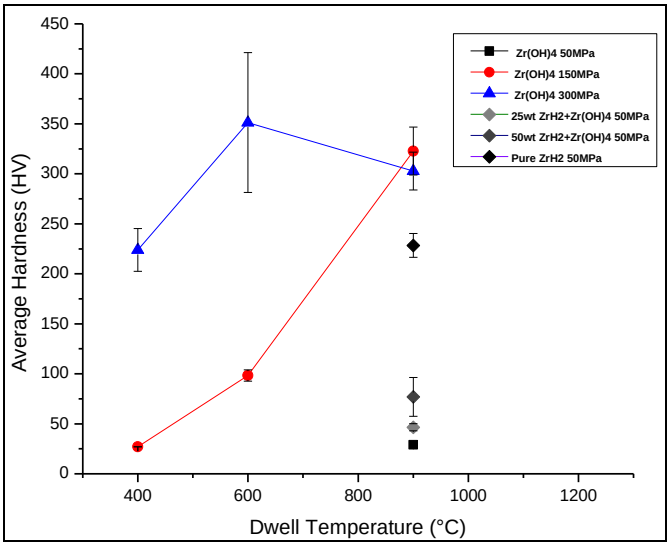

Figure 59: Comparison of Vickers hardness values for the ZrH_2-$Zr(OH)_4$ samples with those of increased applied mechanical pressure

5.4.3 Comparison of the Bi_2O_3 system Vs the ZrH_2 system as sintering aids

The plots from figures 60 and 61 depict the onset sintering temperature and sintering time for each of the different conditions applied for better densification of the $Zr(OH)_4$ powders. The ZrH_2-$Zr(OH)_4$ systems start sintering at around 760°C and take a much smaller time than the pure $Zr(OH)_4$ powders and are also denser than the pure powders. The 10wt% Bi_2O_3-$Zr(OH)_4$ system sintered the best at 900°C with 50 MPa mechanical pressure with the smallest sintering time.

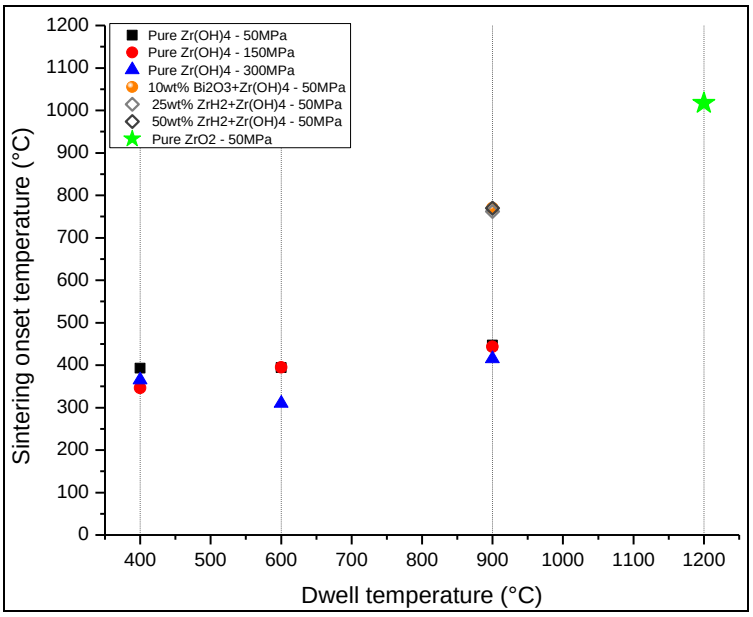

Figure 60: Comparison of sintering onset temperature of all the densified samples

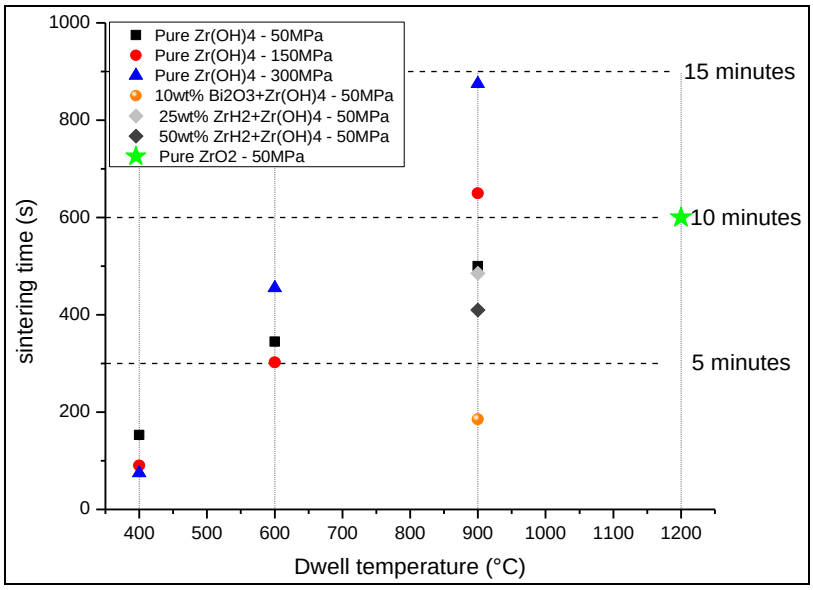

Figure 61: Comparison of sintering time of all the densified samples

The plots from Figures 62 and 63 depict the variation of relative densities and hardness of all the sintered systems. Also, the value from experiments conducted by Estournès *et. al.* [28] is added for comparison. The results depict that the 10wt% Bi_2O_3 system, 50wt% ZrH_2 system, and the 150 MPa & 300 MPa pure $Zr(OH)_4$ systems all sintered at 900°C dwell temperatures have the relative densities in the proximity of the results from the mentioned literature. Also, comparing the hardness values, it can be said that the pure $Zr(OH)_4$ sample sintered at 300 MPa dwell pressure and 900°C dwell temperature had a similar hardness value as the one from the literature and the hardness of 10wt% Bi_2O_3 sample (6.59GPa) sintered at 900°C dwell temperature surpassed the value from literature (3.805GPa).

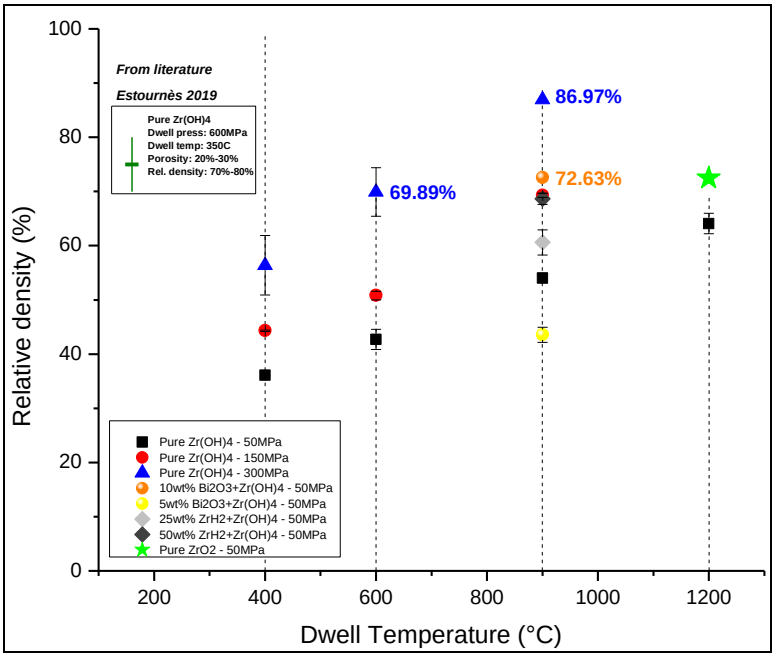

Figure 62: Comparison of relative densities of all the sintered samples

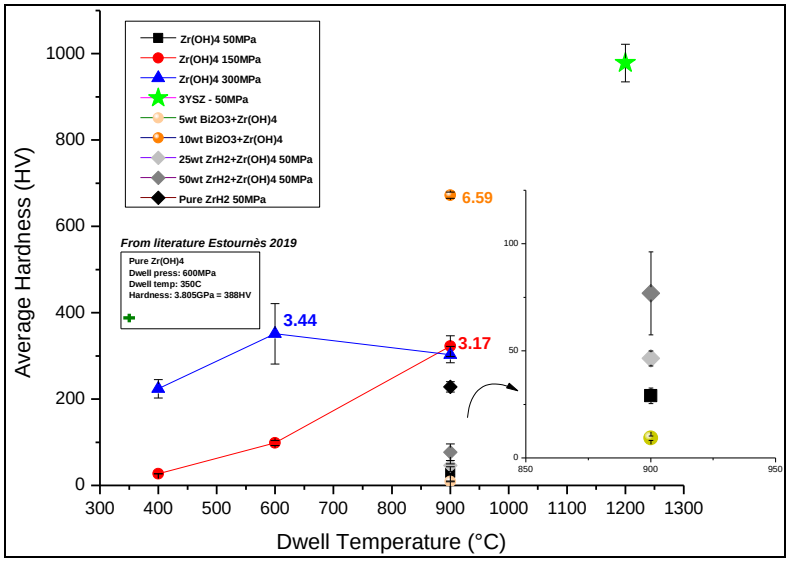

Figure 63: Comparison of hardness values of all the sintered samples

6. PHASE STABILIZATION

6.1 Doping with Yttrium oxide

It is known from previous studies [35][11] that undersized trivalent dopants state can stabilize the tetragonal phases of Zirconia. The most popular undersized dopant used to stabilize ZrO_2 is Yttrium oxide (Y_2O_3). The most used dopants to avoid monoclinic conversion are 2-3 mol% and 8 mol% Y_2O_3. The creation of Oxygen vacancies around the Zr^{4+} ion relaxes the crystal structure and stabilizes the tetragonal phases.

In this experiment, the $Zr(OH)_4$ powders are doped with 3mol% Y_2O_3 and 8mol% Y_2O_3 to stabilize the tetragonal phases in ZrO_2 formed after conversion during the sintering process. The sintering cycles were kept the same with 50°C/minute heating rate, 10-minute dwell time, and free-cooling.

Table 26: Sintering parameters for Y_2O_3-$Zr(OH)_4$ experiments

Sinter atmosphere	Vacuum
Mechanical Pressure at dwell stage	50 MPa (16kN)
Heating rate	50°C/min
Cooling rate	Free Cooling
Dwell time	10 minutes
Dwell temperature	900°C

The XRD analysis is performed on the sintered powders (from pellets) and the results are shown in figure 65. Upon sintering, the 8mol% Y_2O_3 system had a higher tetragonal phase stabilization effect as compared to the 3mol% Y_2O_3 system. The doped systems had more tetragonal phases compared to the pure $Zr(OH)_4$ sintered powders.

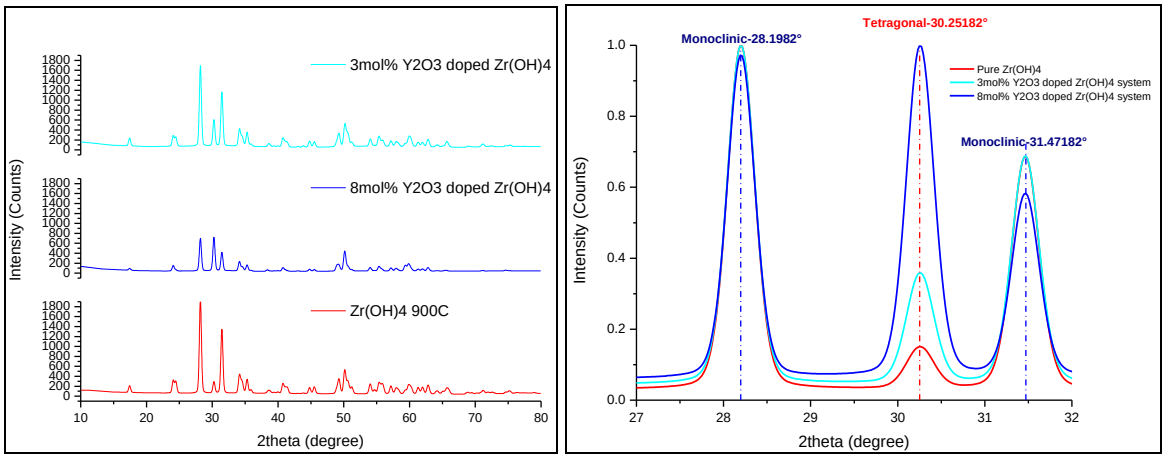

Figure 64: XRD plots of sintered pure $Zr(OH)_4$ (bottom), sintered 3mol% Y_2O_3 doped $Zr(OH)_4$ (centre), and sintered 8mol% Y_2O_3 doped $Zr(OH)_4$ (top) samples along with maximized characteristic peaks (on the right side)

6.2 Doping with Bi_2O_3

Similar to Y_2O_3, the oversized trivalent dopant Bi_2O_3 is also expected to stabilize the tetragonal phases of the Zirconia [36][21]. In this experiment, the $Zr(OH)_4$ powders are doped with 5wt% and 10wt% Bi_2O_3 to stabilize the tetragonal phases in the sinter-formed ZrO_2 at room temperature. The sintering cycles were kept the same with a 50°C/minute heating rate, a 10-minute dwell time at 900°C, and free-cooling.

Table 27: Sintering parameters for Bi_2O_3-$Zr(OH)_4$ experiments

Sinter atmosphere	Vacuum
Mechanical Pressure at dwell stage	50 MPa (16kN)
Heating rate	50°C/min
Cooling rate	Free Cooling
Dwell time	10 minutes
Dwell temperature	900°C

The XRD analysis was performed on the sintered powders (from pellets) and the results are as shown in figure 66. Upon sintering, the 10wt% Bi_2O_3 system had a higher tetragonal phase stabilization effect as compared to the 5wt% Bi_2O_3 system. The doped systems had more tetragonal phases compared to the pure $Zr(OH)_4$ sintered powders.

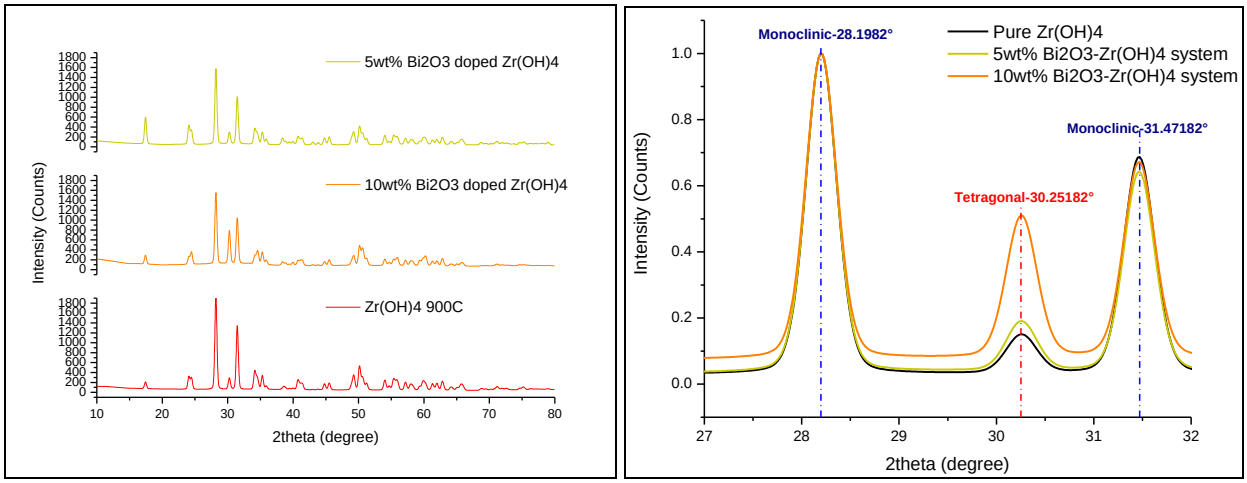

Figure 65: XRD plots of sintered pure $Zr(OH)_4$ (bottom), sintered 10wt% Bi_2O_3 doped $Zr(OH)_4$ (centre), and sintered 5wt% Bi_2O_3 doped $Zr(OH)_4$ (top) samples along with maximized characteristic peaks (on the right side)

6.3 Doping with ZrH_2

In this experiment, the $Zr(OH)_4$ powders are doped with 25wt% and 50wt% ZrH_2 to see if they still stabilize the tetragonal phases of the sinter formed ZrO_2 at room temperature. The sintering cycles were kept the same with 50°C/minute heating rate, 10-minute dwell time, and free-cooling.

Table 28: Sintering parameters for ZrH_2-$Zr(OH)_4$ experiments

Sinter atmosphere	Vacuum
Mechanical Pressure at dwell stage	50 MPa (16kN)
Heating rate	50°C/min
Cooling rate	Free Cooling
Dwell time	10 minutes
Dwell temperature	900°C

The XRD analysis was performed on sintered powders (from pellets) and the results as shown in figure 57. Upon sintering, both the ZrH_2 systems had lower tetragonal phase stabilization effects compared to the pure $Zr(OH)_4$ sintered powders.

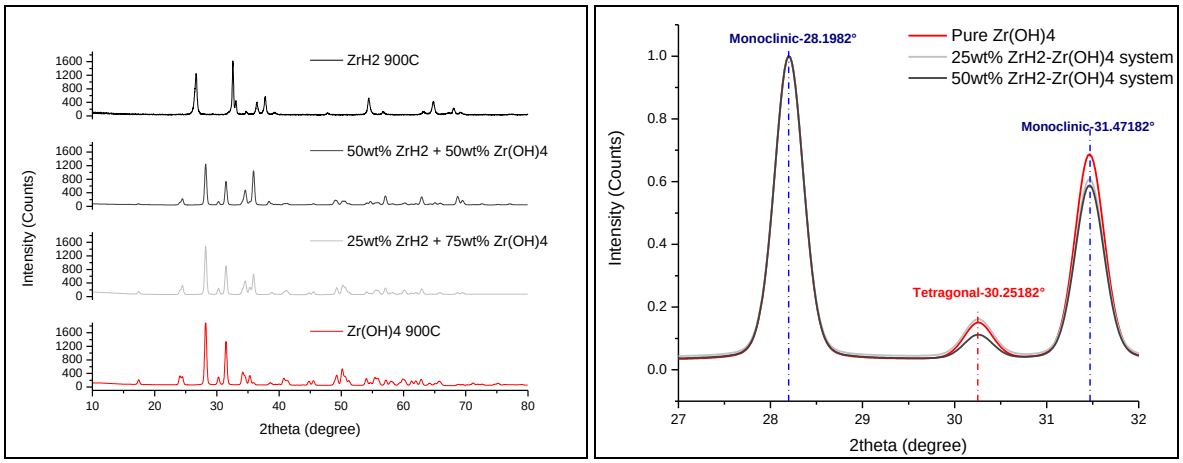

Figure 66: XRD plots of sintered pure $Zr(OH)_4$ (bottom), sintered 25wt% ZrH2-$Zr(OH)_4$ (centre), and sintered 50wt% ZrH2-$Zr(OH)_4$ (top) samples along with maximized characteristic peaks (on the right side)

6.4 Comparison of the Y_2O_3-$Zr(OH)_4$ system, Bi_2O_3-$Zr(OH)_4$ system, and ZrH_2-$Zr(OH)_4$ system as tetragonal phase stabilizers

The complete set of phase stabilization results from the XRD analysis are normalized and plotted for comparison in figure 68 which depicts that the 8mol% Y_2O_3 systems followed by the 10wt% Bi_2O_3 systems had the best stabilization effect among the doped and pure $Zr(OH)_4$ systems. The 3mol% Y_2O_3 system also stabilized the tetragonal phases better than the pure powders. 5wt% Bi_2O_3 and 25wt%ZrH_2-$Zr(OH)_4$ showed a similar stabilization as that of the pure $Zr(OH)_4$ powders.

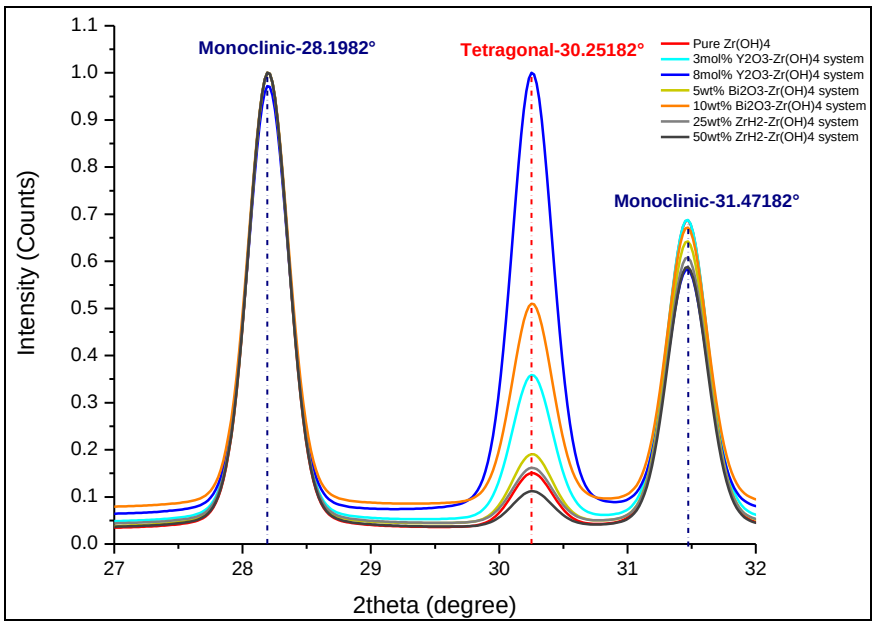

Figure 67: XRD plots of all the phase stabilization systems along with that of pure powders with normalized peaks

7. THERMAL CONDUCTIVITY

The thermal conductivity values are measured using the Hot Disk TPS 2200 machine are tabulated in table 29 and plotted in figure 69. The results suggest that the thermal conductivity values are dependent on the porosity of the samples and reached a maximum when the porosity is around 50%. This is due to the large contribution to thermal conduction via both conduction and radiation whereas it remained lower for porosities on either side of the 50% porosity as the thermal conductivity is mainly attributed to conduction in the case of low porous (high density) samples and radiation in the case of high porous (low density) samples.

Table 29: Thermal conductivity of samples sintered at various dwell temperatures and mechanical pressures.

Sample	Dwell temperature	Dwell Mech. press.	Thermal conductivity (W/mK)
Zr(OH)4	400	50	0.6113
Zr(OH)4	400	50	0.6254
Zr(OH)4	600	50	0.8783
Zr(OH)4	600	50	0.7036
Zr(OH)4	900	50	1.611
Zr(OH)4	900	50	1.271
Zr(OH)4	1200	50	0.4215
Zr(OH)4	1200	50	0.4643
Zr(OH)4	400	150	0.608
Zr(OH)4	400	150	0.6131
Zr(OH)4	600	150	1.074
Zr(OH)4	600	150	1.009
Zr(OH)4	900	150	0.506
Zr(OH)4	900	150	0.4575

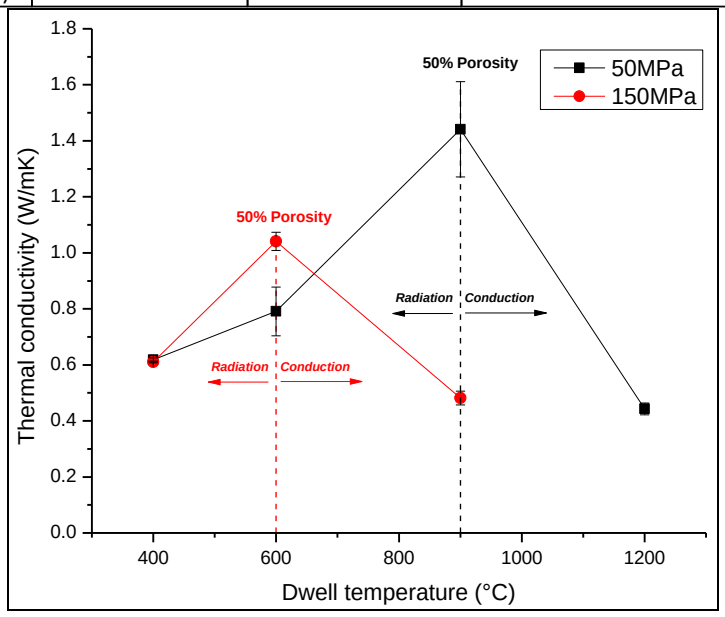

Figure 68: Thermal conductivity of samples sintered at various dwell temperatures and mechanical pressures.

8. CONCLUSION

Zirconium oxide - ZrO_2 (a.k.a Zirconia) is a very essential material in the ceramic family of materials and is a major component of many applications in the field of aerospace engineering, biomedical, solid-fuel, and many other industries. The production of the components made from Zirconia is either sprayed as a coating or sintered through traditional and non-traditional ways. With the advent of field-assisted sintering techniques like 'Spark Plasma Sintering', the compaction of ceramics and metal powders has reached new levels of densification with quicker sintering times. Nevertheless, the sintering temperatures for densifying pure Zirconia remain higher in the range - 1200°C to 1400°C which is expensive. The sintering temperature can be brought to lower values by adopting the novel 'Cold sintering process' which involves lowering the temperature at which the material sinters by making the conditions favourable for the reduction in surface areas of the materials by reducing Gibb's surface energy at lower temperatures. One such attempt at sintering Zirconia through cold sintering of precursor Zirconium hydroxide powders is performed in this thesis work. Also, the stabilization of tetragonal phases of Zirconia is essential for its application in various high-temperature applications to avoid the phase transformation from monoclinic phase is performed, neglecting which may result in failures due to stresses accumulated in the bulks by this transformation.

Preliminary sintering was performed on the amorphous pure Zirconium hydroxide powders at different dwell temperatures and a dwell pressure of 50 MPa. The results from this experiment helped determine the crystallization temperature, oxide conversion temperature, sintering profiles at different dwell temperatures, and the phases formed at those dwell temperatures.

The information from the preliminary experiments and the extensive literature study helped design various sintering experiments to densify the samples at lower temperatures. Parameters like dwell time and powder sizes were varied which incurred very less/no changes in the densification of the bulks. The applied mechanical pressures increased from 50 MPa to 150 MPa and 300 MPa using higher strength mould-punch systems showed a substantial increase in the relative densities and hardness of the materials even at low temperatures like 400°C and 600°C. Sintering aids like Bi_2O_3, ZrH_2 are also added in substantial quantities to improve the sintering which indeed showed better results than the preliminary experiments. The 10wt% Bi_2O_3-$Zr(OH)_4$ system had a density of 72.63% with a hardness value of 6.59GPa which is the highest in the whole sample set. The pure $Zr(OH)_4$ sample sintered at 900°C and 300 MPa dwell conditions had the highest relative density of 86.97%.

Additionally, the tetragonal phases of the Zirconia are stabilized at room temperatures by doping the samples with trivalent compounds like Yttrium oxide Y_2O_3, Bismuth oxide Bi_2O_3, and additionally with Zirconium hydride ZrH_2. The results obtained showed that the 5wt% Bi_2O_3 and 25wt% $Zr(OH)_4$ showed the same level of stabilization as the pure $Zr(OH)_4$ powders whereas, the 10wt% Bi_2O_3-$Zr(OH)_4$, 8mol% Y_2O_3-$Zr(OH)_4$, and 3mol% Y_2O_3-$Zr(OH)_4$ systems showed higher levels of tetragonal phase stabilization in the order:

8mol% Y_2O_3-$Zr(OH)_4$ > 10wt% Bi_2O_3-$Zr(OH)_4$ > 3mol% Y_2O_3-$Zr(OH)_4$

Finally, it can be concluded that by adopting higher mechanical dwell pressures and with the addition of sintering aids like ZrH_2 and Bi_2O_3, the densities of the samples can be improved, and the stabilization of tetragonal phases can be achieved by doping with trivalent compounds like Y_2O_3 and Bi_2O_3 even at lower temperatures like 600°C and 900°C.

9. FURTHER STUDIES

1. Like trivalent cations, even the tetravalent cations like GeO_2 and CeO_2 also stabilize the tetragonal phases of the ZrO_2 by relaxation of the oxygen bonds with the dopant [35], Hence, these powders can be used as dopants to the pure $Zr(OH)_4$ powders for stabilizing the ZrO_2 tetragonal phases in the end product after sintering.

2. Doping of pure $Zr(OH)_4$ powders with pentavalent cations like Ta_2O_5 to check the phase stabilization with respect to tetragonal and cubic phases of ZrO_2 could be performed

3. Use of polymeric sintering aids like Polyvinyl butyrate, Polyethylene glycol, etc. to densify the end products from SPS

4. Use of other ceramic systems like Fe_2O_3, SiO_2 as sintering aids to densify the end products from SPS

5. Another way of achieving highly dense ZrO_2 sintered products at lower temperatures is to start with an optimally packed powder system. This could be achieved using bimodal powder systems [$Zr(OH)_4$ nano powders mixed with $Zr(OH)_4$ micro powders in certain ratios] and sintering them using SPS

6. Since, ZrH_2 shows a promising sintering under SPS, research could be done on Spark Plasma Sintering of ZrH_2 powders

7. The sintering profiles of ZrH_2-$Zr(OH)_4$ systems seems interesting and hence, optimization of the sintering parameters for ZrH_2-$Zr(OH)_4$ systems for producing high density systems could be researched

8. The melt fusion sintering from the Bi_2O_3-$Zr(OH)_4$ system can be optimized to obtain samples with high density and high hardness and further optimization can be done to obtain cubic or tetragonal phase stabilization by Bi_2O_3

REFERENCES

[1] Q. Liu, S. Huang, and A. He, "Composite ceramics thermal barrier coatings of yttria stabilized zirconia for aero-engines," *J. Mater. Sci. Technol.*, vol. 35, no. 12, pp. 2814–2823, 2019, doi: https://doi.org/10.1016/j.jmst.2019.08.003.

[2] P. G. Lashmi, P. V Ananthapadmanabhan, G. Unnikrishnan, and S. T. Aruna, "Present status and future prospects of plasma sprayed multilayered thermal barrier coating systems," *J. Eur. Ceram. Soc.*, vol. 40, no. 8, pp. 2731–2745, 2020, doi: https://doi.org/10.1016/j.jeurceramsoc.2020.03.016.

[3] J. G. Thakare, C. Pandey, M. M. Mahapatra, and R. S. Mulik, "Thermal Barrier Coatings—A State of the Art Review," *Met. Mater. Int.*, 2020, doi: 10.1007/s12540-020-00705-w.

[4] N. P. Padture, M. Gell, and E. H. Jordan, "Thermal Barrier Coatings for Gas-Turbine Engine Applications," *Science (80-.).*, vol. 296, no. 5566, pp. 280 LP – 284, Apr. 2002, doi: 10.1126/science.1068609.

[5] Z.-Y. Hu, Z.-H. Zhang, X.-W. Cheng, F.-C. Wang, Y.-F. Zhang, and S.-L. Li, "A review of multi-physical fields induced phenomena and effects in spark plasma sintering: Fundamentals and applications," *Mater. Des.*, vol. 191, p. 108662, 2020, doi: https://doi.org/10.1016/j.matdes.2020.108662.

[6] T. S. Hille, T. J. Nijdam, A. S. J. Suiker, S. Turteltaub, and W. G. Sloof, "Damage growth triggered by interface irregularities in thermal barrier coatings," *Acta Mater.*, vol. 57, no. 9, pp. 2624–2630, 2009, doi: 10.1016/j.actamat.2009.01.022.

[7] A. Fregeac, F. Ansart, S. Selezneff, and C. Estournès, "Relationship between mechanical properties and microstructure of yttria stabilized zirconia ceramics densified by spark plasma sintering," *Ceram. Int.*, vol. 45, no. 17, pp. 23740–23749, 2019, doi: 10.1016/j.ceramint.2019.08.090.

[8] H. Aleksanoglu *et al.*, "Determining a critical strain for APS thermal barrier coatings under service relevant loading conditions," *Int. J. Fatigue*, vol. 53, pp. 40–48, 2013, doi: 10.1016/j.ijfatigue.2011.11.018.

[9] J. Chevalier, L. Gremillard, A. V Virkar, and D. R. Clarke, "The Tetragonal-Monoclinic Transformation in Zirconia: Lessons Learned and Future Trends," *J. Am. Ceram. Soc.*, vol. 92, no. 9, pp. 1901–1920, Sep. 2009, doi: https://doi.org/10.1111/j.1551-2916.2009.03278.x.

[10] R. H. J. Hannink, P. M. Kelly, and B. C. Muddle, "Transformation Toughening in Zirconia-Containing Ceramics," *J. Am. Ceram. Soc.*, vol. 83, no. 3, pp. 461–487, Mar. 2000, doi: https://doi.org/10.1111/j.1151-2916.2000.tb01221.x.

[11] P. Li, I.-W. Chen, and J. E. Penner-Hahn, "Effect of Dopants on Zirconia Stabilization—An X-ray Absorption Study: I, Trivalent Dopants," *J. Am. Ceram. Soc.*, vol. 77, no. 1, pp. 118–128, Jan. 1994, doi: https://doi.org/10.1111/j.1151-2916.1994.tb06964.x.

[12] O. Guillon *et al.*, "Field-assisted sintering technology/spark plasma sintering: Mechanisms, materials, and technology developments," *Adv. Eng. Mater.*, vol. 16, no. 7, pp. 830–849, 2014, doi: 10.1002/adem.201300409.

[13] E. A. Olevsky, W. L. Bradbury, C. D. Haines, D. G. Martin, and D. Kapoor, "Fundamental

aspects of spark plasma sintering: I. Experimental analysis of scalability," *J. Am. Ceram. Soc.*, vol. 95, no. 8, pp. 2406–2413, 2012, doi: 10.1111/j.1551-2916.2012.05203.x.

[14] M. Biesuz and V. M. Sglavo, "Flash sintering of ceramics," *J. Eur. Ceram. Soc.*, vol. 39, no. 2, pp. 115–143, 2019, doi: https://doi.org/10.1016/j.jeurceramsoc.2018.08.048.

[15] G. Lee *et al.*, "Effect of electric current on densification behavior of conductive ceramic powders consolidated by spark plasma sintering," *Acta Mater.*, vol. 144, pp. 524–533, 2018, doi: 10.1016/j.actamat.2017.11.010.

[16] N. Takekazu, M. Yokota, M. Nose, S. Tomida, T. Kamiya, and S. Saji, "Effects of Pulse Current on an Aluminum Powder Oxide Layer During Pulse Current Pressure Sintering," *Mater. Trans. - MATER TRANS*, vol. 43, pp. 1390–1397, Jun. 2002, doi: 10.2320/matertrans.43.1390.

[17] Z. A. Munir, U. Anselmi-Tamburini, and M. Ohyanagi, "The effect of electric field and pressure on the synthesis and consolidation of materials: A review of the spark plasma sintering method," *J. Mater. Sci.*, vol. 41, no. 3, pp. 763–777, 2006, doi: 10.1007/s10853-006-6555-2.

[18] H. Guo, A. Baker, J. Guo, and C. A. Randall, "Protocol for Ultralow-Temperature Ceramic Sintering: An Integration of Nanotechnology and the Cold Sintering Process," *ACS Nano*, vol. 10, no. 11, pp. 10606–10614, Nov. 2016, doi: 10.1021/acsnano.6b03800.

[19] H. Guo, A. Baker, J. Guo, and C. A. Randall, "Cold Sintering Process: A Novel Technique for Low-Temperature Ceramic Processing of Ferroelectrics," *J. Am. Ceram. Soc.*, vol. 99, no. 11, pp. 3489–3507, Nov. 2016, doi: 10.1111/jace.14554.

[20] H. Guo, J. Guo, A. Baker, and C. A. Randall, "Cold sintering process for ZrO2-based ceramics: significantly enhanced densification evolution in yttria-doped ZrO2," *J. Am. Ceram. Soc.*, vol. 100, no. 2, pp. 491–495, Feb. 2017, doi: 10.1111/jace.14593.

[21] A. Gulino, S. La Delfa, I. Fragalà, and R. G. Egdell, "Low-Temperature Stabilization of Tetragonal Zirconia by Bismuth," *Chem. Mater.*, vol. 8, no. 6, pp. 1287–1291, Jan. 1996, doi: 10.1021/cm950558j.

[22] O. S. Petukhov, A. V Ragulya, and H. Y. Borodianska, "Synthesis of the ZrN–ZrB2 Composite by Spark Plasma Sintering," *Powder Metall. Met. Ceram.*, vol. 58, no. 7–8, pp. 416–430, 2019, doi: 10.1007/s11106-019-00091-y.

[23] A. V Hmelov and I. Shteins, "Properties of mullite-zirconium ceramic obtained by spark plasma sintering," *Glas. Ceram.*, vol. 68, no. 11, pp. 399–404, 2012, doi: 10.1007/s10717-012-9399-z.

[24] R. Martin, M. Vick, R. K. Enneti, and S. V Atre, "Powder Injection Molding of Ceria-Stabilized, Zirconia-Toughened Mullite Parts for UAV Engine Components," *JOM*, vol. 65, no. 11, pp. 1388–1394, 2013, doi: 10.1007/s11837-013-0673-5.

[25] X. Yang, J. Yang, X. Xu, Q. Liu, Z. Xie, and W. Liu, "Injection molding of ultra-fine Si3N4 powder for gas-pressure sintering," *Int. J. Miner. Metall. Mater.*, vol. 22, no. 6, pp. 654–659, 2015, doi: 10.1007/s12613-015-1119-6.

[26] N. Chuankrerkkul, T. Wasanapiarnpong, and K. Noomun, "Powder injection moulding of dental ceramic brackets using water soluble binder," *Chiang Mai J. Sci.*, vol. 45, pp. 2190–2194, Aug. 2018.

[27] J. H. Park *et al.*, "Ultra-fast fabrication of tape-cast anode supports for solid oxide fuel cells via resonant acoustic mixing technology," *Ceram. Int.*, vol. 45, no. 9, pp. 12154–12161,

2019, doi: https://doi.org/10.1016/j.ceramint.2019.03.119.
[28] C. Elissalde *et al.*, “Single-step sintering of zirconia ceramics using hydroxide precursors and Spark Plasma Sintering below 400 °C,” *Scr. Mater.*, vol. 168, pp. 134–138, 2019, doi: https://doi.org/10.1016/j.scriptamat.2019.04.037.
[29] J.-P. Maria *et al.*, “Cold sintering: Current status and prospects,” *J. Mater. Res.*, vol. 32, no. 17, pp. 3205–3218, 2017, doi: DOI: 10.1557/jmr.2017.262.
[30] T. Hérisson de Beauvoir, F. Molinari, U. C. Chung-Seu, D. Michau, D. Denux, and M. Josse, “Densification of MnSO4 ceramics by Cool-SPS: Evidences for a complex sintering mechanism and magnetoelectric coupling,” *J. Eur. Ceram. Soc.*, vol. 38, no. 11, pp. 3867–3874, 2018, doi: https://doi.org/10.1016/j.jeurceramsoc.2018.04.005.
[31] T. Herisson de Beauvoir *et al.*, “Cool-SPS stabilization and sintering of thermally fragile, potentially magnetoelectric, NH4FeP2O7,” *Ceram. Int.*, vol. 45, no. 7, Part B, pp. 9674–9678, 2019, doi: https://doi.org/10.1016/j.ceramint.2018.12.103.
[32] C. Piconi and A. A. Porporati, “Bioinert Ceramics: Zirconia and Alumina BT - Handbook of Bioceramics and Biocomposites,” I. V. Antoniac, Ed. Cham: Springer International Publishing, 2016, pp. 59–89.
[33] M. G. Mulaudzi, “AB initio study of structural stability and electronic properties of ZrO2-xSx for 0,” 2015.
[34] H. T. Rijnten, “No Title,” TU Delft, 1971.
[35] P. Li, I.-W. Chen, and J. E. Penner-Hahn, “Effect of Dopants on Zirconia Stabilization—An X-ray Absorption Study: II, Tetravalent Dopants,” *J. Am. Ceram. Soc.*, vol. 77, no. 5, pp. 1281–1288, May 1994, doi: https://doi.org/10.1111/j.1151-2916.1994.tb05403.x.
[36] S. Ghyngazov and S. Shevelev, “Effect of additives on sintering of zirconia ceramics,” *J. Therm. Anal. Calorim.*, vol. 134, Apr. 2018, doi: 10.1007/s10973-018-7249-0.

APPENDICES

Appendix – A

- Sintering profiles and sinter parameters for calculated for all the sintered samples

$Zr(OH)_4$-50 MPa:

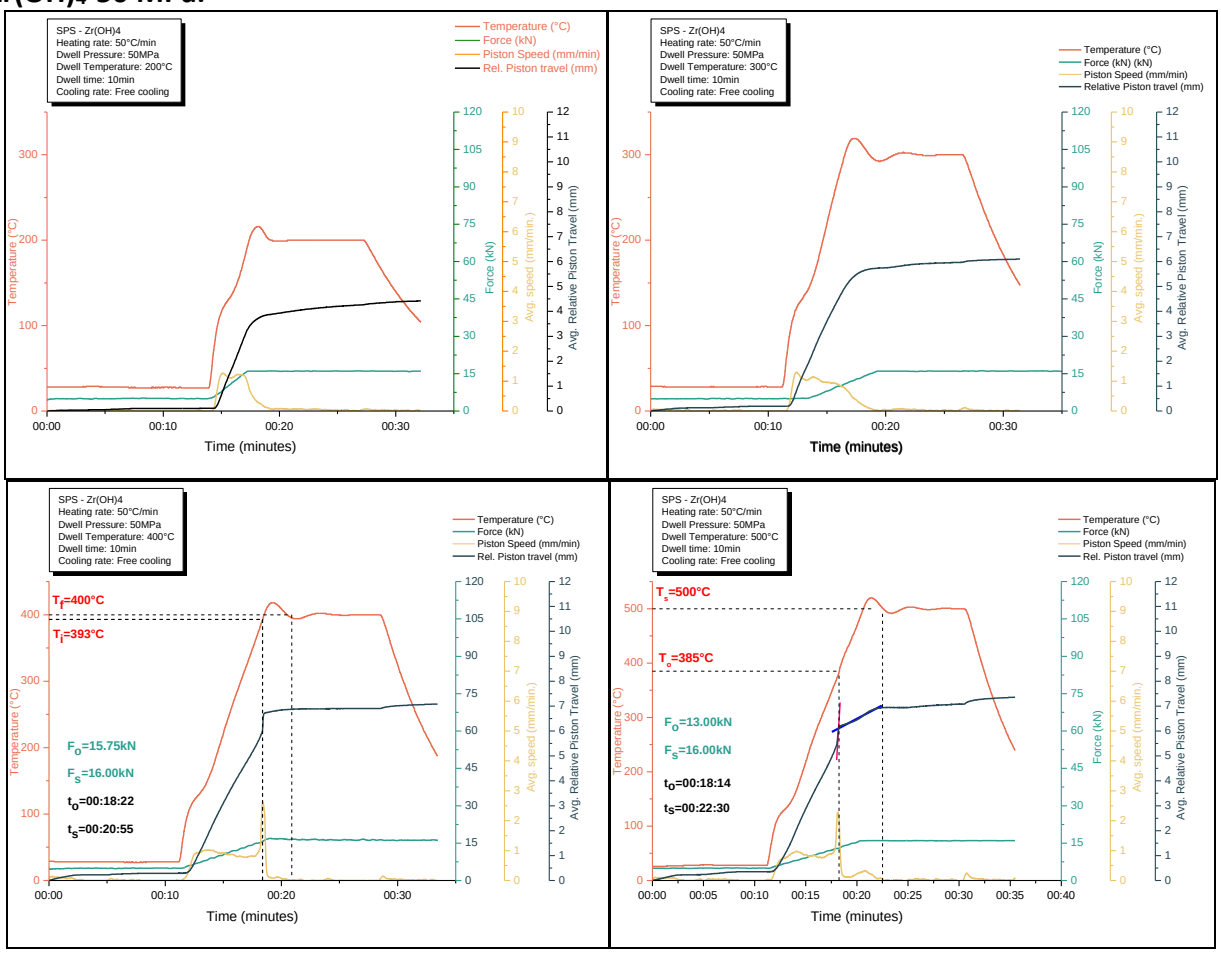

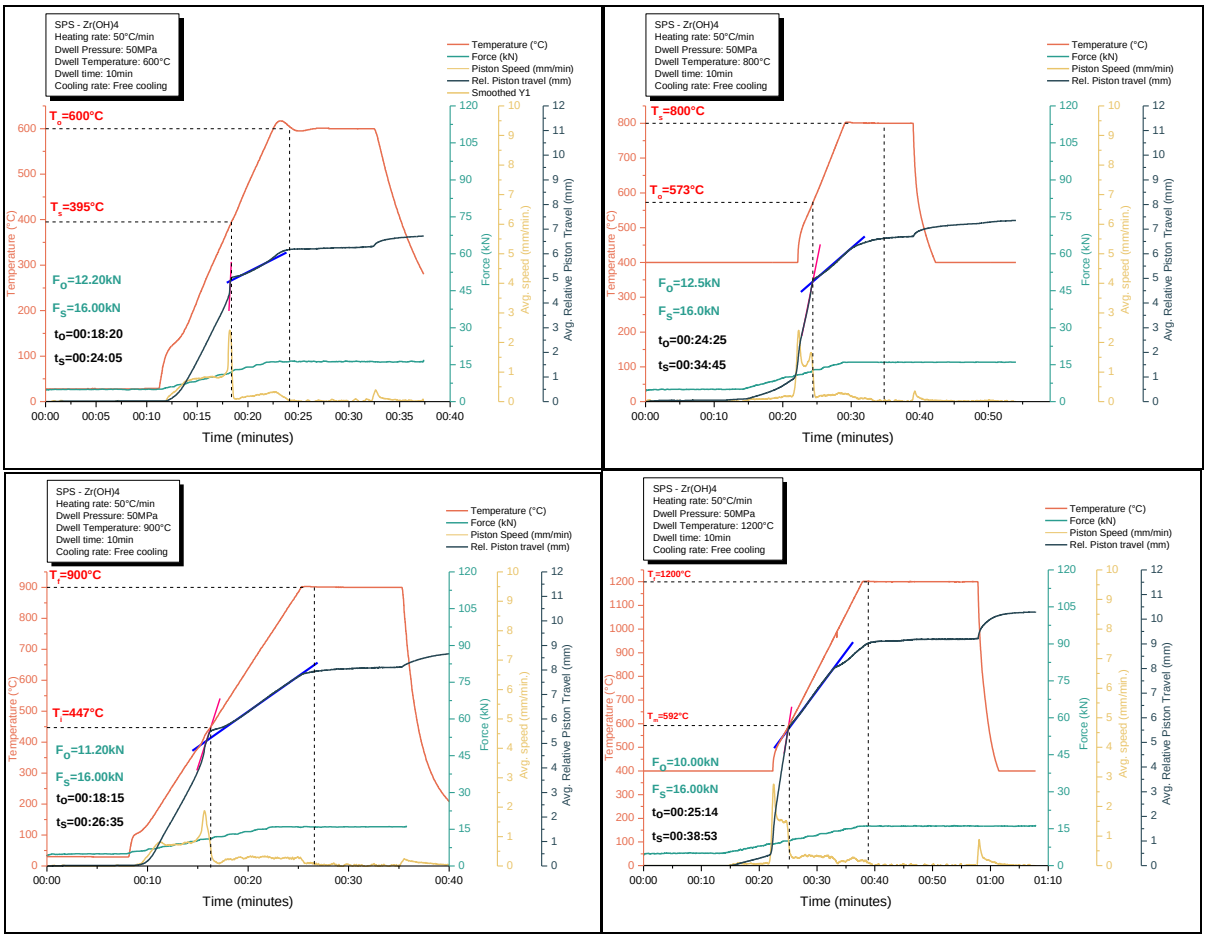

Figure 69: SPS piston displacement curves with projected sintering times, forces, and temperatures for 50 MPa dwell pressure samples of pure $Zr(OH)_4$

ZrO2-50 MPa:

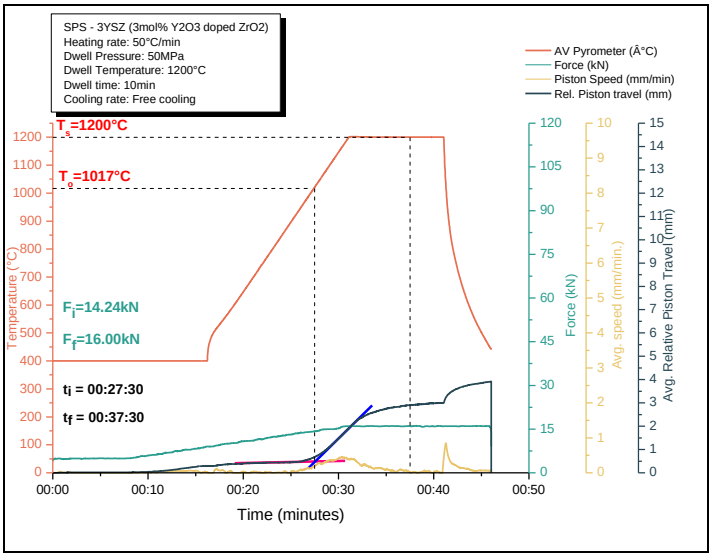

Figure 70: SPS piston displacement curves with projected sintering times, forces, and temperatures for 50 MPa dwell pressure sample of 3mol% Yttria stabilized ZrO_2

$Zr(OH)_4$ 150 MPa:

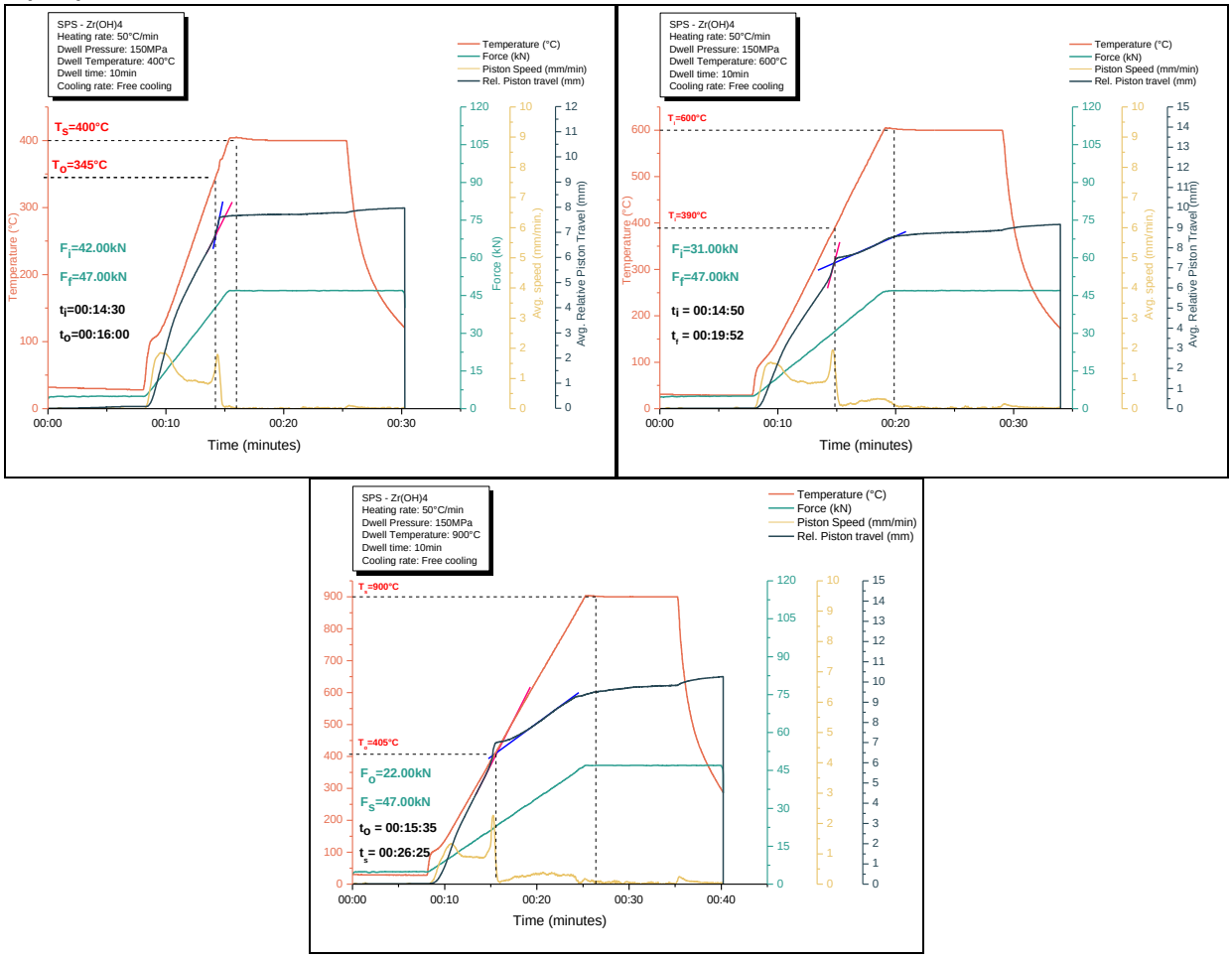

Figure 71: SPS piston displacement curves with projected sintering times, forces, and temperatures for 150 MPa dwell pressure samples of pure $Zr(OH)_4$

$Zr(OH)_4$ 300 MPa:

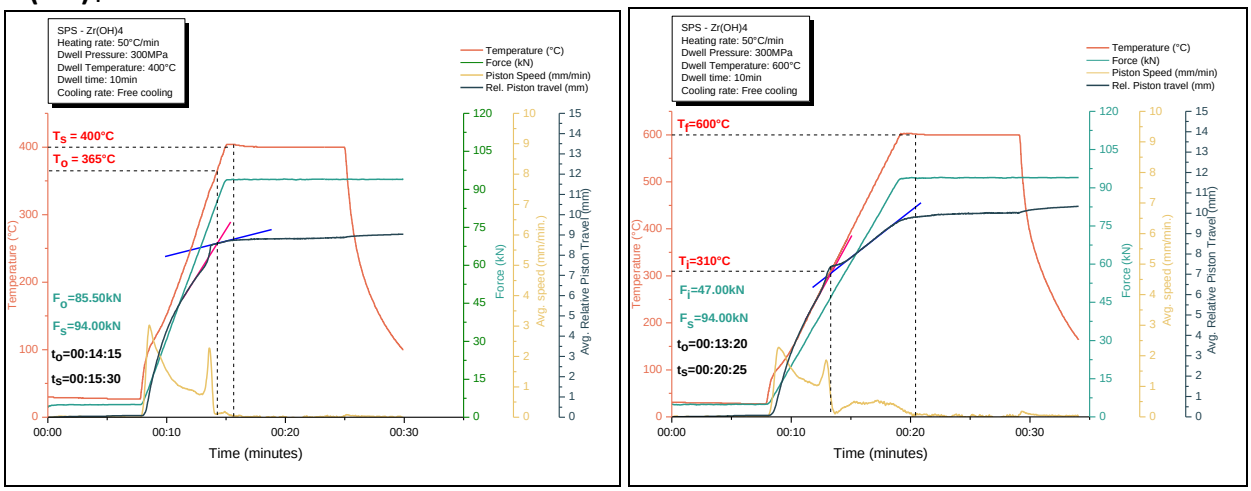

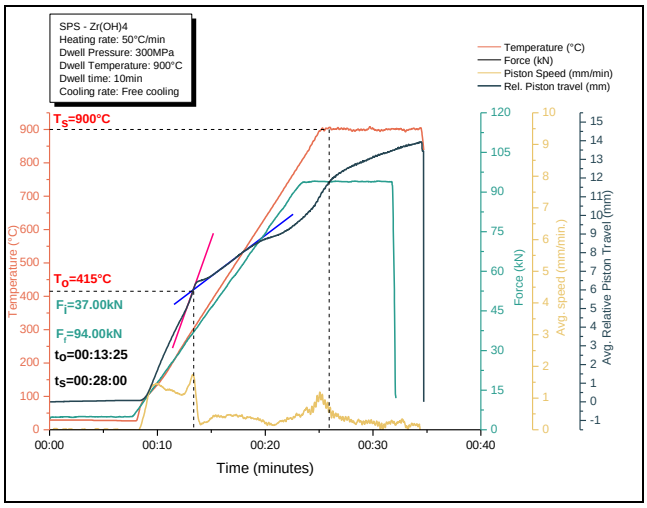

Figure 72: SPS piston displacement curves with projected sintering times, forces, and temperatures for 50 MPa dwell pressure samples of pure $Zr(OH)_4$

10wt%Bi_2O3-$Zr(OH)_4$:

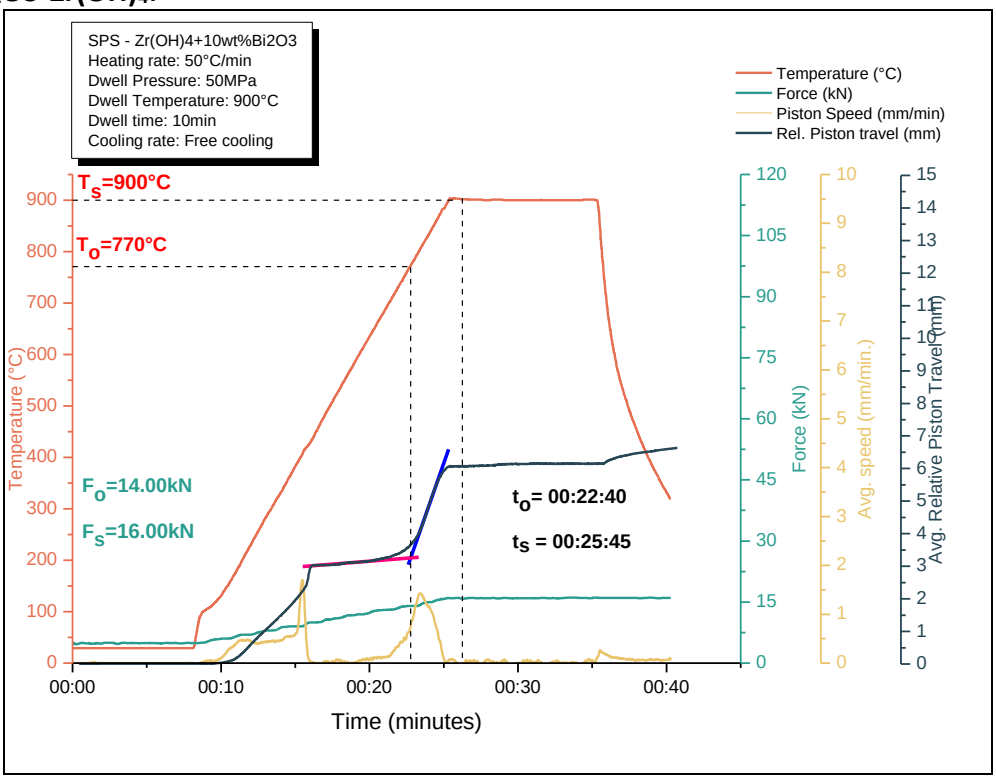

Figure 73: PS piston displacement curves with projected sintering times, forces, and temperatures for 50 MPa dwell pressure samples of 10wt% Bi_2O_3-$Zr(OH)_4$

ZrH_2-$Zr(OH)_4$ systems:

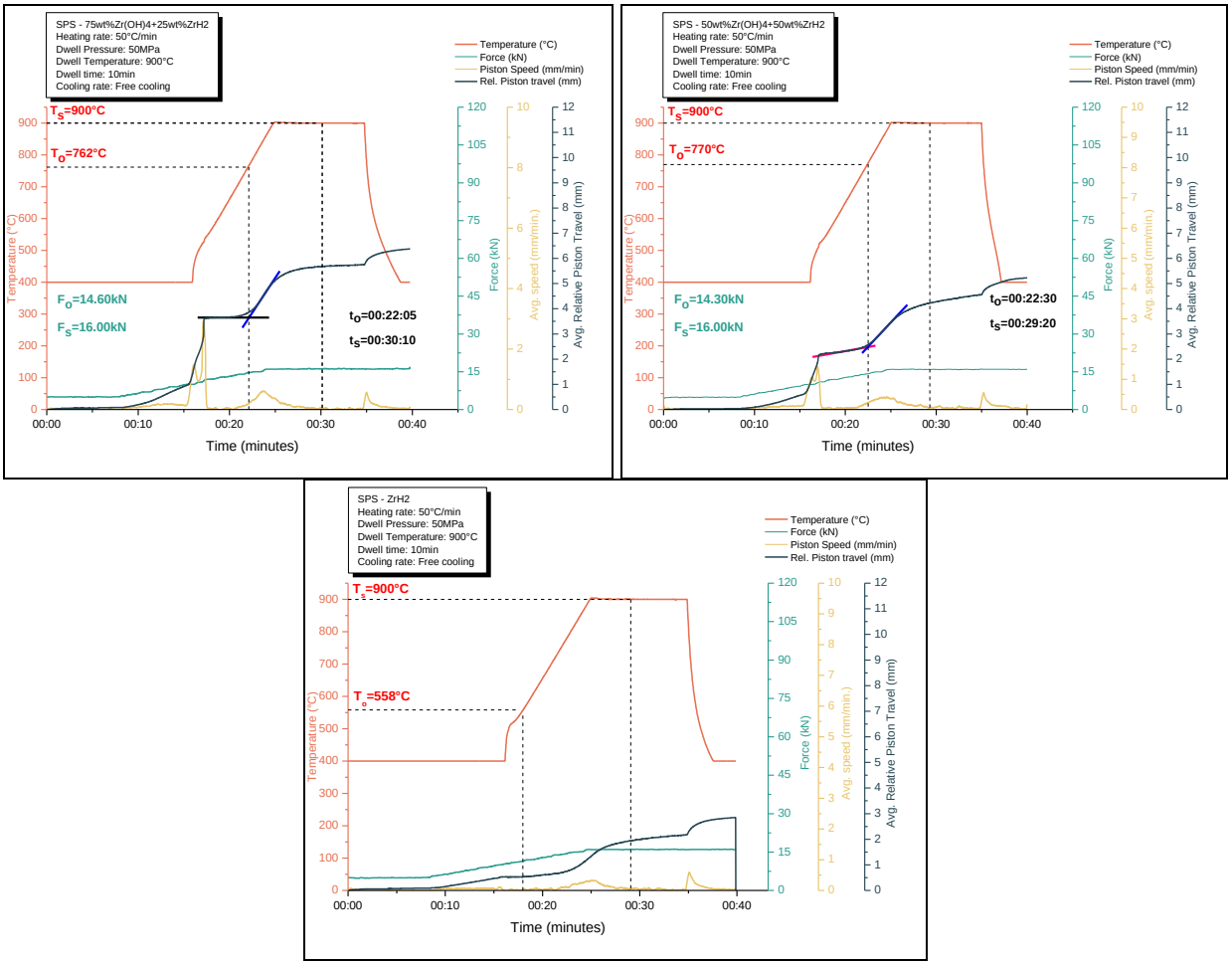

Figure 74: SPS piston displacement curves with projected sintering times, forces, and temperatures for 50 MPa dwell pressure samples of 25wt% ZrH_2-$Zr(OH)_4$, 50wt% ZrH_2-$Zr(OH)_4$, and pure ZrH_2

Appendix – B

- X-ray diffraction curves after full pattern matching with monoclinic and tetragonal phases of ZrO_2

$Zr(OH)_4$-50 MPa:

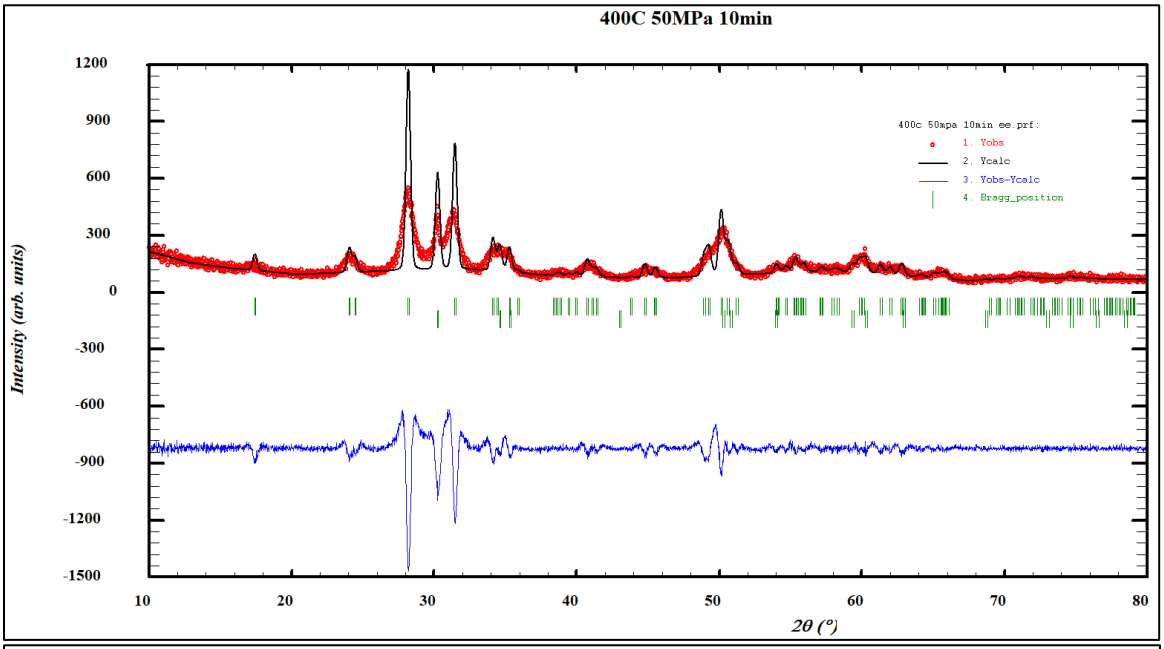

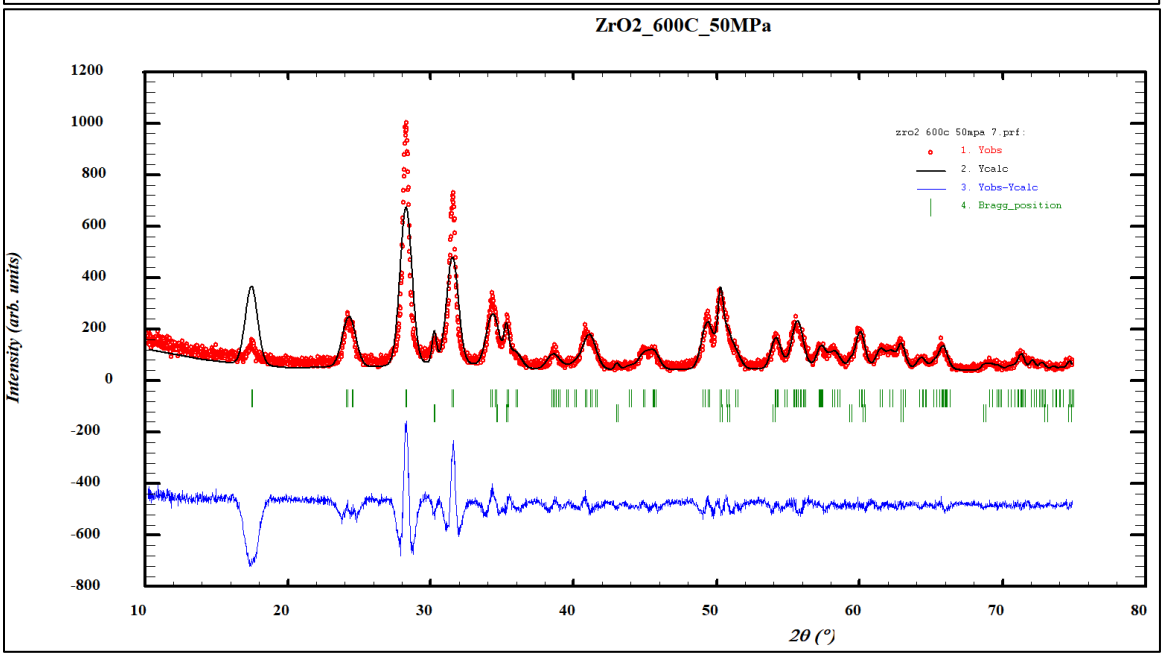

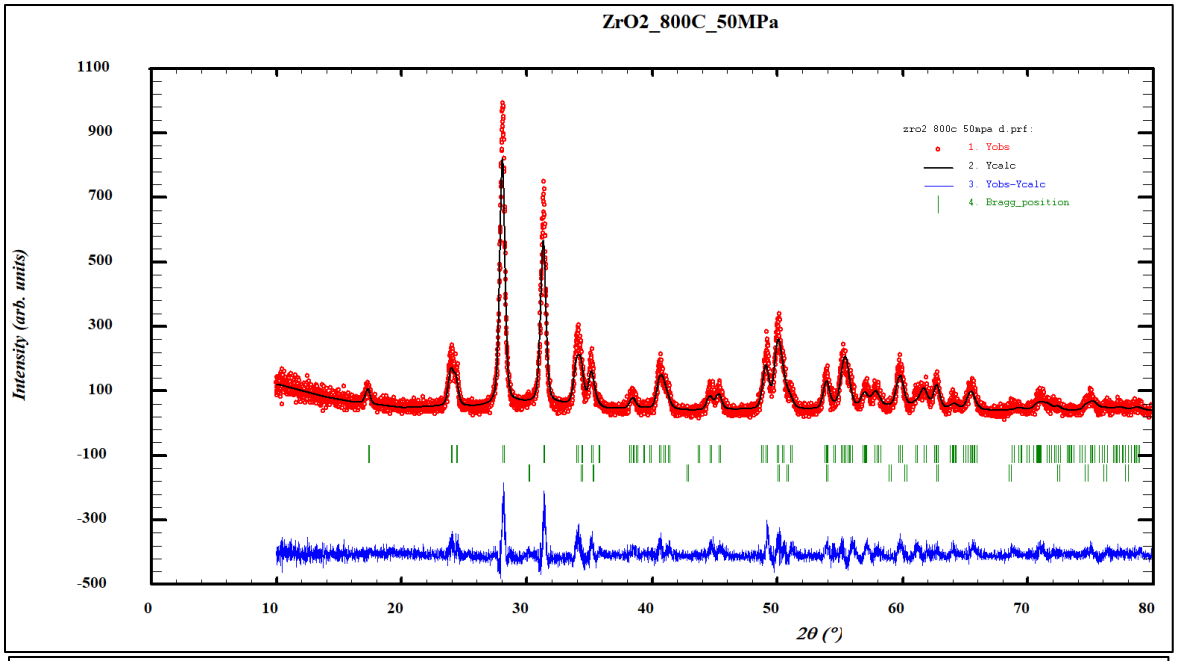
ZrO2_800C_50MPa
zro2 800c 50mpa d.prf:
1. Yobs
2. Ycalc
3. Yobs-Ycalc
4. Bragg_position
Intensity (arb. units)
2θ (°)

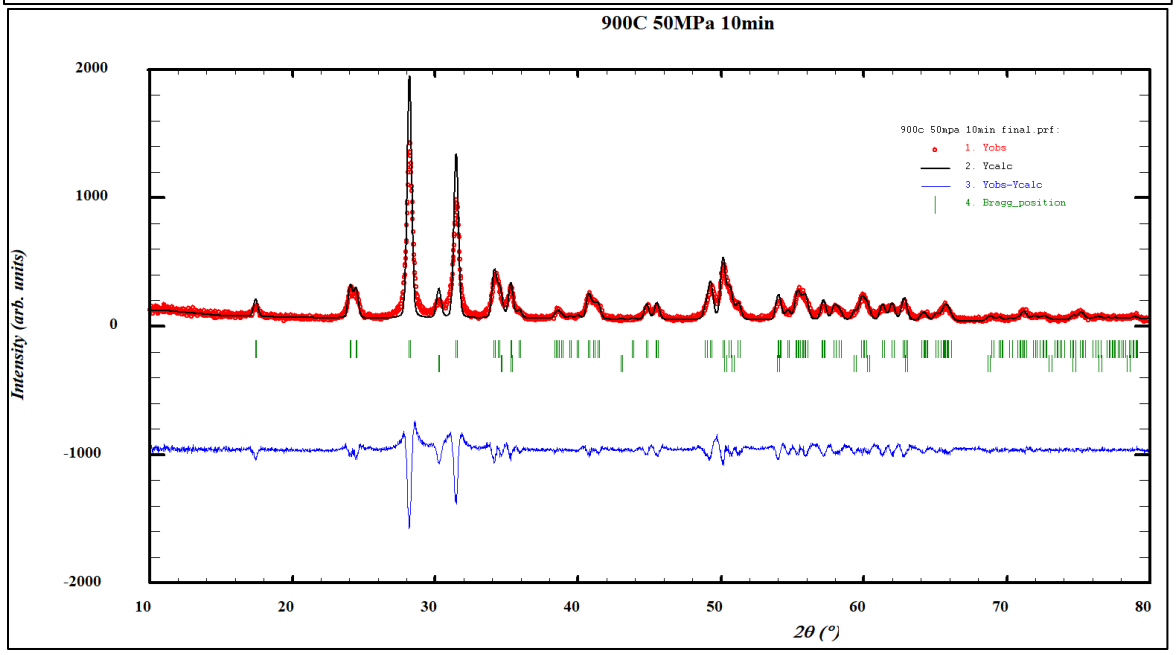
900C 50MPa 10min
900c 50mpa 10min final.prf:
1. Yobs
2. Ycalc
3. Yobs-Ycalc
4. Bragg_position
Intensity (arb. units)
2θ (°)

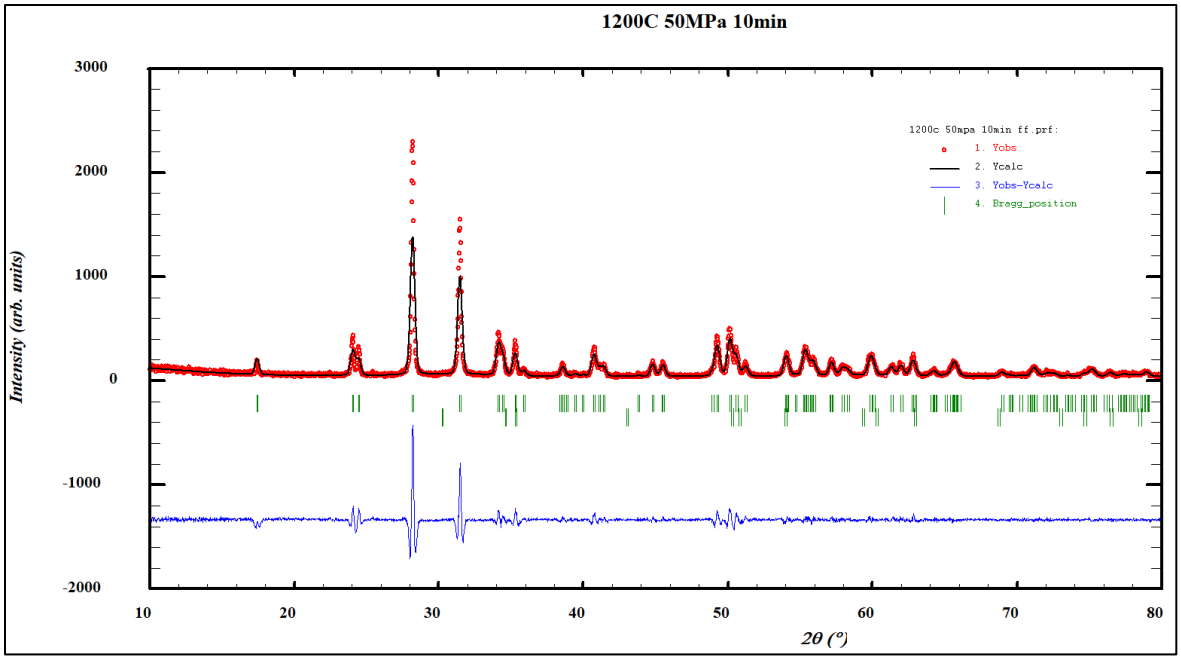

Figure 75: Full pattern matched XRD plots of pure $Zr(OH)_4$ system sintered at 400°C, 600°C, 800°C, 900°C, and 1200°C with a dwell pressure of 50 MPa

Table 30: R-Bragg factor of the curve fittings done by full pattern matching for pure $Zr(OH)_4$ systems

Sample	Bragg R factor Monoclinic	Bragg R factor Tetragonal
400°C – 50 MPa $Zr(OH)_4$	12.90000	2.18000
600°C – 50 MPa $Zr(OH)_4$	0.68500	1.22000
800°C – 50 MPa $Zr(OH)_4$	1.39000	2.79000
900°C – 50 MPa $Zr(OH)_4$	1.94000	2.39000
1200°C – 50 MPa $Zr(OH)_4$	0.78900	1.97000

Yttria doped $Zr(OH)_4$ systems:

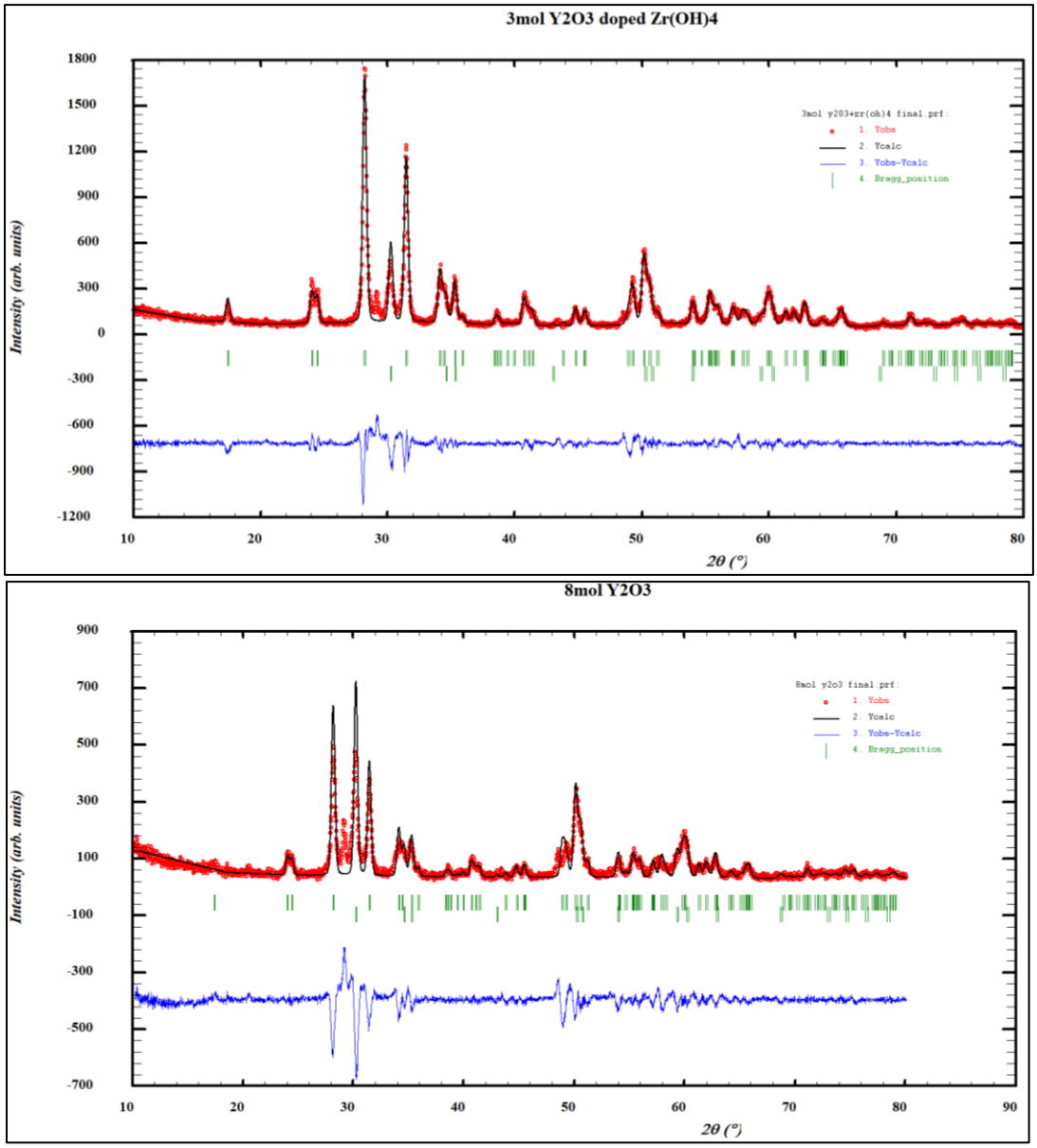

Figure 76: Full pattern matched XRD plots of Y_2O_3 doped $Zr(OH)_4$ systems sintered 900°C with a dwell pressure of 50 MPa

Bismuth oxide doped $Zr(OH)_4$ systems:

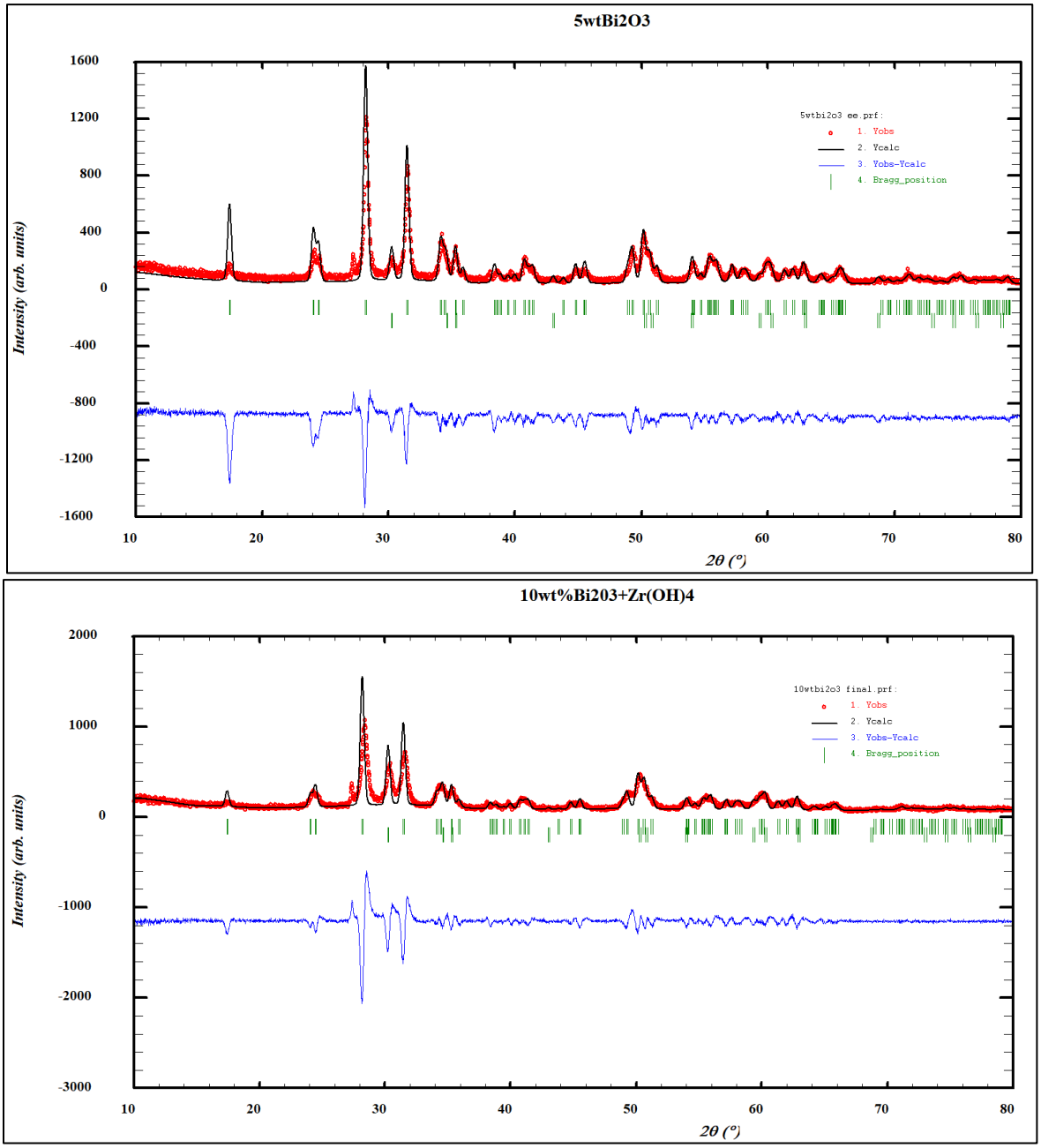

Figure 77: Full pattern matched XRD plots of Bi_2O_3 doped $Zr(OH)_4$ systems sintered 900°C with a dwell pressure of 50 MPa

Zirconium Hydride systems:

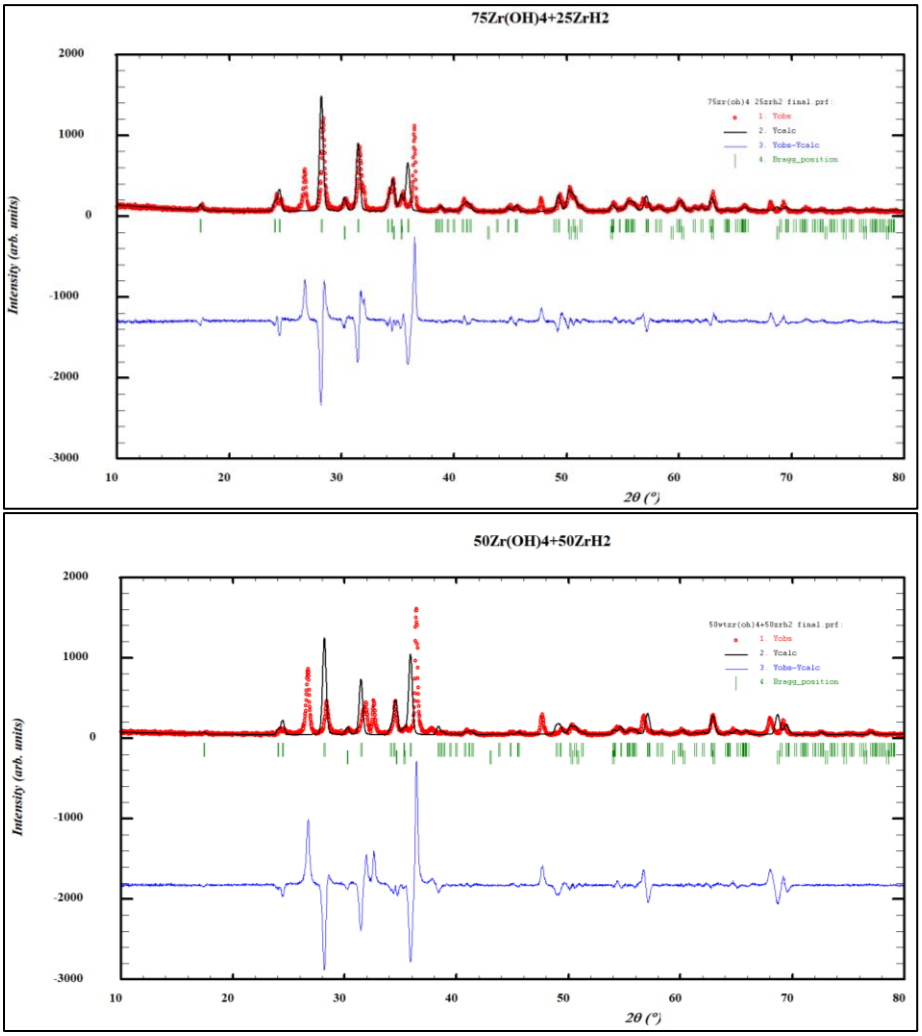

Figure 78: Full pattern matched XRD plots of ZrH_2-$Zr(OH)_4$ systems sintered 900°C with a dwell pressure of 50 MPa

Table 31: R-Bragg factor of the curve fittings done by full pattern matching for doped $Zr(OH)_4$ systems

Sample	Bragg R factor Monoclinic	Bragg R factor Tetragonal
3mol% Y_2O_3-$Zr(OH)_4$	2.02000	1.75000
8mol% Y_2O_3-$Zr(OH)_4$	4.16000	2.56000
5wt% Bi_2O_3-$Zr(OH)_4$	2.67000	1.97000
10wt% Bi_2O_3-$Zr(OH)_4$	4.62000	4.42000
25wt% ZrH_2-$Zr(OH)_4$	28.40000	17.40000
50wt% ZrH_2-$Zr(OH)_4$	8.42000	3.36000

Appendix – C

- Hardness values calculated from Vickers hardness method
- The Vickers hardness is measured using the formula:
  - $Hv = \frac{0.1891 * F}{d^2}$

Where;
HV – Vickers hardness (N/mm^2)
F – Applied force (N) = 4.905N
d – Avg. length of the diagonals (mm)

- The hardness value in GPa is calculated by multiplying the Vickers hardness value by 0.009807

Pure $Zr(OH)_4$:

$Zr(OH)_4$-900°C-50 MPa:

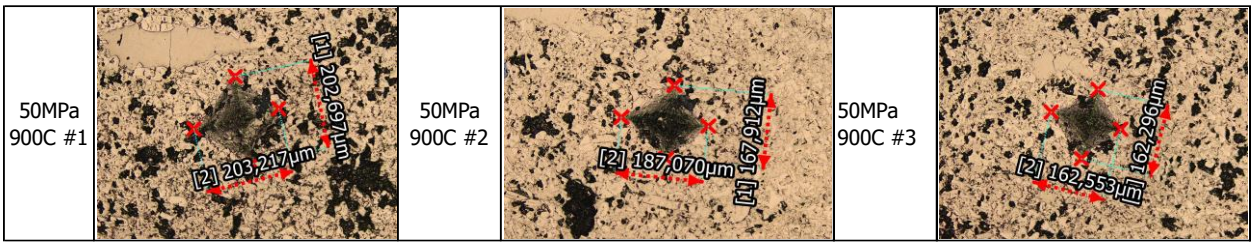

Figure 79: Diagonals of Vickers hardness indentations measured from 50 MPa dwell pressure pure $Zr(OH)_4$ samples sintered at 900°C

ZrO2-1200°C-50 MPa:

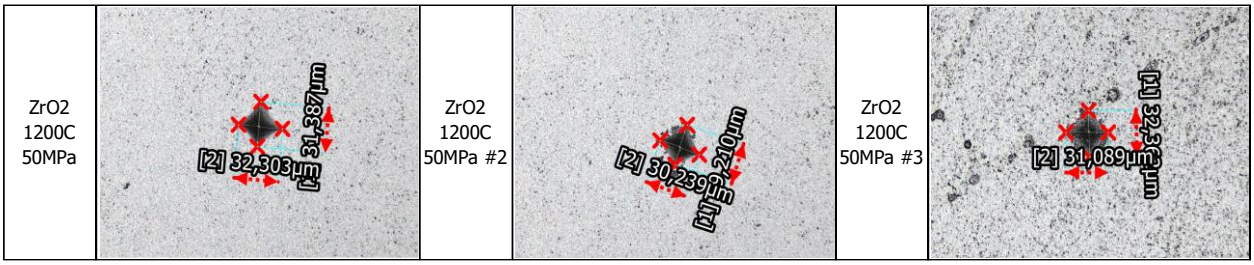

Figure 80: Diagonals of Vickers hardness indentations measured from ZrO_2 sample sintered with 1200°C dwell temperature and 50 MPa dwell pressure

$Zr(OH)_4$-150 MPa:

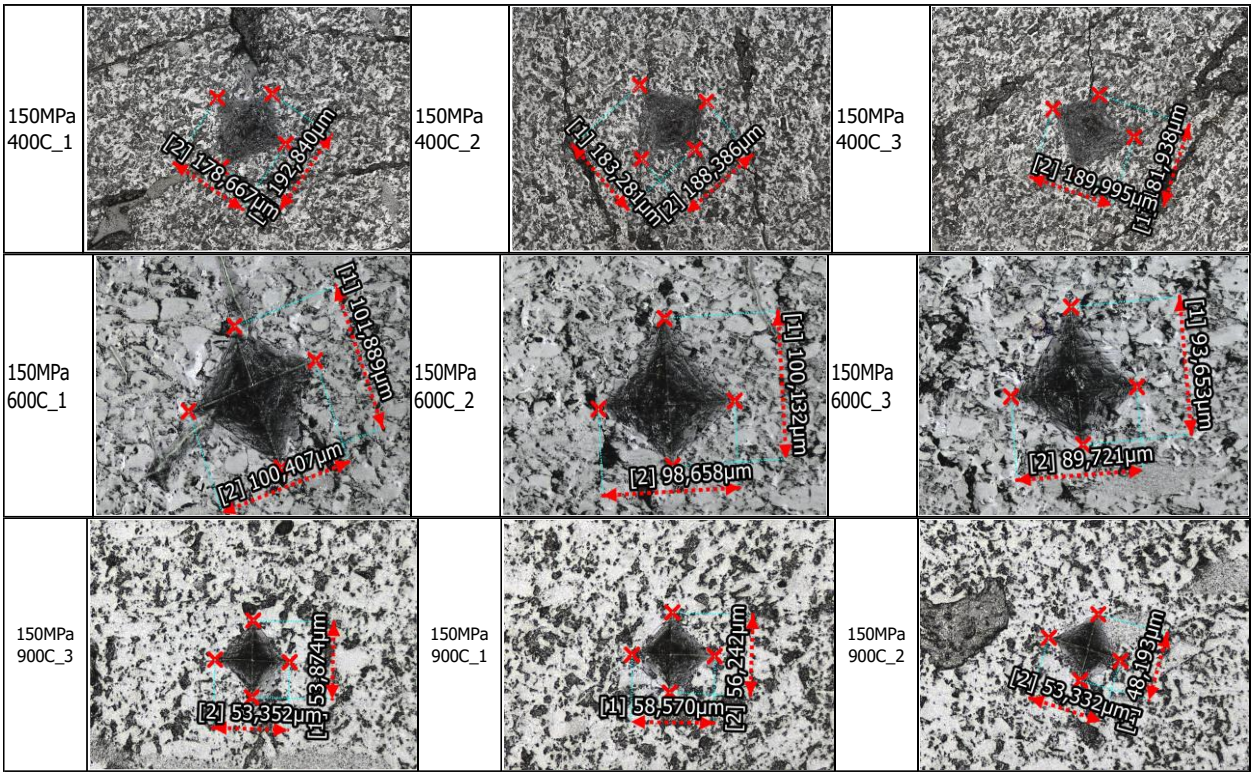

Figure 81: Diagonals of Vickers hardness indentations measured from 150 MPa dwell pressure pure $Zr(OH)_4$ samples sintered at 400°C, 600°C, and 900°C

$Zr(OH)_4$-300 MPa:

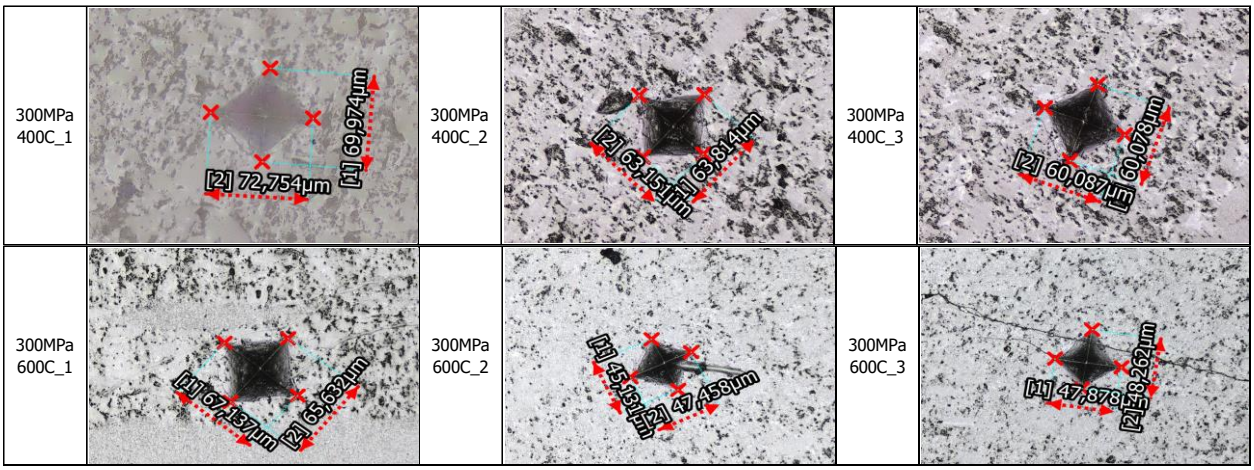

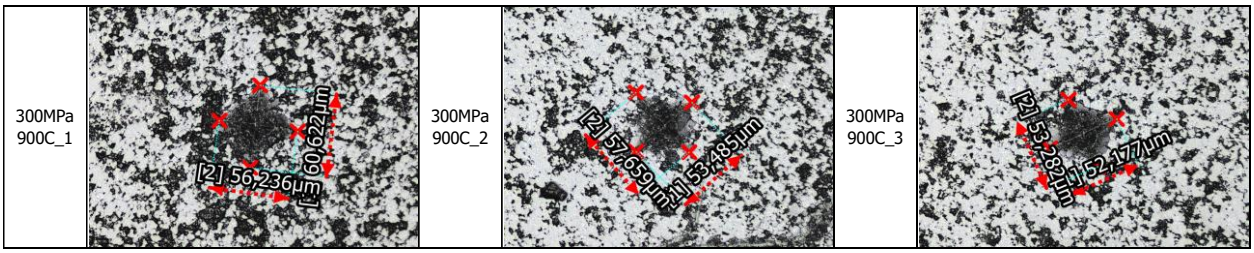

Figure 82: Diagonals of Vickers hardness indentations measured from 300 MPa dwell pressure pure $Zr(OH)_4$ samples sintered at 400°C, 600°C, and 900°C

Table 32: Hardness calculations for the pure $Zr(OH)_4$ samples sintered at various dwell pressures and temperatures

Sample	Diagonal 1 (mm)	Diagonal 2 (mm)	Avg. diagonal (mm)	Vickers Hardness (HV)	Avg. Vickers Hardness (HV)	Hardness (GPa)	Rel. density (%)	Porosity (%)
$Zr(OH)_4$ 900°C-50MPa	0.203	0.203	0.203	22.52	29.04	0.28479071	53.74	46.26
	0.187	0.168	0.177	29.44				
	0.163	0.162	0.162	35.16				
$Zr(OH)_4$ 400°C-150MPa	0.179	0.193	0.186	26.88	26.85	0.26335188	44.33	55.67
	0.183	0.188	0.186	26.86				
	0.190	0.182	0.186	26.82				
$Zr(OH)_4$ 600°C-150MPa	0.100	0.102	0.101	90.66	98.29	0.96396801	50.83	49.17
	0.099	0.100	0.099	93.89				
	0.090	0.094	0.092	110.34				
$Zr(OH)_4$ 900°C-150MPa	0.053	0.054	0.054	322.69	321.37	3.15165946	69.30	30.70
	0.059	0.056	0.057	281.46				
	0.053	0.048	0.051	359.95				
$Zr(OH)_4$ 400°C-300MPa	0.073	0.063	0.068	200.87	229.32	2.2489736	56.37	43.63
	0.063	0.064	0.063	230.16				
	0.060	0.060	0.060	256.94				
$Zr(OH)_4$ 600°C-300MPa	0.067	0.066	0.066	210.47	348.22	3.41500163	69.90	30.10
	0.045	0.047	0.046	432.78				
	0.048	0.048	0.048	401.40				
$Zr(OH)_4$ 900°C-300MPa	0.056	0.061	0.058	271.69	301.88	2.96050938	86.97	13.03
	0.058	0.053	0.056	300.34				
	0.053	0.052	0.053	333.60				
3YSZ 1200°C-50MPa	0.032	0.031	0.032	914.64	961.98	9.43411401	72.48	27.52
	0.030	0.029	0.030	1049.79				
	0.031	0.032	0.032	921.51				

Bi_2O_3-$Zr(OH)_4$ systems:

5wt% Bi_2O_3-$Zr(OH)_4$-50 MPa:

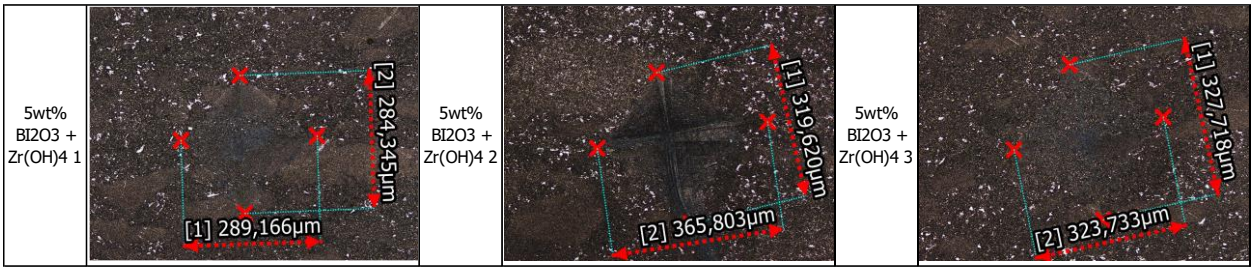

Figure 83: Diagonals of Vickers hardness indentations measured from 5wt% Bi_2O_3-$Zr(OH)_4$ sample sintered with 900°C dwell temperature and 50 MPa dwell pressure

10wt% Bi_2O_3-$Zr(OH)_4$-50 MPa:

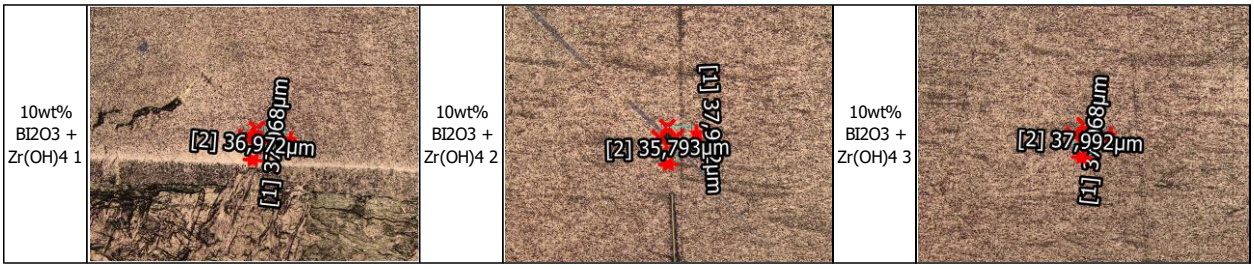

Figure 84: Diagonals of Vickers hardness indentations measured from 10wt% Bi_2O_3-$Zr(OH)_4$ sample sintered with 900°C dwell temperature and 50 MPa dwell pressure

Table 33: Hardness calculations for the Bi_2O_3-$Zr(OH)_4$ samples sintered at 50 MPa dwell pressure and 900°C dwell temperatures

Sample	Diagonal 1 (mm)	Diagonal 2 (mm)	Average diagonal (mm)	Vickers Hardness HV	Average Hardness HV	Hardness (GPa)	Porosity (%)
5wt% Bi_2O_3	0.289	0.284	0.287	11.28	9.31	0.091331	54.63
	0.32	0.366	0.343	7.9			
	0.328	0.324	0.326	8.74			
10wt% Bi_2O_3	0.037	0.037	0.037	676.8	672.27	6.594969	27.37
	0.038	0.036	0.037	681.48			
	0.037	0.038	0.038	658.53			

ZrH_2-$Zr(OH)_4$ system:

25wt% ZrH_2-$Zr(OH)_4$ – 50 MPa:

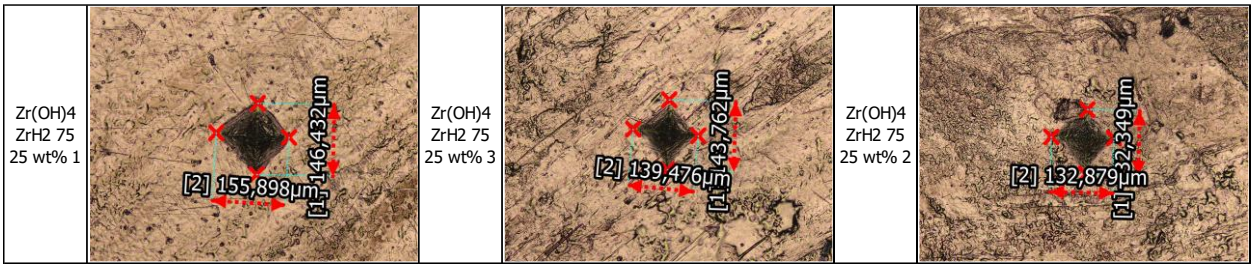

Figure 85: Diagonals of Vickers hardness indentations measured from 25wt% ZrH_2-$Zr(OH)_4$ sample sintered with 900°C dwell temperature and 50 MPa dwell pressure

50wt% ZrH_2-$Zr(OH)_4$ – 50 MPa:

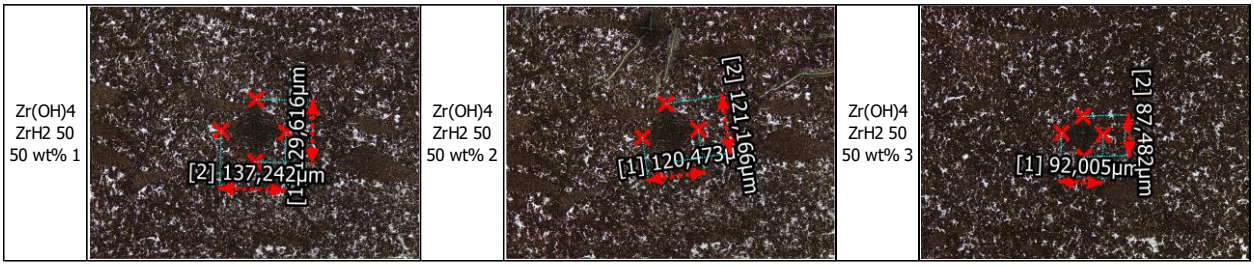

Figure 86: Diagonals of Vickers hardness indentations measured from 50wt% ZrH_2-Zr(OH)4 sample sintered with 900°C dwell temperature and 50 MPa dwell pressure

Pure ZrH_2 – 50 MPa:

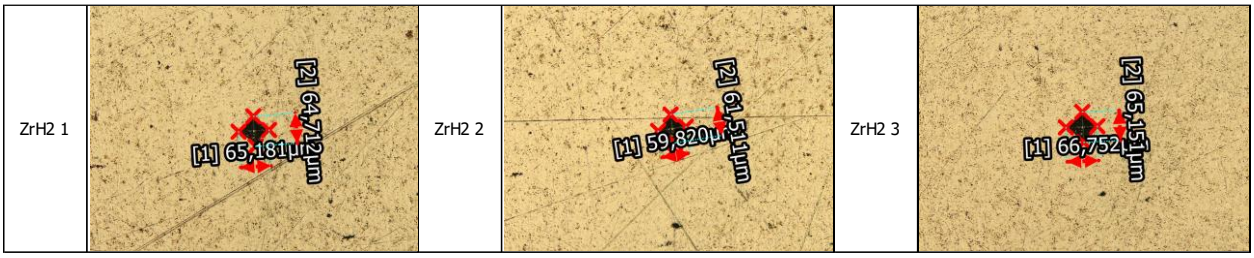

Figure 87: Diagonals of Vickers hardness indentations measured from pure ZrH_2 sample sintered with 900°C dwell temperature and 50 MPa dwell pressure

Table 34: Hardness calculations for the ZrH_2-$Zr(OH)_4$ samples sintered at 50 MPa dwell pressure and 900°C dwell temperatures

Sample	Diagonal 1 (mm)	Diagonal 2 (mm)	Average diagonal (mm)	Vickers Hardness HV	Average Hardness	Hardness (GPa)	Porosity (%)
$Zr(OH)_4$-100wt%	0.203	0.203	0.203	22.52	29.04	0.284882	45.96
	0.168	0.187	0.177	29.44			
	0.162	0.163	0.162	35.16			
$Zr(OH)_4$-75wt% + ZrH_2-25wt%	0.146	0.156	0.151	40.59	46.53	0.456459	39.39
	0.144	0.139	0.142	46.25			
	0.132	0.133	0.133	52.74			
$Zr(OH)_4$-50wt% + ZrH_2-50wt%	0.13	0.137	0.133	52.1	76.94	0.754781	31.36
	0.12	0.121	0.121	63.54			
	0.092	0.087	0.09	115.17			
ZrH_2-100wt%	0.065	0.065	0.065	219.9	228.39	2.240506	22.35
	0.06	0.062	0.061	252.03			
	0.067	0.065	0.066	213.25			